

**MULTIMODE-INTERFERENCE BASED OPTICAL FIBER
SENSOR FOR CIVIL STRUCTURES MONITORING**

CHEW SUE PING

**FACULTY OF ENGINEERING
UNIVERSITY OF MALAYA
KUALA LUMPUR**

2020

**MULTIMODE-INTERFERENCE BASED OPTICAL FIBER
SENSOR FOR CIVIL STRUCTURES MONITORING**

CHEW SUE PING

**THESIS SUBMITTED IN FULFILMENT OF THE
REQUIREMENTS FOR THE DEGREE OF DOCTOR
PHILOSOPHY**

**FACULTY OF ENGINEERING
UNIVERSITY OF MALAYA
KUALA LUMPUR**

2020

UNIVERSITY OF MALAYA
ORIGINAL LITERARY WORK DECLARATION

Name of Candidate: **CHEW SUE PING**

Matric No: **KHA130070**

Name of Degree: **Doctor of Philosophy**

Title of Project Paper/Research Report/Dissertation/Thesis (“this Work”):

MULTIMODE-INTERFERENCE BASED OPTICAL FIBER SENSOR FOR CIVIL STRUCTURES MONITORING

Field of Study:

PHOTONICS

I do solemnly and sincerely declare that:

- (1) I am the sole author/writer of this Work;
- (2) This Work is original;
- (3) Any use of any work in which copyright exists was done by way of fair dealing and for permitted purposes and any excerpt or extract from, or reference to or reproduction of any copyright work has been disclosed expressly and sufficiently and the title of the Work and its authorship have been acknowledged in this Work;
- (4) I do not have any actual knowledge nor do I ought reasonably to know that the making of this work constitutes an infringement of any copyright work;
- (5) I hereby assign all and every rights in the copyright to this Work to the University of Malaya (“UM”), who henceforth shall be owner of the copyright in this Work and that any reproduction or use in any form or by any means whatsoever is prohibited without the written consent of UM having been first had and obtained;
- (6) I am fully aware that if in the course of making this Work I have infringed any copyright whether intentionally or otherwise, I may be subject to legal action or any other action as may be determined by UM.

Candidate’s Signature

Date:

Subscribed and solemnly declared before,

Witness’s Signature

Date:

Name:

Designation:

ABSTRACT

The thesis describes the experimental investigations on the multimode interference-based fiber sensors using single mode multimode single mode (SMS) and multimode single mode multimode (MSM) structures as a sensing device for structural health monitoring (SHM) applications. Both sensor structures were fabricated, characterized and tested for detecting strain and vibration in civil infrastructures. The proposed SMS structure comprises of a short segment of multimode fiber (MMF), which were fusion-spliced by two single mode fibers (SMFs) at both terminals. On the other hand, MSM was fabricated by splicing SMF with MMF at both ends. A new packaging technique for the SMS structure was successfully developed to use as water level gauge. The SMS structure was also used to measure the strain in a reinforced concrete beam. The results indicated that the SMS fiber sensor provides sensitivity of 3.7781 nm/(mm/mm) and linearity of 0.96606 in compressive strain measurements to a maximum of 0.116 mm/mm. It was also found that the packaged SMS has much better temperature stability up to 0.0904 nm/°C as compared to unpackaged SMS. On the other hand, the developed MSM based sensor was successfully used to demonstrate a vibration frequency measurement of the mechanical vibration. The structure was capable of detecting wide range of vibration frequency, ranging from 20 Hz up to 6 kHz with high accuracy.

Keywords: multimode interference, single mode multimode single mode (SMS), multimode single mode multimode (MSM), civil structural monitoring

ABSTRAK

Tesis ini menerangkan kajian eksperimental pada sensor gentian berasaskan gangguan multimod dengan menggunakan struktur mod tunggal multimod mod tunggal (SMS) dan multimod mod tunggal multimod (MSM) sebagai alat pengesan bagi aplikasi pemantauan kesihatan struktur (SHM). Kedua-dua struktur sensor dibuat, dicirikan dan diuji untuk mengesan ketegangan dan getaran pada infrastruktur awam. Struktur SMS yang dicadangkan terdiri daripada segmen pendek multimod (MMF), yang disambungkan secara pelakuran oleh dua gentian mod tunggal (SMF) di kedua-dua terminal. Sebaliknya, MSM dibuat dengan menggabungkan SMF dengan MMF di kedua-dua hujungnya. Teknik pembungkusan baru untuk struktur SMS berjaya dikembangkan untuk digunakan sebagai alat pengukur paras air. Struktur SMS juga digunakan untuk mengukur ketegangan pada blok konkrit bertetulang. Hasilnya menunjukkan bahawa sensor gentian SMS memberikan kepekaan $3.77781 \text{ nm}/(\text{mm}/\text{mm})$ dan lineariti 0.96606 dalam pengukuran regangan mampatan hingga maksimum $0.166 \text{ mm}/\text{mm}$. Juga didapati bahawa SMS yang dibungkus mempunyai kestabilan suhu yang jauh lebih baik hingga $0.0904 \text{ nm}/^\circ\text{C}$ berbanding dengan SMS yang tidak dibungkus. Sebaliknya, sensor berasaskan MSM yang dikembangkan berjaya digunakan untuk menunjukkan pengukuran frekuensi getaran bagi getaran mekanikal. Struktur ini mampu mengesan pelbagai frekuensi getaran, mulai dari 20 Hz hingga 6 kHz dengan ketepatan tinggi.

Kata kunci: gangguan multimod, mod tunggal multimod mod tunggal (SMS), multimod mod tunggal multimod (MSM), pemantauan struktur awam.

ACKNOWLEDGEMENTS

First and foremost, I would like to thank my supervisors, Prof. Dr. Sulaiman Wadi Harun and Prof. Dr. Faisal Rafiq Bin Mahamd Adikan for their invaluable guidance, continuous support and motivation in completing this study. In addition, I would like to express my gratitude to every lecturers and staff of Faculty of Engineering, University of Malaya for their countless assistance, guidance and support throughout the journey in completing my thesis.

My deepest gratitude to my beloved parents, Chew Wee Kok and Mary Ong, who have been praying for my success continuously without fail, as well as supporting and motivating me. My upmost appreciation to my spouse, Lee Leong Yee for his never-ending support, help that has motivated me to complete my thesis. In addition, not to forget my precious and adorable daughters, Lee En Ting and Lee En Xuan for giving me the strength to continue my study. I never give up in my life as they are giving me countless happiness and laughter.

Last but not least, thank you to all my fellow friends especially Latifah Sarah Binti Sufian for the continuous supports, assistance and constructive criticism towards me.

TABLE OF CONTENTS

ORIGINAL LITERARY WORK DECLARATION.....	II
ABSTRACT.....	III
ABSTRAK.....	IV
ACKNOWLEDGEMENTS.....	V
TABLE OF CONTENTS.....	VI
LIST OF FIGURES.....	IX
LIST OF TABLES.....	XII
LIST OF SYMBOLS AND ABBREVIATIONS.....	XIII
LIST OF APPENDICES.....	XIV
CHAPTER 1: INTRODUCTION.....	1
1.1 Research Background.....	1
1.2 Problem statements and scope of work.....	3
1.3 Research objectives.....	4
1.4 Significance of study.....	5
1.5 Outline of Thesis.....	5
CHAPTER 2: LITERATURE REVIEW.....	7
2.1 Introduction.....	7
2.2 Fiber Bragg Gratings and its Applications.....	7
2.3 Multimode Interference in Optical Fiber.....	11
2.3.1 Self-imaging principle in MMI structure.....	11
2.3.2 Single mode Multimode Single mode (SMS) Structure.....	16
2.3.3 Multimode Single-mode Multi mode Structure (MSM).....	18
2.3.4 Review on MMI based optical fiber for sensing applications.....	19

2.3.4.1	Refractive Index Sensor	19
2.3.4.2	Strain Sensor	22
2.3.4.3	Vibration Sensor.....	25
2.3.4.4	Magnetic Field Sensor.....	28
2.3.4.5	Temperature Sensor.....	30

CHAPTER 3: FABRICATION AND CHARACTERIZATION OF SENSOR

PROBE 33

3.1	Construction and characterization of SMS sensor probe.....	33
3.1.1	Sensing principle of SMS structure.....	33
3.1.2	Fabrication of SMS sensor probe	35
3.1.3	Embedded SMS in Sandwiched Packaging.....	38
3.1.4	Characterization of SMS sensor probe	44
3.1.4.1	Investigation on Temperature Sensitivity of the SMS structure.....	44
3.1.4.2	Loading analysis of the SMS structure	50
3.2	Fabrication & Characterizations of MSM sensor probe.....	53
3.2.1	Sensing principle of MSM structure	53
3.2.2	Fabrication of MSM sensor probe.....	56
3.2.3	Characterization of MSM sensor probe.....	57
3.3	Summary.....	59

CHAPTER 4: WATER WAVE GAUGE BASED ON SINGLEMODE-MULTIMODE-SINGLEMODE FIBER STRUCTURE.....60

4.1	Introduction.....	60
4.2	Water Gauge Experimental setup	62
4.3	Results and discussion	67

4.4	Summary.....	76
CHAPTER 5:	SINGLEMODE-MULTIMODE-SINGLEMODE FIBER	
	STRUCTURE AS COMPRESSIVE STRAIN SENSOR ON A REINFORCED	
	CONCRETE BEAM.....	77
5.1	Introduction.....	77
5.2	Compressive Strain Experimental Setup	80
5.3	Results and Discussion	83
5.4	Summary.....	88
CHAPTER 6:	INVESTIGATION ON MULTIMODE UNCOATED SINGLE-	
	MODE MULTIMODE FIBER STRUCTURE FOR VIBRATION DETECTION	89
6.1	Introduction.....	89
6.2	Fabrication of sensor probe	91
6.3	Experimental setup for vibration test.....	93
6.4	Results and discussion	94
6.5	Summary.....	102
CHAPTER 7:	CONCLUSION & RECOMMENDATIONS	103
7.1	Conclusion	103
7.2	Future Works	106
REFERENCES.....		108

LIST OF FIGURES

Figure 1.1	: Main Processes in SHM.....	2
Figure 2.1	: Spectra Response of a FBG (Majumder et al., 2008).....	8
Figure 2.2	: Formation of Fresnel images (Bryngdahl, 1973).....	11
Figure 2.3	: MMI device.....	12
Figure 2.4	: 2D representation of the step-index multimode waveguide (Soldano & Pennings, 1995).....	13
Figure 2.5	: Amplitude-normalized lateral field profile (Soldano & Pennings, 1995).....	13
Figure 2.6	: Schematic diagram of a SMS fiber structure.....	17
Figure 2.7	: Schematic Diagram of MSM Structure.....	18
Figure 2.8	: a) Multi-tapered SMS structure b) Comparisons of wavelength shift for different number of tapers (Y. Zhao et al., 2015).....	21
Figure 2.9	: Laboratory setup for strain measurement using STMS structure (Y. Sun et al., 2017).....	24
Figure 2.10	: Schematic diagram of a gourd-shaped SMS structure (Tian et al., 2017)...	25
Figure 2.11	: Experimental setup for bent SMS vibration sensing (Q. Wu et al., 2014)..	26
Figure 2.12	: The vibration measurement system using SMS structure (Yong Zhao, Li, Meng, & Zhao, 2014).....	27
Figure 3.1	: Schematic Diagram of the SMS structure.....	36
Figure 3.2	: Power Spectrum of SMS structure with different MMF length.....	37
Figure 3.3	: Refractive index distribution of a curved fiber.....	39
Figure 3.4	: Refractive index distribution of an equivalent of a straight fiber.....	39
Figure 3.5	: Placement of fiber on the polymer plastic plate.....	42
Figure 3.6	: Adhesive fixture of fiber on polymer plastic plate.....	43
Figure 3.7	: Sandwiching fiber with two plastic polymer plates	43
Figure 3.8	: Packaging of SMS structure.....	43
Figure 3.9	: (a) Schematic diagram (b) photo image of experimental setup for temperature measurement of SMS structure.....	43
Figure 3.10	: Placement of thermocouple and SMS structure on the heater mat.....	45
Figure 3.11	: Power Spectrum for unpackaged and packaged SMS structures.....	46

Figure 3.12	: Peak wavelength response as a function of temperature and spectral response (inset) of unpackaged SMS.....	47
Figure 3.13	: Spectral response of packaged SMS as a function of temperature.....	48
Figure 3.14	: Peak wavelength response of packaged SMS as a function of temperature.....	49
Figure 3.15	: Schematic diagram load analysis experimental setup for packaged SMS structure.....	50
Figure 3.16	: Photo image of load analysis experimental setup for packaged SMS structure	50
Figure 3.17	: Transmission spectra of the packaged SMS for unloading condition.....	51
Figure 3.18	: Spectral response from the packaged SMS at different load values up to 480.526mN.....	52
Figure 3.19	: Central dip wavelength against the amount of load.....	53
Figure 3.20	: Schematic diagram of MSM structure.....	54
Figure 3.21	: Spectral response of MSM uncoated SMF length of 4.0 cm and 2.5 cm... ..	57
Figure 3.22	: Peak wavelength of the spectral response of MSM as a function of temperature.....	58
Figure 4.1	: SMS is sandwiched between CR-39 polymer plates.....	63
Figure 4.2	: SMS wave gauge experimental setup and photo image of the wave maker flume (C4MKII-5.0M Multi-Purpose Teaching Flume mounted with C4-67 wave generator).....	63
Figure 4.3	: Water wave parameters.....	67
Figure 4.4	: Wave celerity and wave length at different motor speeds.....	68
Figure 4.5	: (a) Average output power time series and (b) its corresponding frequency spectrum at wave celerity of 0.43 m/s.....	69
Figure 4.6	: (a) Average output power time series and (b) its corresponding frequency spectrum at wave celerity of 0.47 m/s.....	70
Figure 4.7	: (a) Average output power time series and (b) its corresponding frequency spectrum at wave celerity of 0.49 m/s.....	71
Figure 4.8	: (a) Average output power time series and (b) its corresponding frequency spectrum at wave celerity of 0.52 m/s.....	72
Figure 4.9	: (a) Average output power time series and (b) its corresponding frequency spectrum at wave celerity of 0.57 m/s.....	73
Figure 4.10	: Average output power pulse frequency at different wavelength.....	74
Figure 4.11	: Average output power pulse frequency at different wave celerity.....	75

Figure 5.1	: Reinforced concrete beam design.....	79
Figure 5.2	: Experimental setup in measuring compressive strain using ER strain gauge and SMS sensor.....	81
Figure 5.3	: Photo image of the test-site in the Civil Engineering Laboratory, University of Malaya, Malaysia.....	81
Figure 5.4	: SMS bandpass transmission spectrum on a reinforced concrete beam.....	83
Figure 5.5	: Peak bandpass spectra at different compressive loads.....	84
Figure 5.6	: Compressive strain and spectral peak center wavelength at different compressive loads.....	85
Figure 5.7	: Compressive strain and spectral peak power at different compressive loads.....	86
Figure 5.8	: Relation between the spectral peak center wavelength and the compressive strain.....	87
Figure 6.1	: Schematic diagram of MSM structure.....	91
Figure 6.2	: Transmission spectrum of the MSM structure.....	92
Figure 6.3	: Experimental setup in detecting vibration using MSM sensor.....	93
Figure 6.4	: Photo image of the waveform of 4.0 kHz using digital oscilloscope.....	94
Figure 6.5	: Waveform Detection at different frequency: a) 20 Hz, b) 80 Hz, c)150 Hz, d) 300 Hz, e) 1kHz, f) 3 kHz, g) 6kHz.....	97
Figure 6.6	: Frequency Response : a) 20 Hz, b) 80 Hz, c)150 Hz, d) 300 Hz, e) 1kHz, f) 3 kHz, g) 6kHz.....	100

LIST OF TABLES

Table 3.1	: Summary of the optical and mechanical properties of CR-39 (Tondi, Kandelbauer, & Goodman, 2014)	41
Table 3.2	: Physical Dimension of MSM structures.....	56
Table 5.1	: Concrete mixture preparation per meter cube.....	79
Table 6.1	: Relative error of frequency measurement.....	101

University of Malaya

LIST OF SYMBOLS AND ABBREVIATIONS

BPM	Beam Propagation Method
EM	Electromagnetic
FBG	Fiber Bragg Grating
MMI	Multimode Interference
SMF	Single mode Fiber
SMS	Single mode multimode single mode
SHM	Structural Health Monitoring
MMF	Multimode Fiber
LG	Long gratings
MSM	Multimode single mode multimode
MF	Magnetic fluid
ASE	Amplified spontaneous emission
DAQ	Data Acquisition
OSA	Optical Spectrum Analyzer
PM	Polarization Maintaining

LIST OF APPENDICES

Appendix A: List of Publications and Papers Presented	105
Appendix B: Bibliography	108

University of Malaya

CHAPTER 1: INTRODUCTION

1.1 Research Background

Structural Health Monitoring (SHM) is an extensive, all-inclusive method of tracking the multiple kinds of damage and issues in various engineering fields. It provides systematic procedures of an efficient damage detection system for civil, aviation and mechanical engineering infrastructure. The complete SHM process as illustrated in Figure 1.1 involves the observation of a system based on periodical measurement of sensors, the isolation of the damage- sensitive elements from these measurements, and the execution of statistical analysis to predict the system's health. The SHM system uses non-destruction inspection technique to detect and monitor the current state of a structure. It provides ongoing real-time information on that structure, so any necessary action can be taken to prevent structural deterioration. Different types of structural analysis and failure models are incorporated with the information acquired from embedded sensors in order to assess a structure's current situation. The SHM system also provides a probable prediction of the remaining life time of the structure. In the context of civil engineering, the SHM refers to material shift, internal status deterioration, and property modification owing to changes in external conditions in different kinds of structures. There is a critical interest for SHM systems in civil infrastructure since structural performance can be degraded over certain time and lead to malfunctions.

Sensors are playing essential roles in SHM system as they provide inputs of the structure identification and inspection to enhance safety and reliability. The sensors used in SHM must be reliable and accurate in monitoring and detecting without causing any damage to the host. They can identify structural damages such as physical crack, structural deformation and loose structural bonding. They should also be robust to weak signal to identify the damage in these infrastructures under monitoring.

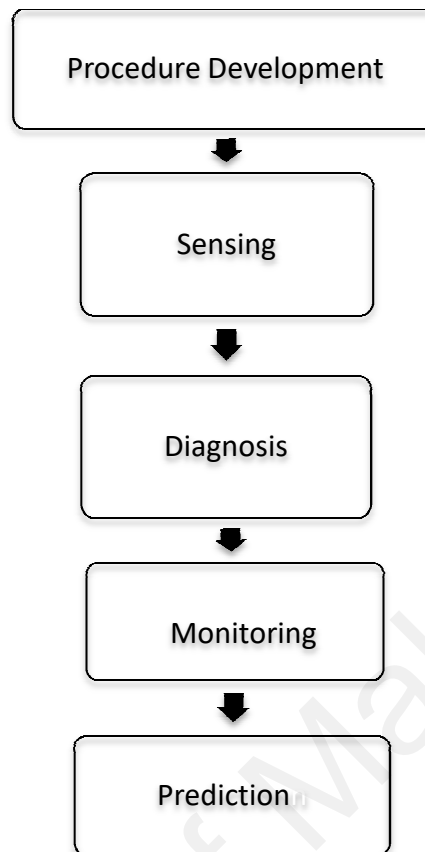


Figure 1.1: Main Processes in SHM

Many SHM systems were fitted with low cost electrical strain gauges in past decades. These strain gauges are very common in SHM because they are cheap, simple to mount and have excellent sensitivity to detect a structure's prospective risk or damage. Corrosion rate meter comprises of the polarization resistance sensor used for the corrosion monitoring of the reinforced steel. The evaluation of the remaining load-bearing ability was described based on the quantification of the real degree of corrosion (Andrade & Alonso, 2001). An impedance measuring system for non-invasive SHM system based on Pblead Zirconate Titanate (PZT) was recently reported by Antunes et al. in 2019. PZT piezoelectric transducers are attached to the structure to monitor its mechanical impedance through measuring the electrical impedance. The PZT devices are cheap, tiny, light weight, involve low energy, are less susceptible to variability in

temperature, and provide a linear response under low electric field. Nonetheless, there is still a demand for alternative because of their inabilities to oppose from corrosion, electromagnetic obstruction (EMI) and water shorting.

In recent, fiber optic sensors have arisen as a significant technique for assessing structural health. The optical fiber sensors have favorable demands in replacing the electrical strain gauge as optical fiber sensors offer low cost in fabrication, highly insusceptible to electromagnetic obstruction and light weight. Many works have developed different sensor schemes to provide virtual measurements for any interest parameters (Antunes et al., 2019; W. Yang et al., 2019). Fiber optics technology offers better solution for sensing applications such as a single optical fiber may substitute a large number of discrete electrical and mechanical sensors. The solution is cost effective and able to sustain harsh environmental usage.

Both the SMS and MSM have demonstrated reliable properties as optical sensors in the pasts where its applications in heavy civil structures in measuring strain and vibration have not been well developed and investigated. This research contribution will bring benefits in civil engineering field where better sensor alternatives are required to suit specific applications where other existing sensors unable to satisfy the specifications.

1.2 Problem statements and scope of work

The SMS and MSM working principle are largely different as compared to Fiber Bragg Grating (FBG) although they possess similar properties such as response linearly to strain. However, there are still unexplored properties of the sensor that been covered in this research work. Designing the packaging method, setup and sensor characterization is essential to find its usefulness and effectiveness in strain measurement in civil infrastructures. One of the challenges of utilizing the SMS is to make sure that the sensor probe is installed in a straight manner in order to provide

linear bending when strain is applied on the heavy civil structure. Since the MMF section can be conveniently cleaved and fusion spliced in a short segment, there is a tendency that the MMF section is not straight during sensor installation. Another challenge is that the fiber is easily broken in harsh environment as its material is silica glass. Thus, installation and packaging method of the sensor must be well developed to protect the fiber. Moreover, the sensor probe requires sufficient bending for it to provide linear strain response which was not mentioned by many researchers in the past. Hence, sensor probe with insufficient bending or strain will lead to non-linear response. For that reason, designing the packaged sensor probe to detect the applied load on the heavy civil structure is critical to solve this issue.

1.3 Research objectives

This research embarks on the following objectives:

- a) To investigate the use of a packaged SMS fiber structure with polymer plastic as water wave gauge in the laboratory hydraulic tank
- b) To investigate the strain dependence of the spectral response of a SMS fiber structure on the reinforced concrete beam
- c) To investigate the use of a MSM structure to detect vibration frequency for mechanical vibration.

1.4 Significance of study

The current FBG optic technology has achieved specialized development, quality, and cost viability that they are commercialized and replacing conventional sensors to measure strain, temperature, humidity, position and vibration. Fiber optic sensors possess many advantages of light and portable dimension, low power consumption and immunity to EM interference. The significance of this research study is to examine the performance of the multimode interference structures as optical sensors to measure strain and vibrations on heavy civil structure respectively. The proposed multimode interference structures provide an alternative to substitute FBG in measuring strain for higher sensitivity, lower cost and the ease to fabricate the structure.

1.5 Outline of Thesis

This thesis presents the work on development of MMI-based fiber sensor for structural health monitoring, with comprehensive works which include fabrication, characterization and testing of the sensor probe on the civil infrastructures. The properties, advantages and limitations of these structures were investigated with respect to its operation principle. The thesis consists of seven (7) chapters.

Chapter 1 is an introductory section which initiates a brief background on the importance of SHM, motivations, objectives of the research and also outlines of the thesis. Then, Chapter 2 provides a brief description on commercialized and widely used fiber grating (FBG) optical fiber and its sensing applications. In particular, it describes principle of self-imaging based on the MMI effect in optical fiber. Two MMI-based fiber structures are described in this chapter, namely SMS and MSM. The discussion is further made for these structures with their sensing applications.

Chapter 3 describes the fabrication of SMS and MSM structures and also includes the detailed characterizations of these two sensor probes. The investigation on sensor sensitivities to physical conditions such as temperature and packaging is elaborated in this section. Investigations of temperature dependence of the spectral characteristics of SMS and MSM probe are also elaborated. Then, characterizations of the packaged SMS structure are included with experimental investigations on linear response to the applied load.

In Chapter 4, a packaged SMS fiber structure was experimentally tested in a laboratory water flume to gauge water waves. The experimental results are discussed in this chapter and summarized that the packaged SMS structure was capable of serving as a wave gauge at relatively high sensitivity.

Chapter 5 describes the straight SMS structure used as compressive strain sensor on the reinforced concrete beams. The discussion on the experimental work involving fabrication of standard reinforced concrete beam and strain testing. Then, the findings discussed the sensitivity on the compressive strain measurement using the SMS sensor probe.

Chapter 6 discusses on the development and testing of a frequency vibration sensor based on MSM configuration. This chapter explains the laboratory setup to test the capability of the MSM structure to detect the vibration frequency in the frequency range from 20 Hz to 6 kHz. The time domain measurements were converted to Fast Fourier Transform (FFT) to acquire the vibration frequency. Finally, overall conclusions arising from this work are presented in Chapter 7. The proposed structure-based SMS and MSM sensors for SHM applications will be concluded with key findings and also proposal of future work on enhancing the packaging of the optical sensor probe.

CHAPTER 2: LITERATURE REVIEW

2.1 Introduction

There is a critical concern in civil infrastructure for SHM schemes as structural performance can be degraded over certain duration and prone to breakdowns. Due to its capacity to detect structural problems for performance assessment and maintenance, electrical strain gauges have been employed for many years in SHM scheme. However, owing to their inability to withstand corrosion, electromagnetic wave interference (EMI) and water shorting (Bremer et al., 2016), there is still a need for an alternative approach.

The optical fiber sensors then have favorable requirements to replace the electrical strain gauge as optical fiber sensors offer low manufacturing costs and are extremely resistant to electromagnetic interference. Various works have created many optical fiber sensor systems for detection of any physical and chemical parameter. Fiber optics technique provides the distinctive potential to assess on a distributed basis with having a single optical fiber to substitute large numbers of discrete sensors. This feature has the potential to reduce the cost and complexity of a sensor system when a large number of measuring points are required.

2.2 Fiber Bragg Gratings and its Applications

Fiber optic sensors (FOS) has been popular used in monitoring the health of the civil infrastructure due to its ability to overcome the shortcomings of the electrical strain gauge. Particularly, the FBG optical sensor has emerged as an accurate and reliable mechanism in SHM of civil infrastructures such as tunnels, tall buildings, bridges, hydro dams, roadways and pipelines. FBGs have exhibited numerous of advantages due to its working mechanism that is detecting wavelength shift, the ability to provide good response to strain, large scale production, simplicity of multiplexing, remote detecting and accurate measurement (Cazzulani et. al, 2014; Majumder et. al, 2008). For

structural health monitoring applications, one of the greatest benefits of FBG devices over other accessible strain or temperature sensors is that they can be multiplexed into a big sensor network. With a single or restricted entry points and lead wires, structural safety surveillance applications have a remarkable benefit with reduced external disturbance of lead wires.

A FBG is fabricated by modifying a single-mode optical with a UV laser. As light travels along the fiber, the Bragg grating which creates periodic or variations in the refractive index, reflects a narrow single wavelength, whereas allows transmission of other wavelengths through the grating (Meltz, et al., 1989) .

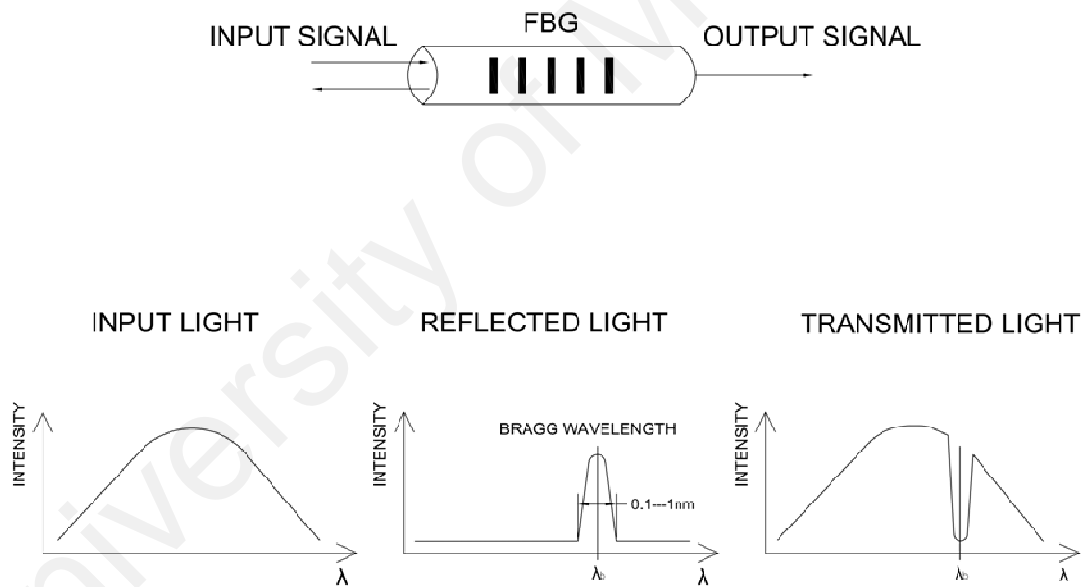


Figure 2.1: Spectra Response of a FBG (Majumder et al., 2008)

Based on Figure 2.1, the Bragg wavelength, λ_b is the center of wavelength in the reflection spectrum and it is mathematically derived as (2.1)

$$\lambda_b = 2\eta_{eff}\Lambda \quad (2.1)$$

Where Λ is the grating period and η_{eff} is the effective index. When any stress

applied with constant temperature, the period of FBG varies and causes a wavelength shift which is detected by an interrogator. The relative changes Bragg wavelength is then expressed as Equation 2-2:

$$\frac{\Delta\lambda_b}{\lambda_b} = \left(1 - \frac{\eta_{eff}}{2} [\rho_{12} - \nu(\rho_{11} + \rho_{12})]\right)\epsilon \quad (2.2)$$

Where ρ_{12} & ρ_{11} are photo elastic tensor components, ϵ is longitudinal strain on the FBG and ν is the Poisson's ratio. Normally, strain sensitivity is around 1.2 pm/ μ strain and Λ is approximately 500nm at 1550 nm band (Zujie et. al, 2012). When the grating period is in the range of sub-millimeter, a long period fiber grating (LPFG) is made at which the grating couples the core mode with the cladding modes (Bhatia & Vengsarkar, 1996; Stephen & Ralph, 2003).

FBG sensors are likewise delicate to temperature variations as the grating period and index modulation amplitude are function of both temperature and strain values. The relative change in Bragg wavelength due to temperature variations is derived as Equation 2-3. The ratio of the change in the normalized refractive index of silica ($5 - 10 \times 10^{-6} \text{ } ^\circ\text{C}^{-1}$) and the expansion of thermal expansion coefficient of silica ($\sim 5.2 \times 10^{-7} \text{ } ^\circ\text{C}^{-1}$) is leading to $\xi \approx 5.52 - 10 \times 10^{-6} \text{ } ^\circ\text{C}^{-1}$.

$$\frac{\Delta\lambda_b}{\lambda_b} = (\alpha + \beta)\Delta T \quad (2.3)$$

Where β is the thermo optic coefficient, α is the thermal expansion and ΔT is the temperature changes. It is obvious that the response of the Bragg wavelength is significantly affected by thermal factor with approximation of 10%. Thus, it is necessary to compensate the effects of temperature changes on the Bragg wavelength. The simplest technique used to compensate the temperature effects is to provide two separate FBG sensors for strain and temperature measurement respectively (Frank et al., 1998) . However, the interrogation of the two sensors are difficult and complex.

A FBG sensing system requires an interrogator in order to obtain and interpret data from each sensor. Several methods have been implemented to multiplexing big FBG sensor networks where devices are interrogated using wavelength division multiplexing (WDM) and time division multiplexing (TDM). For WDM applications, the reduction of wavelength separation between each of the FBGs reduces the time necessary for scanning the network. A wide range of multiplexed detectors should be used for low-reflectivity TDM implementations. When having both WDM and TDM combined, the power loss can be reduced by FBG and the total wavelength spectrum screened to interrogate the whole network is reduced (Kersey et al., 1997).

Despite the uniform grating on FBG, numerous fiber gratings such as chirped, apodized, sampled and phase-shift grating, have been designed to accommodate different demands and applications. Chirped fiber Bragg grating (CFBG) (Kashyap, 2010) is created with a linear period variation along the fiber. It demonstrates the reflected spectrum to broaden significantly as grating period reflects light of different wavelengths at distinguished positions. CFBG is useful fiber communications and laser technologies (Hill et al., 1994; R. Sun et al., 2016), as such they are often used as filters (Q. Wu et al., 2010) or interrogators (Chitchebakov & Swart, 2004).

Another special FBG structure is tilted gratings (TFBG) which the grating is at particular phase angle. The grating is designed at angle which is to the respect to the optical axis. This structure enables coupling of the propagated light at outside of the fiber core, which then makes TFBG commonly used in most optical interrogation system (Suo et al., 2008).

2.3 Multimode Interference in Optical Fiber

The phenomenon of interference is the resultant of at least two or more waves superposing and forming one single wave. The wave propagating along a multimodal waveguide is undergoing image replication in periodic intervals. The image replication is formed by destructive and constructive interferences between the propagated waves.

2.3.1 Self-imaging principle in MMI structure

Self- imaging is a multimode waveguide property that aids to reproduce the input field profile of the single or multiple images at periodical intervals along the guided propagation path. The principle of self-imaging in uniform index slab waveguides was first proposed by Bryngdahl (1973). Figure 2.2 illustrates the formation of Fresnel images when self-imaging phenomenon took place.

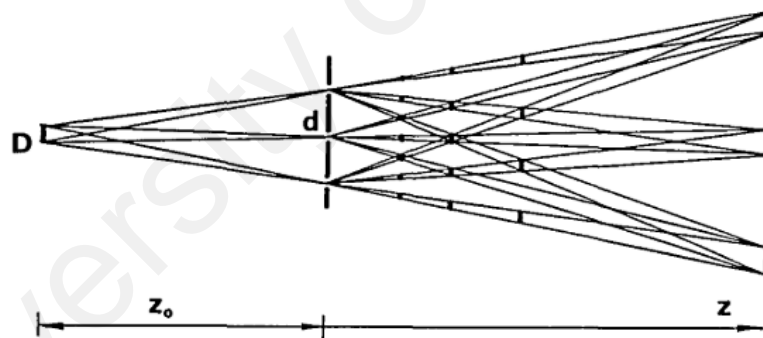


Figure 2.2: Formation of Fresnel images (Bryngdahl, 1973)

Once an object is illuminated periodically in two orthogonal directions with collimated light, Fresnel images of periodic object will be formed in planes at distance, z from the object. The distance, z can be described as:

$$z = \frac{2vd^2}{\lambda} \quad (2.4)$$

Where d is the period, λ is the wavelength of the collimated light, z is the distance and v is the integer of object. When the object array is illuminated by a point source that is located in distance z_0 from the object, Fourier images for the square array is obtained using:

$$\frac{1}{z_0} + \frac{1}{z} = \frac{\lambda}{2vd^2} \quad (2.5)$$

An MMI device as shown in Figure 2.3 comprises of two parts, which are the access waveguide and center multimode waveguide. For instance, the SMS structure is a multimode waveguide which the access waveguide is SMF and meanwhile, the multimode waveguide is MMF. Normally, the single mode waveguide is used as an access waveguide. Light will be launched from single mode waveguide into a multimode waveguide and then recoupled the light when it reentered single mode waveguide. Multimode interference (MMI) occurs when a wave propagating at the interface of SMF-MMF. Because of the MMF's core diameter, the entrance wave is replicated into many higher order modes. When these waves leave MMF, they sum up and propagate energy from distinct media through the SMF.

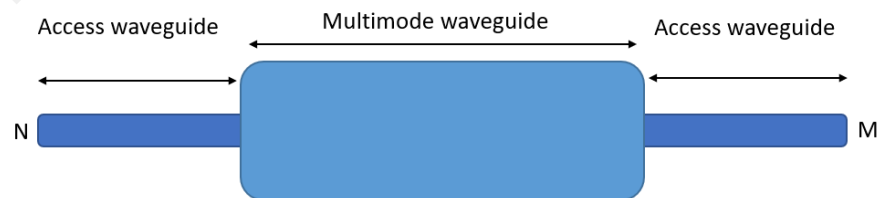


Figure 2.3: MMI device.

The MMI device is not only limited to SMS structure. It can also be assembled with an MMI coupler, where there will be more than one input and output access waveguide. This type of coupling is referred to as $N \times M$ MMI couplers, where the N and M refer to input access waveguide and output access waveguide respectively. The central multimode waveguide is usually designed to support large number of modes.

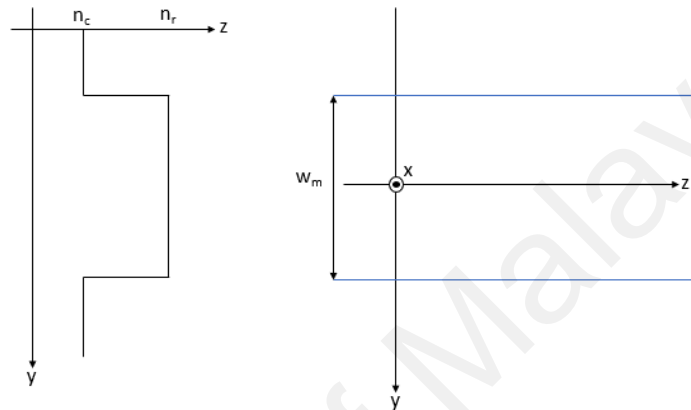


Figure 2.4: 2D representation of the step-index multimode waveguide (Soldano & Pennings, 1995)

Figure 2.4 illustrates the step index multimode waveguide, where W_m is the multimode waveguide width, n_r is the ridge effective refractive index, n_c is the cladding effective refractive index. The waveguide as shown in Figure 2.5 has m modes, which illustrates the guided modes from 0 to 8 in step-index multimode waveguide.

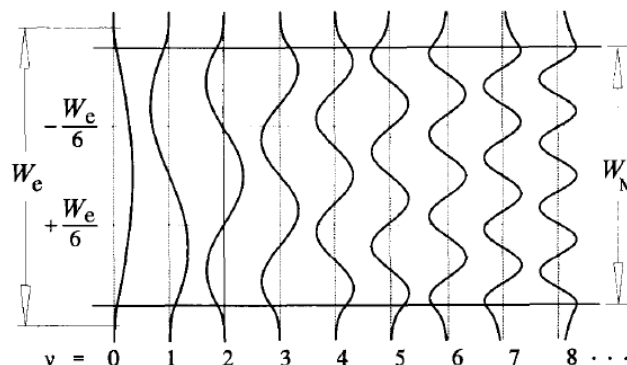


Figure 2.5: Amplitude-normalized lateral field profile (Soldano & Pennings, 1995)

The equation below shows the relationship between the propagation constant, β_v and lateral wavenumber, k_{yv} and the ridge index, n_r .

$$k_{yv}^2 + \beta_v^2 = \left(\frac{2\pi}{\lambda_0}\right)^2 n_r^2 \quad (2.6)$$

Where v is mode numbers, λ_0 is the free space wavelength. Meanwhile, lateral wavenumber, k_{yv} is related to the lateral penetration depth, W_{ev} as described in (2.7).

$$k_{yv} = \frac{(v+1)\pi}{W_{ev}} \quad (2.7)$$

If the waveguide become high in contrast, W_{ev} will be approximated to multimode waveguide width, W_m . Then, the lateral penetration depth, W_{ev} can be approximated by the width corresponding to the fundamental modes, W_e only as using (2.8).

$$W_e = W_M + \left(\frac{\lambda_0}{\pi}\right) \left(\frac{n_c}{n_r}\right)^{2\sigma} (n_r^2 - n_c^2)^{-\frac{1}{2}} \quad (2.8)$$

Where $\sigma = 0$ is for TE (Transverse Electric Modes) and $\sigma = 1$ is for TM (Transverse Magnetic Modes). The propagation constants, β_v is deduced from equation (2.6) and (2.7). The β_v in the step index multimode waveguide displays an almost quadratic on the mode number, v .

$$\beta_v \simeq k_0 n_r - \frac{(v+1)^2 \pi \lambda_0}{4 n_r W_e^2} \quad (2.9)$$

The beat length, L_π is obtained from the first 2 lowest order modes and is expressed as (2.10)

$$L_{\pi} = \frac{4n_r W_e^2}{3\lambda_0} \quad (2.10)$$

The space between the propagation constants can be described as (2.11):

$$(\beta_0 - \beta_v) \simeq \frac{v(v+2)\pi}{3L_{\pi}} \quad (2.11)$$

Based on a guided-mode propagation assessment, the MMF input field profile at when $z=0$ is written as

$$\Psi(\mathbf{y}, \mathbf{0}) = \sum_v c_v \psi_v(\mathbf{y}) \quad (2.12)$$

where $\psi_v(\mathbf{y})$ is the field distribution of LP_{0m} with \mathbf{y} , the radial direction in the cross-section of fiber and c_v is the excitation coefficient of each mode, which can be calculated using overlap integrals based on the field orthogonality connection of both $\Psi(\mathbf{y}, 0)$ and $\psi_v(\mathbf{y})$, which can be represented as orthogonal relationship in Equation (2.13).

$$c_v = \frac{\int \Psi(\mathbf{y}, \mathbf{0}) \psi_v(\mathbf{y}) d\mathbf{y}}{\sqrt{\int \psi_v^2(\mathbf{y}) d\mathbf{y}}} \quad (2.13)$$

The field profile at distance of z is superposing all the guided mode distributions and can be written as (2.14). When light is launched from the MMF section into the output SMF, the eigenmodes within the MMF are recoupled into the SMF fundamental mode.

$$\Psi(\mathbf{y}, z) = \sum_{v=0}^{m-1} c_v \psi_v(\mathbf{y}) \exp[j(\omega t - \beta_v z)] \quad (2.14)$$

The field profile, $\Psi(\mathbf{y}, z)$ is then deduced as (2.15) with the angular phase of the fundamental mode of the field is taken out and assumption made with the $\exp(j\omega t)$ has been implicit.

$$\Psi(\mathbf{y}, z) = \sum_{v=0}^{m-1} c_v \psi_v(\mathbf{y}) \exp[j((\beta_0 - \beta_v)z)] \quad (2.15)$$

When z is replaced with the length of MMF as L , the field profile is described as (2.16).

The field profile, $\Psi(y, z)$ represents the self-imaging of the input field, $\Psi(y, 0)$.

$$\Psi(y, z) = \sum_{v=0}^{m-1} c_v \psi_v(y) \exp\left[j \frac{v(v+2)\pi}{3L\pi} L\right] \quad (2.16)$$

Where the mode phase factor, \emptyset is expressed as below:

$$\emptyset = \exp\left[j \frac{v(v+2)\pi}{3L\pi} L\right] \quad (2.17)$$

In order to have $\Psi(y, z)$ as an image of $\Psi(y, 0)$, the mode phase factor, \emptyset must be unity. There are two conditions that needed to be fulfilled. The first condition is that every single mode, experiencing phase changes along L with value of multiple of 2π . Every guided mode that has similar phase with $z=0$ will experience a direct duplicate of input field. Furthermore, the second condition requires that the phase change must be even and odd multiples of π to ensure that the phase change is alternative. The length, L for the occurrence of self-images (Soldano & Pennings, 1995) is expressed as below:

$$L = p(3L\pi) \quad \text{with} \quad p = 0,1,2, \dots \quad (2.18)$$

By using equation (2.18), the required length of MMF to form the self-images of the input profile at the output, can be found easily. However, the formation of self images at different light wavelength will varies in coupled intensity along the L .

2.3.2 Single mode Multimode Single mode (SMS) Structure

Due to the implementation of FBG sensors in SHM which require complex interrogation (Y. Zhao & Liao, 2004), multimode-based optical fiber sensors such as SMS fiber structure have been explored and reported in many sensing applications such as displacement (A. Mehta, 2003; Q. Wu et al., 2011), refractive index (P. Wang et al.,

2011; Y. Zhang, Zhou, et al., 2014), pressure (May-Arrijoja et. al, 2016), vibration (Q. Wu et al., 2014; Y. Zhao et al.,2014) , strain, temperature (Tripathi et al., 2009) and etc. As compared to FBG sensors, the SMS sensors are easier to fabricate and does not need a complex interrogator in measurement. It was revealed that the capability of SMS sensor is compatible to FBG sensor as it caters similar performances in strain and temperature measurements (Q. Wu et al., 2009). SMS fiber optic structure is created by fusion splicing both terminals of the small segment of MMF with bare SMF.

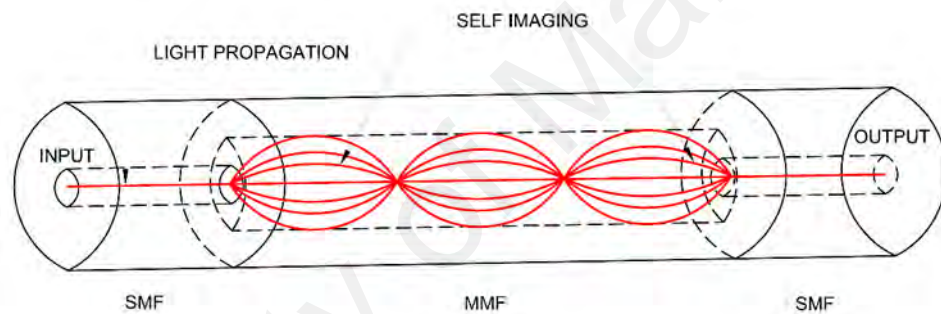


Figure 2.6: Schematic diagram of a SMS fiber structure

Figure 2.6 indicates a SMS fiber structure's schematic diagram. The SMS fiber sandwiches a portion of the step index MMF. Due to the wider core diameter of the MMF, when light enters along the straight SMS structure, moving from SMF to MMF input, multiple eigenmodes will be excited in the MMF segment, causing the phenomenon of modal interferences (MMI). The interferences result from the superimposition of two or more waves. Only at the MMF and SMF joint, the light will be recoupled into the output SMF. In a multimodal waveguide, the input light field is replicated periodically in multiple images along the multimodal waveguide. This MMI is based on the self –imaging phenomenon.

2.3.3 Multimode Single-mode Multi mode Structure (MSM)

The fusion splicing the two sides of the SMF with two short segments of MMF constitutes another configuration that is based on the mode interference concept. This structure is referred as MSM. This configuration displays a homogeneous interference fringe between core and cladding modes that MMF will combine some energy in the SMF into fewer modes. Because of its enormous variations in effective index between core and cladding mode, this MSM design is particularly useful for detecting applications such as strain detection and temperature monitoring (Q. Wu et al., 2015; Yin et al., 2016), magnetic field (Tang et al., 2014), vibration and etc.

The MSM structure diagram is shown in Figure 2.7. When light propagates from MMF to SMF, a portion of light spreads to the cladding layer of SMF as the core diameter of the MMF is much bigger than the core of the MMF. However, after passing through the second MMF, light from both core and cladding modes will be recoupled, forming linear modal interferences.

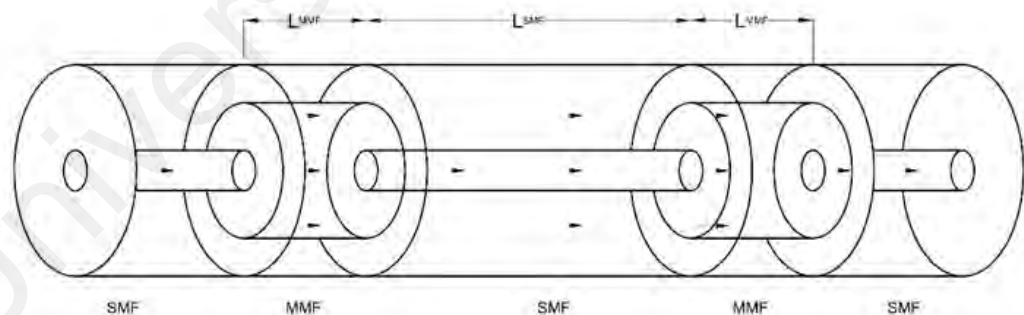


Figure 2.7: Schematic Diagram of MSM Structure

2.3.4 Review on MMI based optical fiber for sensing applications

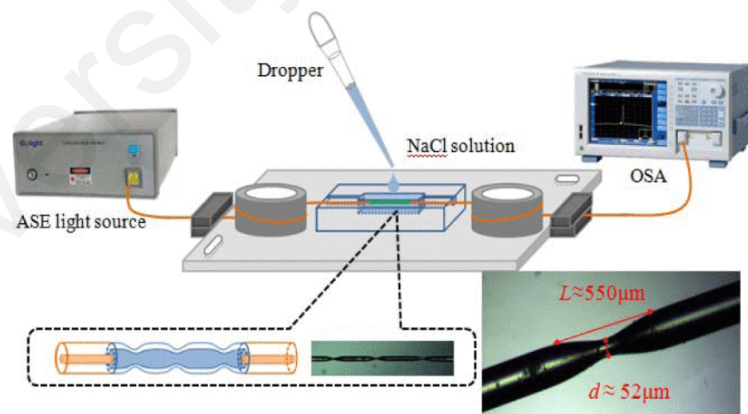
The MMI based optical fiber structures have extensively investigated and developed for optical sensing with the benefits of manufacturing ease, compact structures, electromagnetic immunity and elevated sensitivity in measurement. The MMI based optical fiber structures have been used for many sensing applications such as refractometer sensor (L. Li et al., 2012; Jieyuan Tang et al., 2017; W. Yang et al., 2019), temperature sensor, strain sensor, vibration sensor and magnetic field detector. The typical MMI based optical fiber structures are SMS and MSM structures. This section discusses on the related previous works on common sensing applications of the MMI based optical structures which exploit the mechanism of the multimodal interference for an improved performance.

2.3.4.1 Refractive Index Sensor

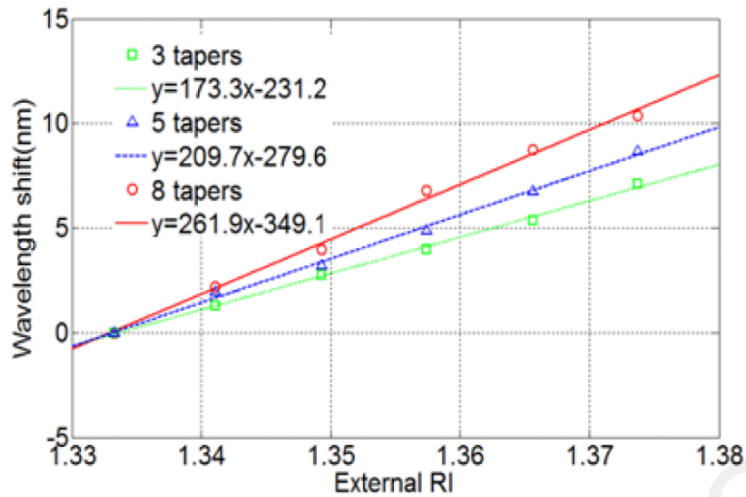
Refractive index sensing is one of popular applications in the biological, environment monitoring and chemical industry. A MMI based optical fiber structure was demonstrated by Villatoro and Monzon-Hernandez (2006) to produce the excitation of the SMF cladding modes via huge core diameter mismatch to provide measurement of refractive index. The MMI structure was constructed by fusion splicing the uncoated SMF in between two short MMF segments. Meanwhile, Y. Ma et al. (2012) proposed an in-fiber Mach-Zehnder interferometer with having MSM structure as sensing element to achieve high resolution of the refractive index measurement up to 7.1×10^{-5} within refractive index range of 1.33 to 1.40.

The SMS structure was also used for refractive index sensing by exposing the chemically etched MMF core to the surrounding medium to detect refractive index (Q. Wu et al., 2011). The refractometer exploits the multimode interference occurring in MMF. The propagation properties of the respective guided modes in the MMF will

change corresponding to the surrounding refractive index. However, the refractive index measurement range of the SMS structure is limited by the refractive index of the MMF core. Thus, Pengfei et al. (2011) demonstrated the tapered fiber as a refractive index detector. In order to achieve larger dynamic range in refractive index measurement, the MMF is tapered to provide thinner cladding layer to permit adequate power propagation in the MMF cladding. Meanwhile, Rong et al. (2012) experimentally proved a structure-based in-fiber refractometer that has a sandwiched SMF between two short segments of thin core fibers to increase the detection sensitivity. Another similar work on tapering the SMS structure to provide refractive index measurement was achieved by Y. Zhao, Cai, and Hu (2015). This work utilized the SMS structure with several tapers on the MMF to enhance the sensitivity of the refractive index measurement. The result as shown in Figure 2.8 shows that the higher number of tapers yield higher sensitivity in measurement because more evanescent wave was generated by the leaking of the higher order modes to the surrounding liquid along the tapered region.



(a)



(b)

Figure 2.8: a) Multi-tapered SMS structure b) Comparisons of wavelength shift for different number of tapers (Y. Zhao et al., 2015)

In the recent work, the SMS fiber structure is fabricated by polishing MMF via wheel polishing method (Jieyuan Tang et al., 2017). The polished MMF segment with controllable polishing depth was able to detect refractive index, which the sensitivity was comparable to the conventional chemical etched fiber structure (Qiang Wu et al., 2011).

There are also several works found on using the coreless fiber as refractive index sensor (Y. Li et al., 2014; Socorro et al., 2013). The configuration of the coreless fiber structure is similar with SMS structure with having two identical SMFs spliced in between the coreless fiber. The study showed that the sensitivity in refractive index measurement of the coreless fiber structure is not influenced by the length of the coreless fiber but is affected by the diameter of the coreless fiber (Y. Li et al., 2014). In recent work, Baharin et al. (2018) proposed an open cavity Mach-Zender interferometer based on the lateral offset of the coreless fiber. This structure was constructed by

splicing a segment of coreless fiber in between two segments of coreless fiber with lateral offset and obtained sensitivity of 750 nm/RIU. However, the proposed structure is difficult to fabricate and yield undesirable coupling loss. Thus, another work on open cavity Mach-Zender was then proposed by L. Wang et al. (2019). This structure was constructed based on the multimode interference coupling with having coreless fiber largely offset spliced in between two MMFs. The coupling technique is effective in reducing insertion loss significantly with high refractive index measurement.

2.3.4.2 Strain Sensor

Strain assessment plays a crucial role in SHM for many civil infrastructures. For elevated precision in strain measurement, strain detectors are therefore needed, especially in aviation, houses and bridges where sensing is vital. Among the existing strain sensing technologies, OFS such as FBGs have attracted many research attention (Chan et al., 2006; Y. B. Lin et al., 2005; Tjin et al., 2002). In 2001, FBG gauges were incorporated to the bridges concrete structure in Canada. These gauges were not only capable in measuring static load but also sensitive to measure dynamic loads on bridge elements. For over the past few years, the monitoring of the bridges structural health were performed with high reliability in a hostile condition (Tennyson et al., 2001) .

MMI based optical fiber structures have been also investigated for strain assessment because of its simple and low cost configuration. In 2001, A. Kumar et al. performed a theoretical analysis to investigate the strain detecting characteristics of a few-mode fiber due to the modal interference between the first two modes of an SMF (A. Kumar et al., 2001). Then, the work has been extended to investigate the modal interference behaviours of the SMS structure (A. Kumar et al., 2003). A strain detector relying on SMS fiber structure with graded index MMF was reported in 2007 (Y. Liu & Wei, 2007). The graded index MMF fiber functions as a comb filter that can be used for

instrumentation and telecommunications in fiber sensing and laser tuning. However, the proposed SMS structure has limited measurement applications as the structure is not compact. In 2010, Hatta et al. developed a ratio metric power measurement configuration using two identical SMS structures to measure strain and temperature respectively. The proposed scheme demonstrated the strain measurement up to 1000 $\mu\epsilon$ with minimized measurement error due to the temperature fluctuations.

Another MMI based optical fiber structure which is MSM structure can be also utilized for strain measurement. The MSM structure has MMI occurring in between core and cladding modes in the SMF. The MSM structure was wrapped around a polyurethane hollow column to form a sensing device for volume strain detection which may potentially use for earthquake detection (Z. Xu et al., 2013). Another work done by Q. Wu et al. (2015) utilized a SMF with FBG spliced to two MMFs to cater multiple sensing. The transmitted and reflected light of the structure distinguished the responses for strain and temperature. The MSM structure was further investigated on the strain and temperature sensing characteristics (Yin et al., 2016). The work demonstrated that the power distribution in the SMF is very much depending on the length of first MMF segment.

In 2017, Y. Sun et al. (2017) created a low cost and highly responsive optical fiber strain sensor using single mode twisted multimode single mode (STMS) framework as demonstrated in Figure 2.9. Due to the disturbance caused by twisting MMF, higher-order modes are brought into and change the MMF coupling process in which twisting transitions impact the strain sensitivities.

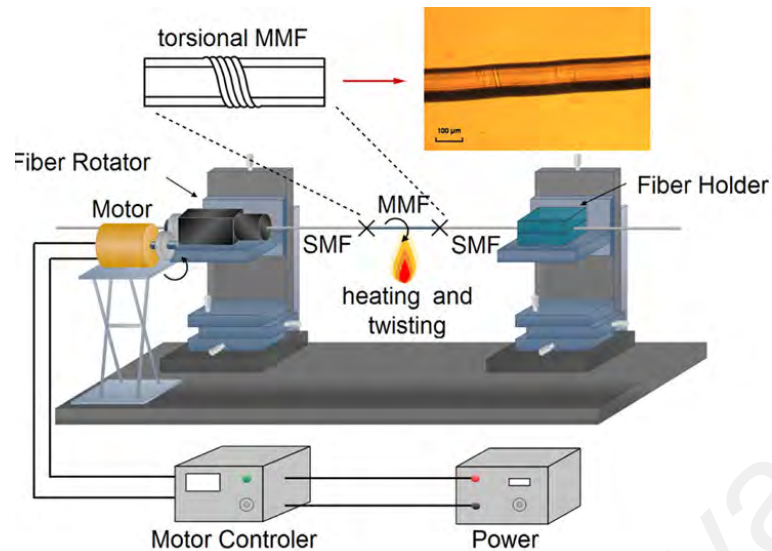


Figure 2.9 Laboratory setup for strain measurement using STMS structure (Y. Sun et al., 2017)

The MMI structure based on the polymer optical fiber was also used for strain measurement. Polymer MMF have been utilized for larger range of strain measurement up to $2 \times 10^4 \mu\epsilon$ sensing due to their large Young's Modulus elastic properties as compared to silica optical fibers (J. Huang et al., 2012). Similar work also found on the investigation of the strain sensing characteristics on a step-index polymer MMF (Becker et al., 2018).

Tian et. al modified the SMS structure to enhance the sensitivity of the strain measurement such as reshaping the structure into gourd shape. As shown in Figure 2.10, the MMF cladding was reformed to form MMI based FPI and obtained strain sensitivity of $-2.60 \text{ pm}/\mu\epsilon$. Meanwhile, Tian et al. also investigated the balloon-shaped SMS structure as displacement sensor. The structure was formed by bending SMS structure using capillary tube to fix the balloon shape and was capable to measure displacement with sensitivity of $0.51 \text{ dB}/\mu\text{m}$ (Tian et al., 2018). Another recent work published in 2018, S-tapered multimode (STM) structure was able to cater strain

measurement with high sensitivity up to $-103.8\text{pm}/\mu\epsilon$. However, this work requires the establishment of suitable axial offset of the STM structure in order to produce effective composite interference within the MMF section (Tian, Zhang, et al., 2018).

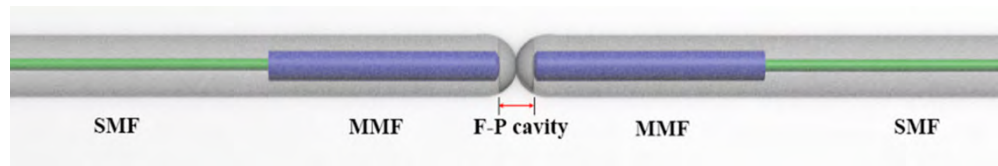


Figure 2.10: Schematic diagram of a gourd-shaped SMS structure (Tian et al., 2017)

2.3.4.3 Vibration Sensor

Detection of vibration is widely used for civil infrastructure health monitoring. The piezoelectric accelerometer has been used for vibration detection over past few decades till present. However, it is not suitable to be used in the electromagnetic sensitive environment. Thus, various fiber optic vibration sensing techniques have been extensively studied such as FBG (Bezombes et al., 2007; Z. Zhang & Liu, 2017), Fabry Perot interferometer (Z. Gong et al., 2017; L. Liu et al., 2016) and tapered fiber structure (B. Xu et al., 2012; Zhao et al., 2018).

Xu et al. demonstrated a tapered fiber Mach-Zehnder interferometer structure to detect vibration. The structure was able to measure broad frequency range up to 500 kHz (Y. Xu et al., 2013). A similar work on tapered SMS fiber structure was proposed to detect acoustic frequency up to 300Hz. The tapered SMS structure was constructed with having the MMF segment to be chemically etched to enhance the sensitivity in vibration measurement (R. Gao et al., 2018). However, these tapered fiber structures were difficult to fabricate due to the controllability of the desired diameter of the tapered fiber.

Among various fiber sensors, the SMS structure has also attracting many interest in using it for vibration detection. A vibration detector using the SMS fiber structure with particular predetermined MMF segment bending values was demonstrated by Q. Wu et al. in 2014. Figure 2.11 shows the experimental setup for the bent SMS structure. The vibration introduced to the SMS fiber structure will alter the bend radius and identify vibration frequencies and amplitudes up to 12 kHz in which the strength of the transferred optical power will differ. (Q. Wu et al., 2014).

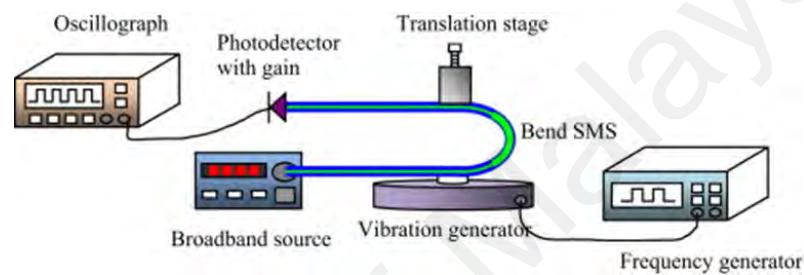
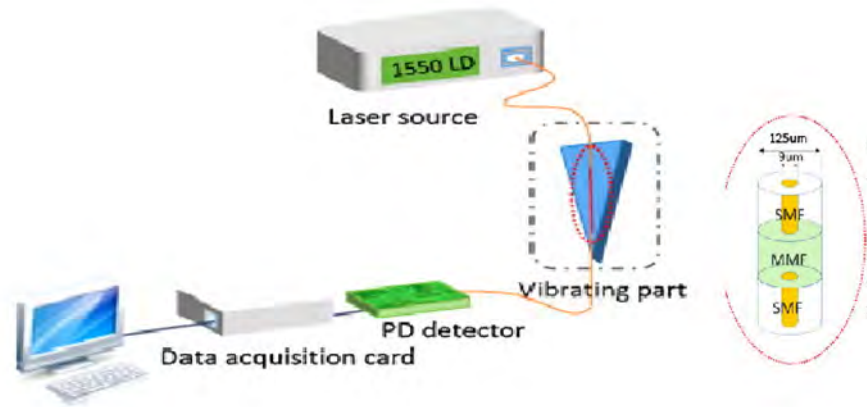
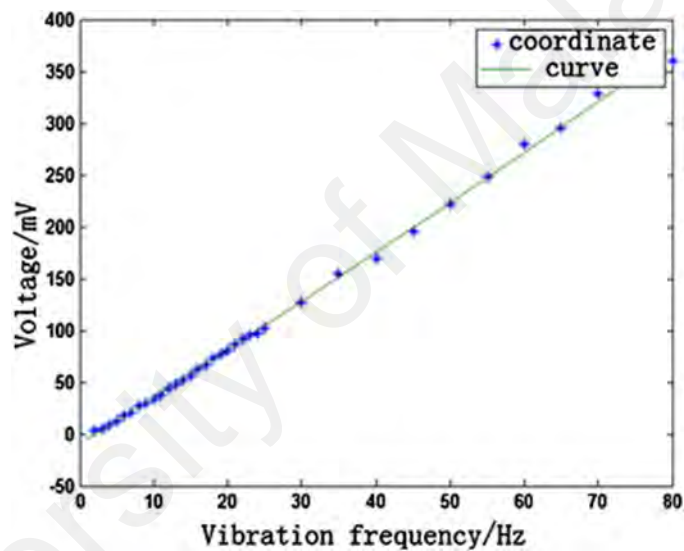


Figure 2.11: Experimental setup for bent SMS vibration sensing (Q. Wu et al., 2014)

Another research by Yong Zhao et al. (2014) demonstrated a vibration-sensing scheme relying on SMS fiber framework as illustrated in Figure 2.12(a). The origin of vibration is the contact in the loose end of a cantilever beam between the electromagnetic coils and permanent magnet pastes. When the frequency shifts, the identified voltage signal acquired by the lock-in amplifier will vary. The voltage has a linear connection with the vibration frequency difference can be observed from the graph as shown in Figure 2.12(b). The scheme can assess vibration frequency up to 80 Hz with a minimal level measurement error of 2% and a precision of 4.741 mV/Hz.



(a) Schematic diagram of the experimental setup



(b) Graph of output voltage of lock-in amplifier and vibration frequency

Figure 2.12: The vibration measurement system using SMS structure (Yong Zhao, Li, Meng, & Zhao, 2014)

The Butterfly-Shape Mach-Zehnder Interferometer is another MMI structure as a vibration fiber sensor. This sensor was proposed by Zhao et al. for low-frequency vibration sensing, in which the sensing component was tapped at the hollow core fiber. The results showed that low relative error in vibration frequency was obtained and as well as a vibration measurement tolerance of 13.575 dB/W under 50Hz vibration frequency (Yong Zhao et al., 2018).

In addition, Sun et al. proposed the MSM structure to be used as acoustic wave detector. The sensor utilized a thin aluminum foil to enhance the coupling efficiency between different modes, in which the proposed structure was capable to detect the acoustic wave up to 11 kHz (A. Sun et al., 2012).

2.3.4.4 Magnetic Field Sensor

Magnetic field detectors are essential for tracking civil infrastructure's magnetic field strength variability. In recent years, optical fiber magnetic field sensors have been investigated and explored as an alternative to the conventional electromagnetic current transformers due to their fiber strength, excellent insulation, compactness, and elevated sensitivity. The magnetic fluid (MF) was used to develop optical devices such as optical switches, tunable capacitors, modulators and magnetic field sensors because of its magneto-optical characteristics. Once an external magnetic field is introduced to the MF, the magnet particles alter the extinction factor of the MF, which the attenuation strength is depending on the evanescent field absorption factor of the MF (Fang, Xuan, & Li, 2013).

A magnetic field sensor was proposed by using MF as a cladding of MSM fiber structures for sensing magnetic fields up to 215pm/mT and 0.5742dB/mT at 1595 nm dip wavelength (Tang et al., 2014). MFs are also used as the cladding of SMS fiber structures to detect the magnetic field in many works. For instance, research works conducted by H. Huang et al. (2013), Chen et al. (2013), W. Lin et al. (2013) have demonstrated that SMS based fiber structure can delivers elevated efficiency of magnetic field detection. Luo et al. fabricated a SMS structure by fusion splicing the SMFs with large core offset. The structure was covered with Fe_3O_4 liquid and subjected to magnetic field. The work revealed that the SMS structure was able to detect magnetic field up to 110 Oe with notable changes in the wavelength shift and intensity of the

optical transmission spectrum. The proposed structure caters the sensitivity of 65.9 pm/Oe and 0.1185 dB/Oe for wavelength and intensity of the transmission spectrum respectively.

Zhang et al. realized a magnetic field sensor by combining the SMS structure with no core fiber. The sensor structure coated with EMG605 MF was experimentally investigated on the effect of the bending condition and also diameter of no core fiber on the sensor's performance. The bending sensor was able to perform an elevated sensitivity of 3185.2 pm/mT in the magnetic field range of 1.6 to 9.6 mT. In addition, the authors revealed that the smaller diameter of no core fiber yields better sensitivity in measurement.

Meanwhile, another similar work also demonstrated a MMI structure with no core fiber, which is immersed in an oil-based MF to measure magnetic field (Rao et al., 2017). The proposed structure has elevated sensitivity measurement up to 116.681 $\mu\text{m}/\text{RIU}$ due to the matching refractive index coupling. Under this condition, the guided modes in no core fiber segment becomes leaky and leading to a coupling transmission spectrum. In this work, the authors revealed that the length of the no core fiber has a negligible impact on the sensitivity of the proposed structure. In addition, the magnetic field sensor relying on the SMS framework with coreless fiber as the MMF immersed in MF was studied theoretically and experimentally in a recent work by Y. Huang et al. (2017). The recommended detector has encoding intensity characteristics, multiplexing intensity capacities and produces a high sensitivity value of 0.097 dB/Oe and a strong modulation depth of 78% in a comparatively linear spectrum.

2.3.4.5 Temperature Sensor

Temperature measurement is very important to monitor the health of the civil structures. Abnormal operating temperature detected on the civil structure may indicate the potential damage and degrading performances of the structure. The existing commercialized thermometers such as electrical temperature detector and thermal imaging camera are often used in temperature measurement for civil structural monitoring. However, these thermometers are highly affected to EMI and insusceptible to harsh environment. Thus, fiber optic temperature sensors are gaining interests due to its immunity to EMI and compactness.

A variety of optical fiber temperature sensors such as FBGs (Chen, X. et al., 2005) and LPGs (Gao et al., 2012; Bai et al., 2015) have been reported in the past decade. These FBG sensors are commonly coated with special material in order to increase its sensitivity in temperature measurements. The coating materials are usually Indium or any material that possesses large thermal expansion coefficient. The value should be greater than silica (Park et al., 2011; Wang et al., 2016). A work by Mishra et al. (2016) shows FBG sensor are coated with several coating materials. The result indicated that among all coating materials, the FBG coated with Polymethyle methacrylate provides significant enhancement of the temperature measurement sensitivity.

On the other hand, MMI optical fiber structures was also developed to use as temperature sensors. As compared to the FBG temperature sensors, the MMI based temperature sensors offers compatible sensitivity in temperature measurement with added advantage of ease in fabrication. Simple interferometer was accomplished in earlier work using a slight misalignment between two SMFs and a small core fiber stub that induces mode interference between core modes of LP01 and LP11 in a fiber core (Canning & Carter, 1997). Then, the interference in the MSM structure between

guided modes of a MMF has exhibited its capacity in temperature monitoring. Villatoro and Monzon-Hernandez (2006) used the MSM structure to function as a refractive index detector. The SMF's cladding modes were stimulated along MMF's big core diameter and displayed refractive index measurement around 1.450 with resolution up to 7×10^{-5} .

In another work by Nguyen et al. (2008), a temperature sensor based on MSM fiber structure in which able to measure elevated temperature up to 900 °C and cater high sensitivity in measurement of 0.088 nm/°C. The proposed sensor was designed to achieve clear inhomogeneous interference pattern with the excitation of cladding modes and largely interfered with core mode.

In 2015, Lin et al. conducted a numerical investigation on a MMI structure based temperature sensor with no core fiber. The effects of the temperature fluctuations on the wavelength shift of a single dip of the optical transmission spectrum was observed. The authors claimed that the proposed sensor has a larger wavelength shift which is 38.7 pm/ °C compared to the FBG based sensor which only has a wavelength shift of 11.5pm/ °C. Meanwhile, Chen et al. suggested measuring the distance of the wavelength shift of 2 dips. Both studies demonstrated that different methods in obtaining temperature parameter can be conducted in an optical sensor which provide alternative ways for researcher to conduct experiments

In addition, a liquid sealed fiber interferometer was recently developed by Bhardwaj and Singh (2017) and Su et al. (2019). Su et al. proposed an Isopropanol-sealed multimode microfiber to be used in detecting temperature, in which the Isopropanol is claimed to have a high thermo-optic coefficient. Due to this factor, the refractive index of this chemical changes along with the variation of surrounding temperatures.

A recent study by J. Yang et al. (2020) claims liquid filled fiber directional coupler was able to perform sensitivity up to 562.4 pm/°C in temperature measurement. The sensor was constructed with two cascaded SMFs with a liquid filled eccentric hole-assisted dual-core fiber, in which significantly change the light coupling between the center and suspended cores of the sensing element corresponding to the temperature changes.

University of Malaya

CHAPTER 3: FABRICATION AND CHARACTERIZATION OF SENSOR PROBE

Firstly, this chapter elaborates on the sensing principle of the SMS and MSM structures. These structures may act as sensor to detect any parameters changes as the output is depending on the concept of mode interference in optical fiber. Then, fabrication of SMS and MSM structures are further explained. The characteristics of the sensor probes fabricated with temperature variations are investigated experimentally. The making of packaged SMS structure in order to suit its application for load analysis is also further elaborated.

3.1 Construction and characterization of SMS sensor probe

3.1.1 Sensing principle of SMS structure

A SMS configuration is comprising of two SMFs which are fusion-spliced at both terminals of a short segment of MMF. The assumption is made that these fibers are aligned in axial. The sensitivity of transmission power is highly dependent on the length of MMF and the operating wavelength (Arun Kumar et al., 2003).

In the SMS structure, only the light with the smallest angle to the propagation axis can propagate along the SMF as the core radius is small. The light with the smallest angle to the axis is known as the fundamental mode. When light reaches at the SMF-MMF intersection, higher order eigenmodes are excited and formed a regular modal interference along the MMF with varying phase velocity. The distinction between the propagation constants of m and n modes is described as below (Gong Y. et al., 2011) :

$$(\beta_m - \beta_n) = \frac{\lambda(u_m^2 - u_n^2)}{4\pi a^2 n_c} \quad (3.1)$$

Where a is the core radius of the MMF and n_c is the refractive index of the core MMF. Meanwhile, both $u_m = \frac{\pi(4m-1)}{4}$ and $u_n = \frac{\pi(4n-1)}{4}$ the roots of the lowest order of Bessel function.

Due to occurrence of MMI in the MMF segment, the intensity of the light transmission reaches its critical value when the phase shift between two modes along the MMF equals to the multiples of 2π . The wavelength at dominant interference is determined as below:

$$\lambda = \frac{16Na^2n_c}{(m-n)(2(m+n)-1)L} \quad (3.2)$$

Where N is an integer (1, 2, 3 ...) and L is the effective length of MMF. The specific MMF length of the SMS structure may generate maximum or minimum MMI in its transmission spectrum. When an external perturbation such as strain, vibration or temperature applied to the SMS structure, there will be some changes in the fiber length, refractive index or core diameter (E. Li, 2007). These changes will lead to the changes in output spectral of the SMS structure. The relative wavelength shift due temperature changes is expressed as (3.3):

$$\frac{\Delta\lambda_1}{\lambda} = (\alpha_1 + \beta)\Delta T \quad (3.3)$$

Where as α_1 is the thermal expansion coefficient, β is the normalized thermo-optic coefficient of the MMF. Meanwhile, the strain induced wavelength shift in equation (3.4) at a constant temperature is due to the change of fiber dimensions and photoelastic effects.

$$\frac{\Delta\lambda_2}{\lambda} = \left(\frac{1}{n_c} \Delta n_c + \frac{2}{a} \Delta a + \frac{1}{L} \Delta L \right) \quad (3.4)$$

The relative refractive index changes of the core MMF due to strain can be derived as:

$$\frac{\Delta n_c}{n_c} = -\frac{n_c^2}{2}(p_{12} - \nu(p_{11} + p_{12}))\varepsilon = -p_e \varepsilon \quad (3.5)$$

Where p_{12} and p_{11} are the photoelastic coefficients, ν is the Poisson ratio of the fiber, ε is the strain and p_e is the effective photoelastic coefficient. Furthermore, the relative MMF core radius changes due to strain and the relative length changes due to strain can be derived as (3.6) and (3.7) respectively.

$$\frac{\Delta a}{a} = -\nu \varepsilon \quad (3.6)$$

$$\frac{\Delta L}{L} = \varepsilon \quad (3.7)$$

Therefore, the strain induced wavelength shift in equation (3.4) can be deduced as below:

$$\frac{\Delta \lambda_2}{\lambda} = -(1 + 2\nu + p_e)\varepsilon \quad (3.8)$$

The output power of the SMS structure as derived in equation (3.9) is depending on the relative phase difference between cladding and core modes along the MMF segment. Therefore, when an external force is applied on the SMS structure, the intensity of the transmission power will change accordingly to the corresponding propagating coefficients and the excitation of the eigenmodes along the MMF.

$$P_{out}(z) = \frac{|\int \Psi(y,z)\Psi(y,0)ydy|^2}{\int |\Psi(y,z)|^2(y)dy \int |\Psi(y,0)|^2(y)dy} \quad (3.9)$$

3.1.2 Fabrication of SMS sensor probe

The SMS fiber as shown in Figure 3.1 is built using a MMF segment with a 105 micron core size step index profile. To produce the SMS structure, the MMF is spliced to its terminals with SMF-28 fibers. The refractive cladding and core index of the SMF-

28 are 1.4447 and 1.4504 respectively at the operating wavelength of 1550 nm and its core diameter is 8.3 μm , Whereas the refractive cladding and core index are 1.4271 and 1.4446 respectively at 1550 nm wavelength and its core diameter is 105 μm . A reflective phenomenon of the SMF and MMF interface may occur owing to the refractive index mismatch. However, since the reflection causes very small return loss, it may be negligible during practical implementation (Q. Wang et al., 2008).

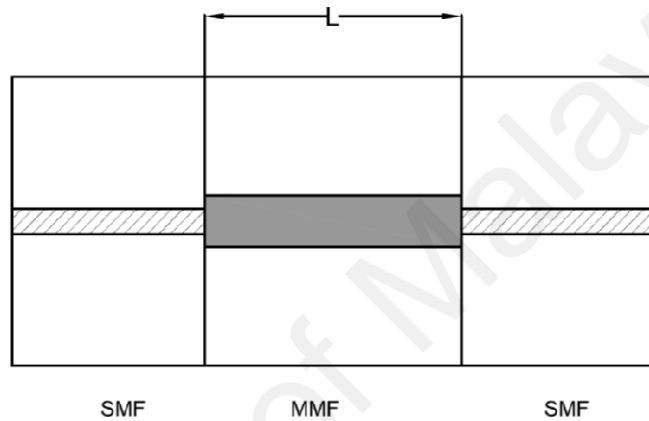


Figure 3.1: Schematic Diagram of the SMS structure

In order to construct the SMS structure, equation (3.10) can be used to determine the required length of the MMF segment for certain light wavelength, which will form a self-image of the field profile at the junction of the MMF and lead out SMF. If the wavelength is different from the wavelength used in the design, the corresponding self-images will be formed at different position along the MMF segment instead of the junction of the MMF and lead out SMF. The coupled intensity will decrease for the non-matching wavelength (May-Arrijoja et al., 2016). Therefore, the SMS structure is usually supplied by a broadband light source in order to observe the transmission spectra of the SMS structure.

$$L = \frac{4n_c D^2}{\lambda} \quad (3.10)$$

Where n_c is the effective refractive index of MMF, λ is the operating wavelength and D is the core diameter. The MMF length of 5.8 cm was proposed in the SMS structure at operating wavelength of 1550nm (Socorro et al., 2013). The optimal length of MMF is decided by the required or sufficient interference length to construct the SMS sensor probe for certain sensing application.

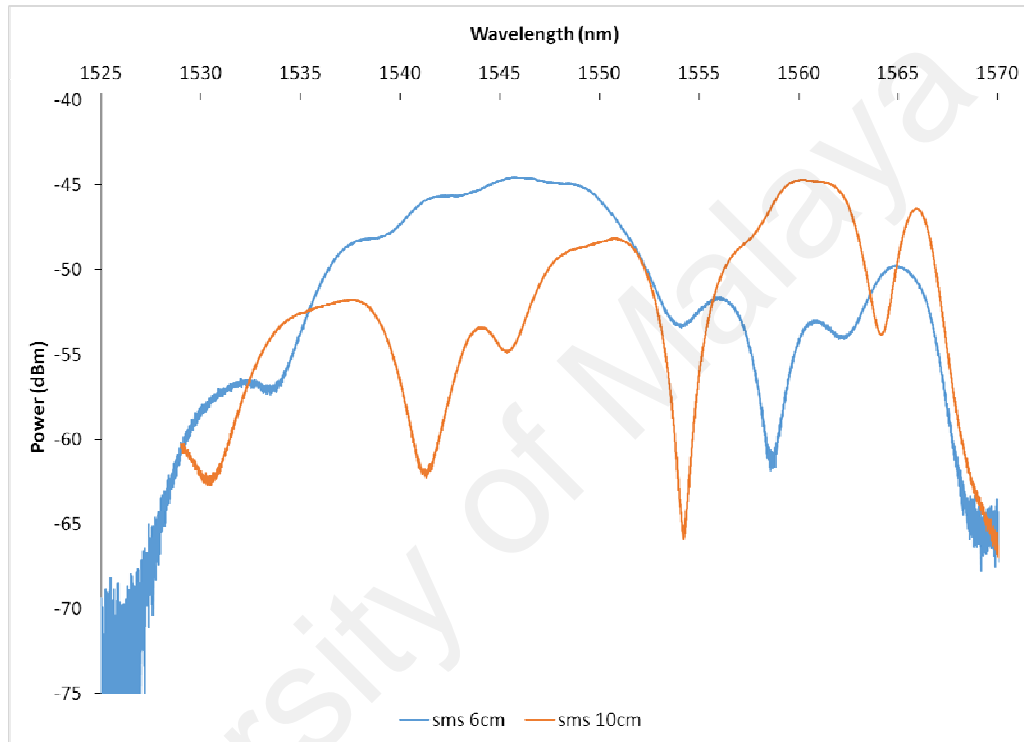


Figure 3.2: Power Spectrum of SMS structure with different MMF length

The SMS is connected to the amplified spontaneous broadband light source with central wavelength of 1550 nm. The output power spectrums was observed using an OSA. The output power spectrums for two distinct MMF length of the SMS structure are shown in Figure 3.2. The MMF length of 6 cm and 10 cm were used to develop the SMS sensor in order to investigate the transmission spectral characteristics. The difference of the two spectrums is noticeable as the interval of the various peaks of the output power decreases with the increase of the MMF length. This differences is due to

the light field variation of the MMF which caused by the different MMF length. Theoretically, the longer MMF segment will excites more cladding modes than the shorter MMF, the light spreads and converges while propagating along the MMF (Qian Wang et al., 2008).

3.1.3 Embedded SMS in Sandwiched Packaging

A straight SMS structure can acts as optical sensor like FBG for measurement of strain and vibration. However, the straight SMS structure provides very limited measurement as the fiber structure is possessing high risk in breakage when larger strain or vibration amplitude is applied to it. Thus, a bent SMS is a better solution to provide wider strain measurement and high resolution (Q. Wu et al., 2014). E. Li (2007) also demonstrated temperature compensation up to stability of 1pm/°C of SMS structure by using ceramic as packaging material.

The phenomenon of multimode excitation will occur at the MMF segment in a straight SMS structure. Due to the symmetrical refractive index along the propagation path, the light propagation in the straight MMF segment is symmetrically spread. For comparison, a curved MMF, the refractive index is asymmetrical along the fiber axis. Equation (3.11) is shown as the corresponding refractive index distribution for a bend MMF. Figure 3.3 shows the refractive index distribution of an unstressed, bent fiber and Figure 3.4 shows its corresponding straight fiber after conformal mapping. The refractive index of the conformal mapped fiber grows from the middle of curvature.

$$n = n_0 \left(1 + \frac{x}{R_{eff}} \right) \quad (3.11)$$

Where n_0 is refractive index and R_{eff} is its corresponding bend radius of straight SMS as expressed as equation (3.12);

$$R_{eff} = \frac{\theta}{1 - \left(\frac{n_0^2}{2}\right)[P_{12} - \nu(P_{11} + P_{12})]} \quad (3.12)$$

Where θ is the bend radius with ν , Poisson ratio and P_{11} and P_{12} , the photoelastic tensor components.

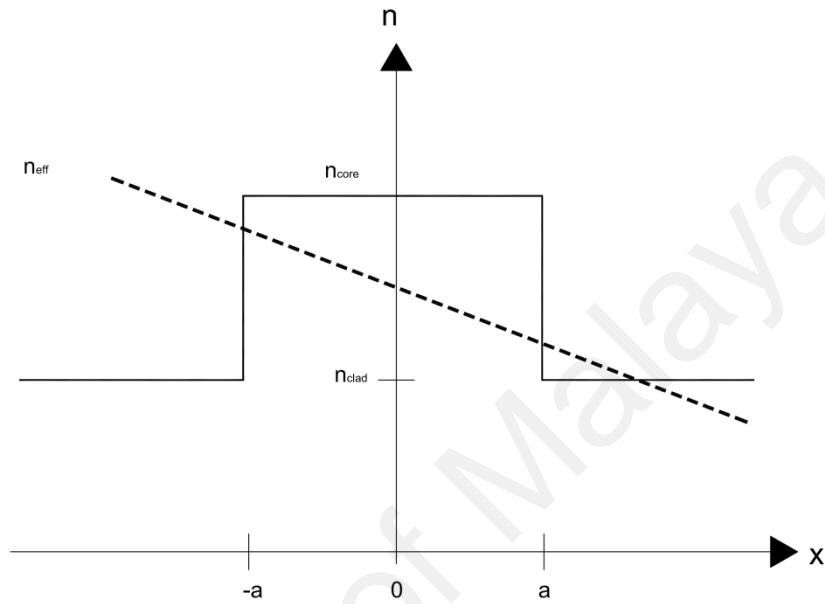


Figure 3.3: Refractive index distribution of a curved fiber

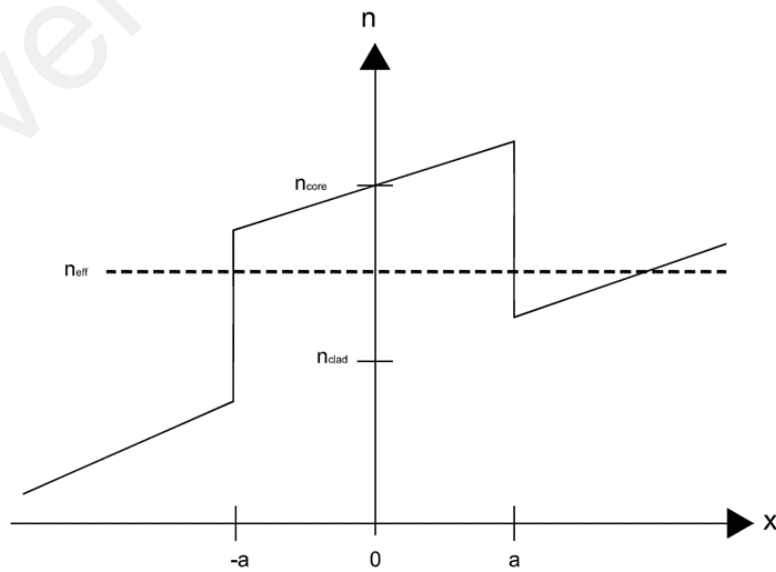


Figure 3.4: Refractive index distribution of an equivalent of a straight fiber

To reduce the impact of a SMS's high non-linear spectral output, a proper packaging is required to assist the SMS structure in bending linearly to respond to any load applied. The transmission characteristic due to the effective refractive index changes in the MMF depends primarily on the length of the MMF, its core size and its bending situation (Y. Gong et al., 2011). Since the transmission power of the SMS structure is sensitive to the selection of the working wavelength and also the length of the MMF, the design of the optical microbend sensor is essential (A. Kumar et al., 2003).

The SMS sensor probe is sandwiched between two plastic polymer sheets of CR-39. The dimensions of the CR-39 plastic polymer sheet are 5 mm thick, 40 mm wide, and 174 mm long. The CR-39 plate is also recognized as allyl diglycol carbonate. CR-39 is a plastic polymer widely used in eye glass lenses production. CR-39 is transparent in the visible spectrum and is nearly totally opaque in the ultraviolet range. It is made via polymerization of allyl diglycol carbonate (ADC) with initiator of diisopropyl peroxydicarbonate (IPP). The ADC monomer combines the optics of glass with the sturdiness of a thermoset material. It achieves fairly high abrasion resistance in which capable to withstand scratches.

Table 3.1 indicates the optical and mechanical properties of the plastic polymer sheet. CR-39 is approximately only 50% of the weight of glass with an index of refraction of 1.501. It possesses high Abbe numbers of 59.3 in which benefits to provide low chromatic aberration. The chromatic aberration is a distortion of the image due to the incapability of the lens to focus all shades onto the identical focal point. It can be used continually in temperatures up to 100 °C and withstand operation up to one hour at 130 °C (Tondi, Kandelbauer, & Goodman, 2014)

Table 3.1: Summary of the optical and mechanical properties of CR-39 (Tondi, Kandelbauer, & Goodman, 2014)

Property	Typical Values
Refractive Index (20° C)	1.501
Abbe Value	58
Transmittance (6.3 mm)	89 -92%
Specific Weight (25 ° C)	1.31 g/cm ³
Barcol Hardness	70-85
Abrasion resistance (Taber Test)	30-40
Compression resistance	15.8 kg/mm ²
Impact resistance	0.6 kJ/m ²
Flexural modulus (50° C)	112-140 kg/ mm ²
Specific heat	0.55 cal/g° C

The preparation of packaging the SMS sensor probe is shown in Figure 3.5- Figure 3.8. The CR-39 plate which its width of 4cm, was drawn a straight line marking the position of the SMS placement. This process is crucial as to ensure the SMS is placed in a straight manner on the plastic plate. 3M tape was used to secure both end of the SMS to fix the MMF section coincide with that of the plastic plate as presented in Figure 3.5.

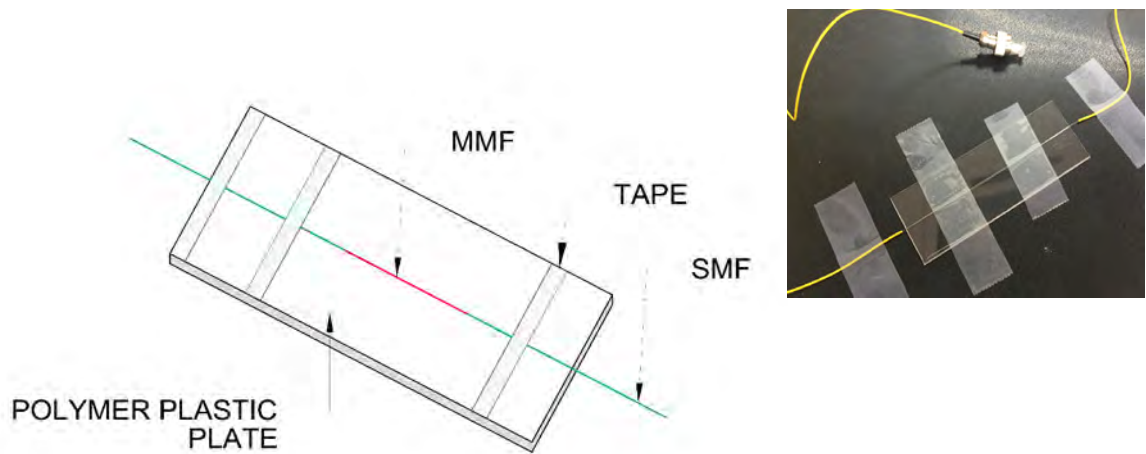


Figure 3.5: Placement of fiber on the polymer plastic plate

In Figure 3.6, a small amount of epoxy was applied evenly on end of the fiber. The drying process was taking approximately 30 minutes. Then, the SMS fiber was pulled towards vertical axis with appropriate force to ensure the SMS is positioned in straight manner. At this time, another end of the fiber was adhered with epoxy. Extra precautions measure is necessary to avoid SMS fiber loosen during the drying process as it might not firmly fixed at the position. The second drying process should take approximately 30 minutes. Subsequently, another identical CR-39 plate was spread by a thin epoxy and the plate was pressed onto the SMS- adhered plate as depicted in Figure 3.7. The packaged SMS as seen in Figure 3.8 was left to dry for 8 hours for maximum adhesion.

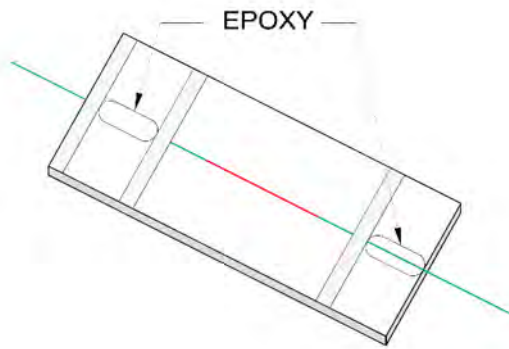


Figure 3.6: Adhesive fixture of fiber on polymer plastic plate

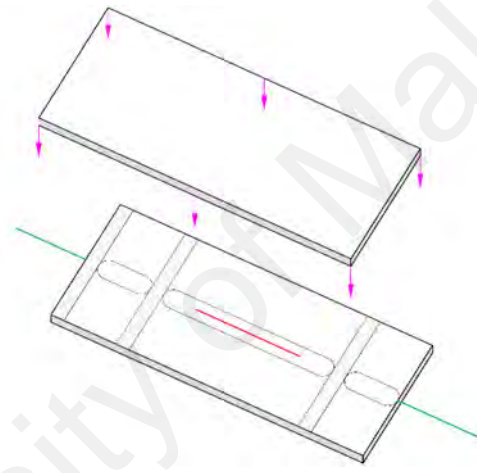


Figure 3.7: Sandwiching fiber with two plastic polymer plates

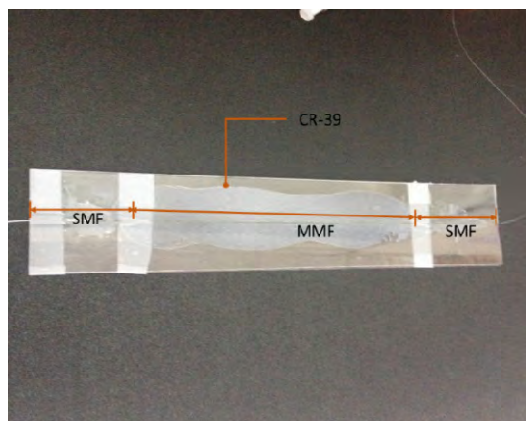


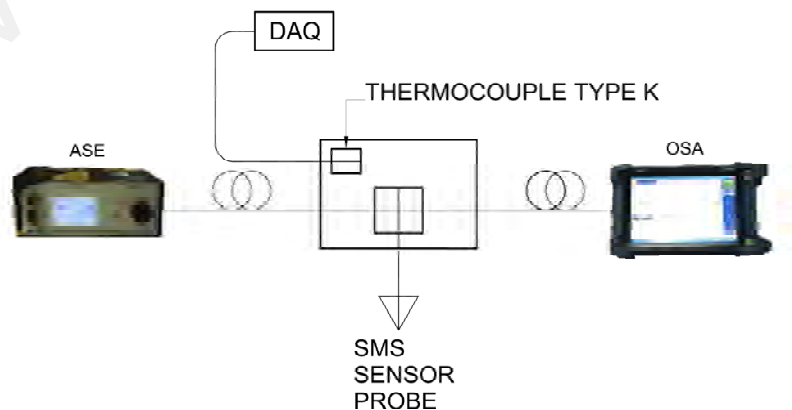
Figure 3.8: Packaging of SMS structure

3.1.4 Characterization of SMS sensor probe

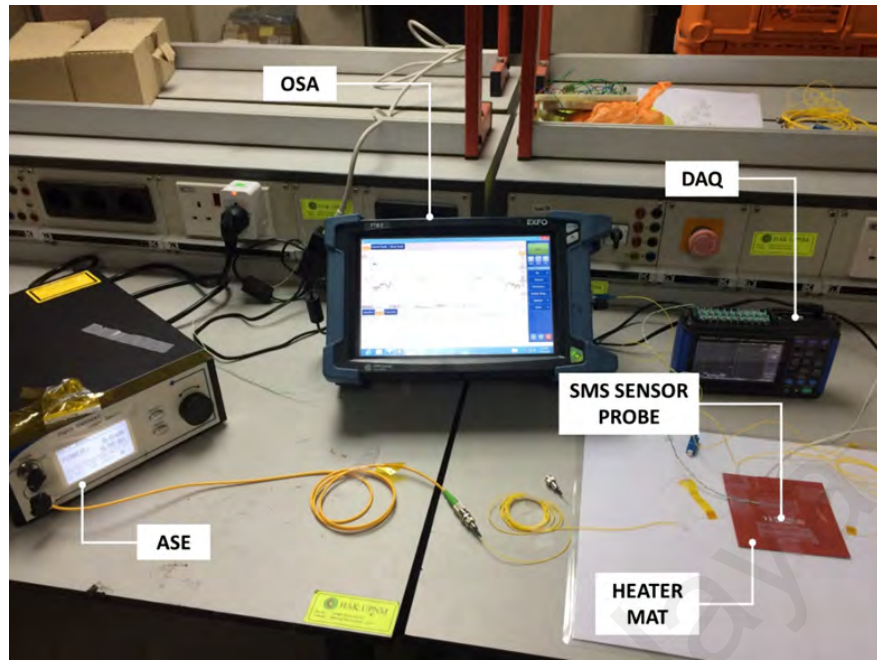
3.1.4.1 Investigation on Temperature Sensitivity of the SMS structure

Temperature reliance investigations were also performed on the spectral features of the SMS probe. The temperature reliance may influence the practical implementation, so the impacts of temperature on the features of the SMS device need to be investigated.

The experimental setup to test temperature response of the SMS structure is depicted in Figure 3.9. A rectangular heater mat, which made of Permacel P5004, glass cloth supported by silicon rubber with thickness of 0.7mm was used to provide temperature measurement on the SMS structure. The heater mat was powered by dc voltage up to 12v. The thermocouple type K was fixed on the surface of the heater mat using thermal adhesive tape. The thermocouple was connected to the data logger to read and store the temperature values. SMS sensor probe was secured on the heater mat as shown in Figure 3.10 with ASE light source at C-band wavelength as supply and the output of SMS sensor probe was connected to OSA to observe its output power spectrum. The measurement of thermocouple type K and the SMS sensor were simultaneously recorded for comparison.



(a)



(b)

Figure 3.9: (a) Schematic diagram (b) photo image of experimental setup for temperature measurement of SMS structure

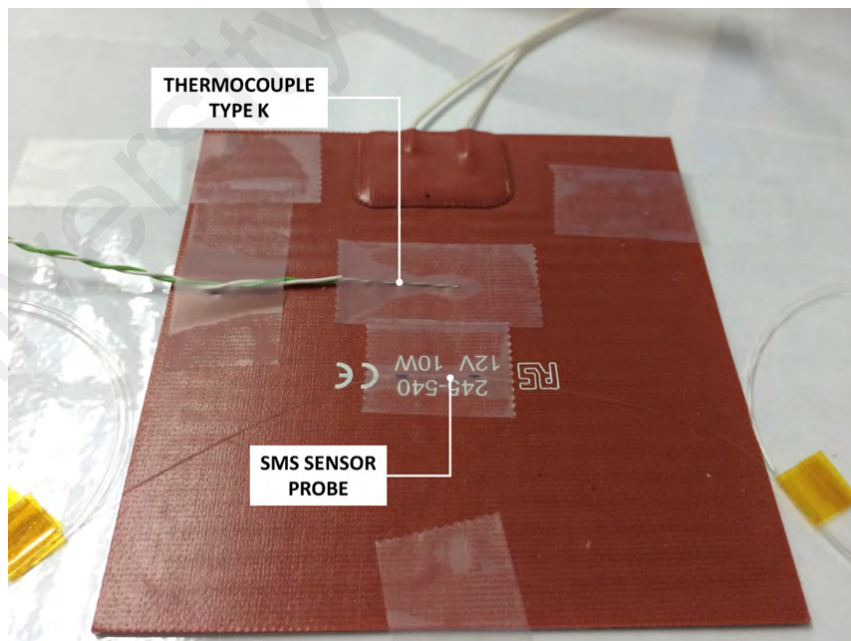


Figure 3.10: Placement of thermocouple and SMS structure on the heater mat

Experimental temperature measurement was conducted on unpackaged and packaged SMS with approximately 10 cm of MMF with temperature sweeping from 25°C to 55°C. The output power spectrum for each structure was observed during the increasing of temperature. The MMF length of 10 cm was used to develop the SMS sensor to measure the temperature measurement of SMS. The spectrum of 10cm consists visible peaks and dips as the interval of the various peaks of the output power is influenced by the MMF length. Figure 3.11 illustrates the corresponding power spectrums for both unpackaged and packaged SMS structures. The transmission spectra of the unpackaged SMS exhibits the minimum interference of two modes at dominant wavelength of 1550 nm. On the other hand, the packaged SMS structure has a maximum interference at the dominant wavelength of 1552 nm. Since the packaging material introduced external force to the SMS structure, there will be some changes in the fiber length, refractive index or core diameter, which these changes will lead to the changes in output spectral of the packaged SMS structure.

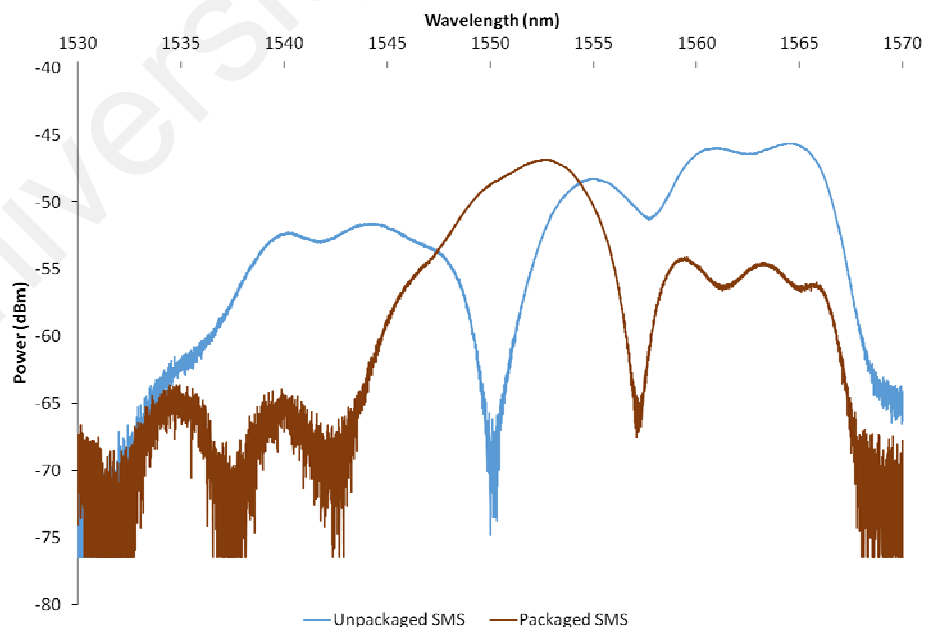


Figure 3.11: Power Spectrum for unpackaged and packaged SMS structures

The inset of Figure 3.12 shows the transmission spectra of the unpackaged SMS. It is noticed that the peaks and dips of the transmission spectra are not shifted from the corresponding wavelength with increasing temperature. This indicates that the output spectra of the SMS structure is not sensitive to the temperature variation. Figure 3.12 shows the relationship of the temperature changes and its corresponding peak wavelength. Thus, it is further interpreted that the unpackaged SMS has good temperature stability.

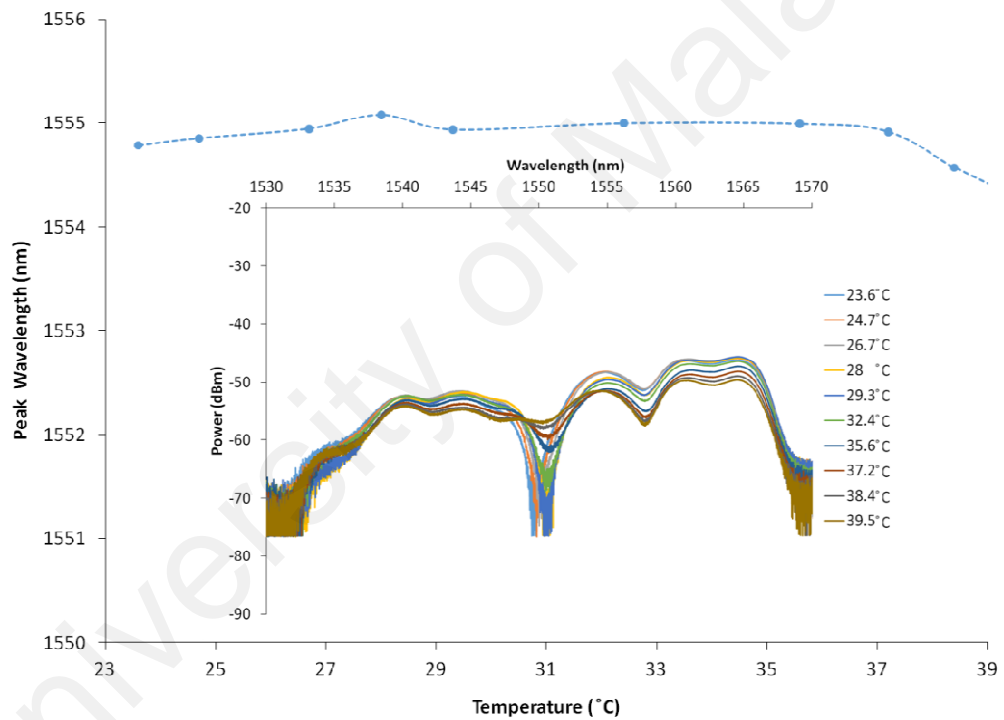


Figure 3.12: Peak wavelength response as a function of temperature and spectral response (inset) of unpackaged SMS

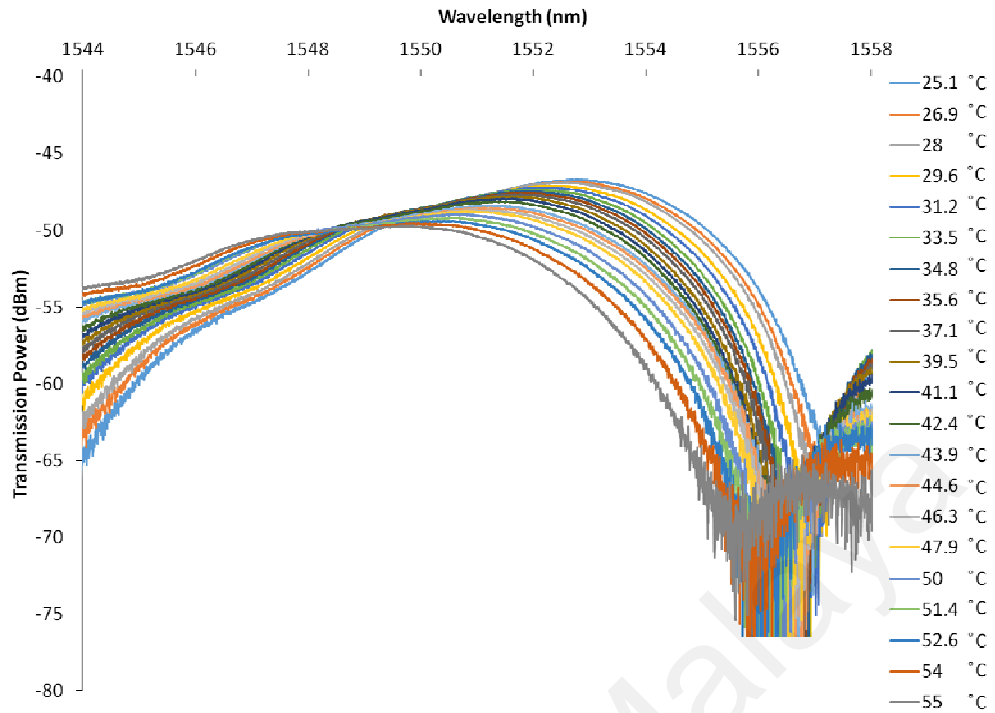


Figure 3.13: Spectral response of packaged SMS as a function of temperature

In comparison, Figure 3.13 shows the transmission spectra of the packaged SMS. It is observed that the peak wavelength of the packaged SMS in at different temperatures shifted towards shorter wavelength. When the packaged SMS experiences temperature variation, the structure will experience thermal stress which is contributed by the thermal expansion coefficient of the sensing fiber and also the packaging material. Thus, the wavelength of the spectral response will be shifted corresponding to the temperature changes.

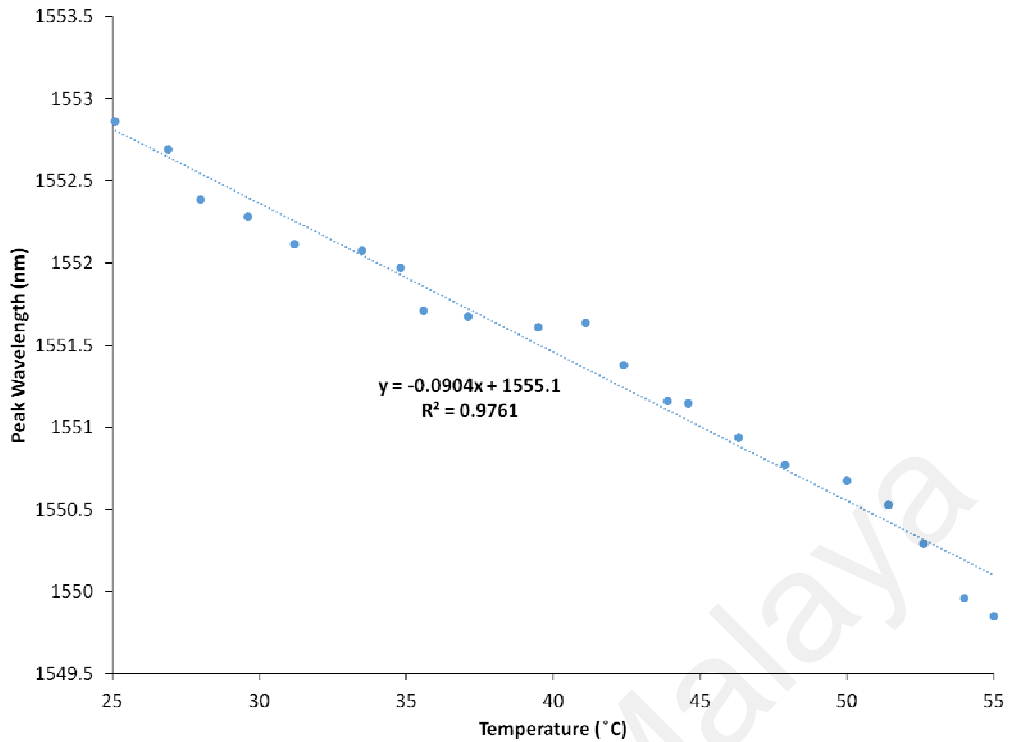


Figure 3.14: Peak wavelength response of packaged SMS as a function of temperature

Figure 3.14 shows the relationship of the temperature and wavelength shift of the output spectrum of the package. The packaged SMS exhibits respond to temperature fluctuation with sensitivity measurement of 0.0904 nm/°C. It is agreeable to the work by Q. Wu et al. (2009) that their SMS structure achieved sensitivity up to 10 pm/°C. The SMS structure with chemical coating or etching will obtains high sensitivity in measurement to temperature variation (Y. Zhang et al., 2014; S. Silva et al., 2012). Thus, based on the temperature measurement of both packaged and unpackaged SMS structures in this work, these structures are reliable for strain measurement under normal ambient environment as the performances of SMS will be not influenced by small temperature disturbances.

3.1.4.2 Loading analysis of the SMS structure

A loading fixture as shown in Figure 3.15, was used to experimentally investigate the loading effect on the packaged SMS. The SMS was placed with one end at fixed position securing by the clamp, while the load was placed at the other end of the SMS. Broadband light from ASE was fed into the packaged SMS and the output spectrum was observed by an OSA. Figure 3.16 is the photo image of load analysis experimental setup for packaged SMS structure at the laboratory.

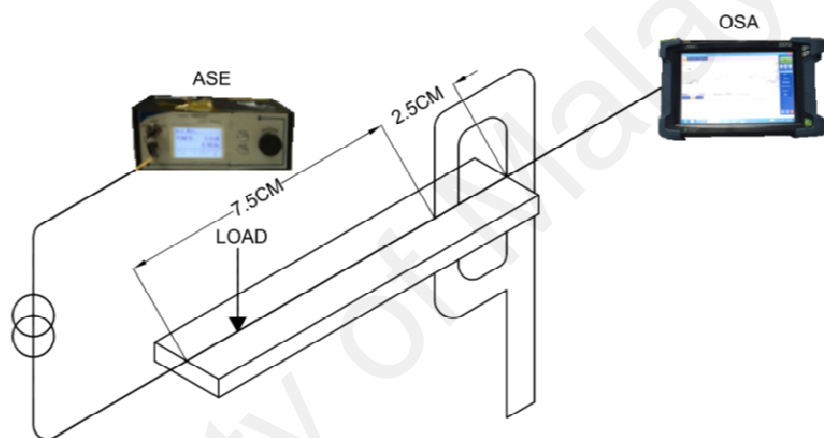


Figure 3.15: Schematic diagram load analysis experimental setup for packaged SMS structure.

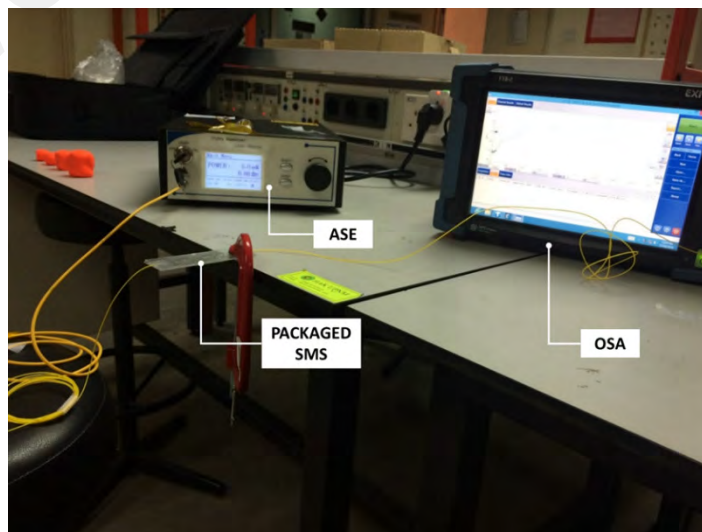


Figure 3.16: Photo image of load analysis experimental setup for packaged SMS structure.

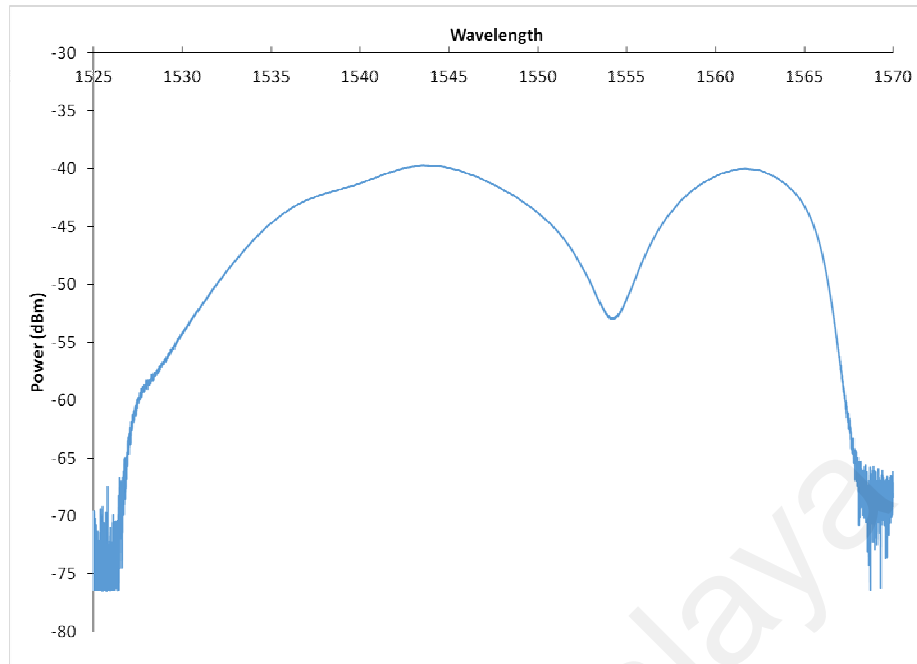


Figure 3.17: Transmission spectra of the packaged SMS for unloading condition

The measurement of the output spectrum was initially taken for unloaded condition, which is shown in Figure 3.17. The spectrum in is the resultant of the multimode interference along the SMS structure. It is noted that there are two peaks corresponding to 1545 nm and 1562 nm respectively.

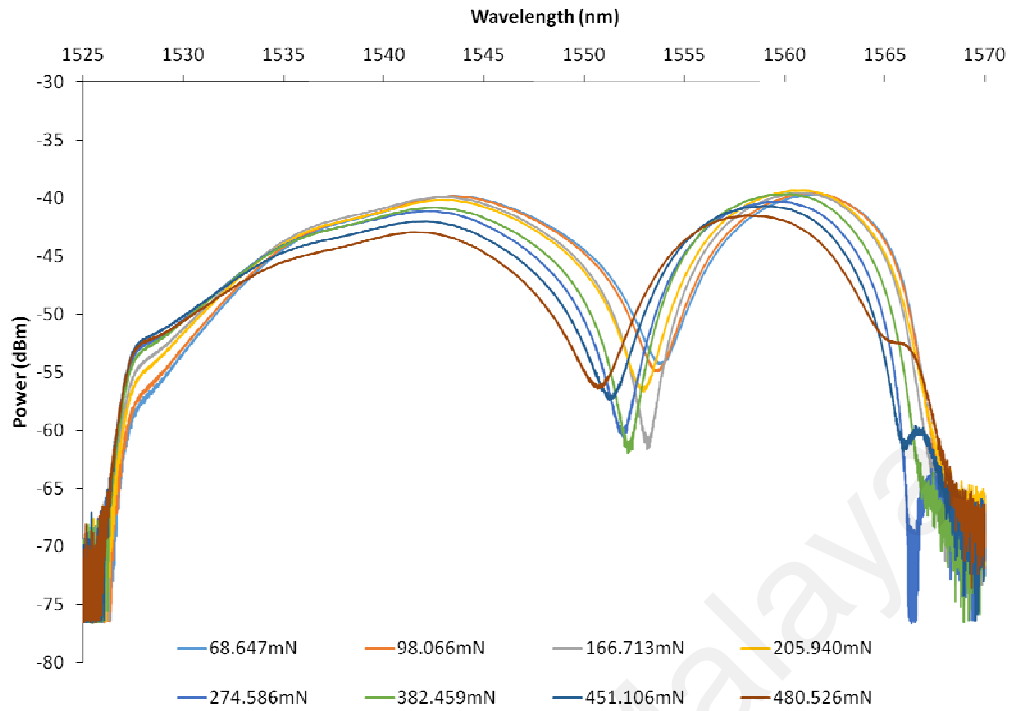


Figure 3.18: Spectral response from the packaged SMS at different load values up to 480.526mN

The load on the SMS structure was then lifted to 480.526 mN in small increments. The measured spectral responses due to the load changes is shown in Figure 3.18. As observed from the graph, the dip wavelength changes as the load increases. The spectrum wavelength changes to smaller wavelength as the load rises. It can be implied that the bending MMF in the SMS structure creates asymmetric refractive index spread and influences the resulting transmission pattern of the SMS structure.

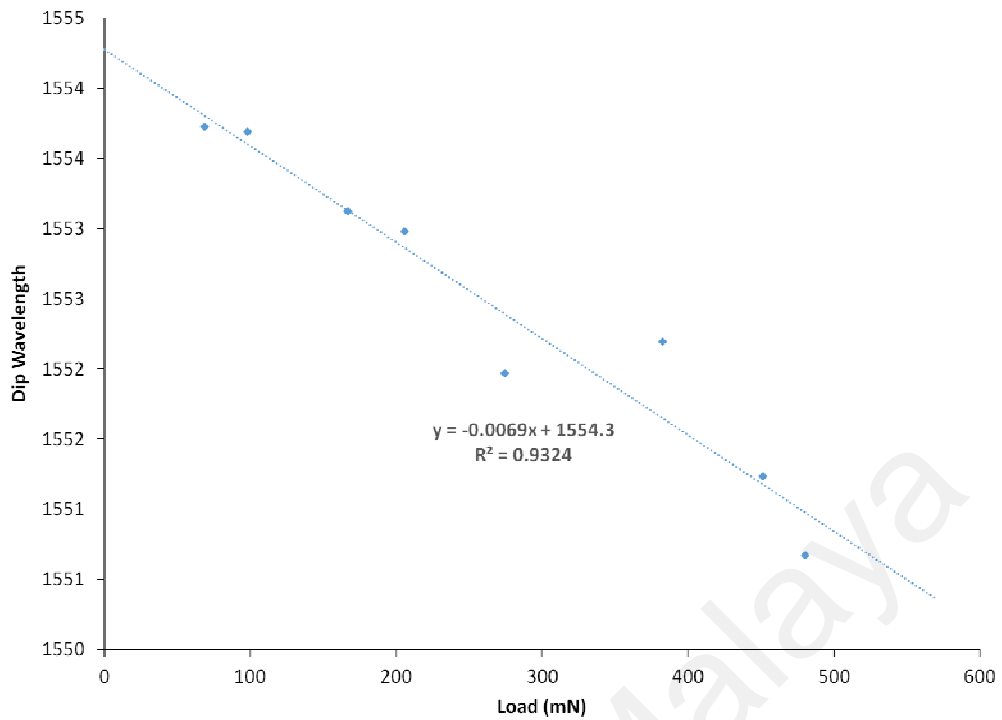


Figure 3.19: Central dip wavelength against the amount of load

Figure 3.19 illustrates the relationship between the interference wavelength dip and the different load with measuring sensitivity of 0.0069 nm / mN. The packaged SMS structure behaves elastically for small strains and returns to the original position after being bent. However, higher quantity of strain larger than 451.106mN is avoided to be applied on the SMS as this quantity of strain may exceeded the elastic limit of the packaged SMS and cause permanent deformation and fracture.

3.2 Fabrication & Characterizations of MSM sensor probe

3.2.1 Sensing principle of MSM structure

The MSM sensor probe as shown in Figure 3.20, is constructed by fusion splicing both terminals of SMF segment with two short MMF segments. The length of the two identical MMF segments is L_1 , meanwhile the length of the sensing SMF is L_2 .

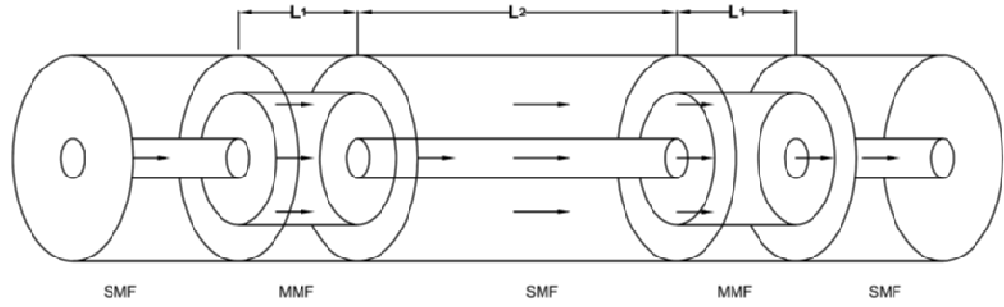


Figure 3.20: Schematic diagram of MSM structure

When light is transmitted to the first MMF segment from the SMF, a higher order eigenmodes will be excited along the first MMF. The field profile in the first MMF is written as below:

$$\Psi(y, L_1) = \sum_{m=1}^M c_m \psi_m(y) \exp(j\beta_m L_1) \quad (3.13)$$

Where $\psi_m(y)$ denotes the m^{th} order of the eigenmodes of the first MMF, c_m is the excitation coefficient and β_m is the propagation constant of the MMF. At the junction of the first MMF and the sensing SMF, a portion of light propagating along the core MMF will be leaking to the SMF cladding due to the mismatch core size in between the SMF and MMF. Thus, the excitation coefficient of n^{th} mode of the SMF is derived as below:

$$c_n = \frac{\int \Psi(y, L_1) \psi_n(y) dy}{\sqrt{\int \psi_n^2(y) dy}} \quad (3.14)$$

After propagating a distance of L_2 in the sensing SMF, the field profile of the n^{th} mode can be obtained as (3.15) with given that β_n is the propagation constant of the sensing SMF.

$$\Psi(y, L_2) = \sum_{n=1}^N c_n \psi_n(y) \exp(j\beta_n L_2) \quad (3.15)$$

Similarly, when light is relaunched at the junction of the sensing SMF and the second MMF, some cladding modes of SMF couples with the guided mode in the MMF. Therefore, MMI occurs in between the fundamental mode and the higher order cladding modes of the sensing SMF along the second MMF segment. The phase difference between the fundamental mode and the higher order cladding modes of the sensing SMF can be expressed as (3.16)

$$\phi_{mmf} = \frac{2\pi\Delta n_{eff}L_2}{\lambda} \quad (3.16)$$

Where Δn_{eff} is the effective refractive index difference in between the core mode and the nth cladding mode. Therefore, the intensity of the transmission spectrum of the MSM structure can be expressed as (3.17).

$$I = I_c + I_n + 2\sqrt{I_c I_n} \cos \phi_{mmf} \quad (3.17)$$

Where I_c is the intensity of the core mode, I_n is the intensity of the nth cladding mode of the sensing SMF. The intensity of the light transmission of the MSM structure reaches its critical value when the phase difference between the fundamental mode and the higher order cladding modes of the sensing SMF equals to the multiples of 2π . Thus, the wavelength at dominant interference, λ_d is determined as below:

$$\lambda_d = \frac{2\Delta n_{eff}L_2}{2N+1} \quad (3.18)$$

Where N is an integer representing the interferential order. When the MSM structure is applied with external perturbations such as strain, the characteristics of the MSM transmission spectrum such as the resonant wavelength as expressed in (3.19) will change due to the changes in the fiber dimensions and refractive index (Z. Xu et al., 2013).

$$\frac{\Delta\lambda_d}{\lambda} = \frac{2\Delta n_{eff}L_2}{2N+1} \cdot \left(\frac{1}{n_{eff}} \Delta n_{eff} + \frac{2}{a} \Delta a + \frac{1}{L} \Delta L \right) \quad (3.19)$$

Where Δn_{eff} is the variation of the effective refractive index difference of the core mode and nth order cladding mode in the SMF, Δa is the radius changes of the SMF and ΔL is the length changes of the SMF. The interference between the core mode and cladding modes is significantly influenced by the length and the effective refractive index difference of the sensing SMF (Yin et al., 2016).

3.2.2 Fabrication of MSM sensor probe

Two MSM structures are constructed with different configuration parameters as tabulated in Table 3.2. The MSM structures consist of 5.0 cm long MMF, 4.0 cm long and 2.5 cm long for SMF respectively. The chosen length of the MMF segment is compact and sufficient to provide fewer cladding modes to be strongly coupled with the core mode in the sensing SMF.

Table 3.2: Physical Dimension of MSM structures

	MSM 1	MSM 2
Length of first MMF segment (cm)	5.0	5.0
Length of SMF segment (cm)	4.0	2.5
Length of second MMF segment (cm)	5.0	5.0

The length of the sensing SMF in the MSM structure is greatly influencing the free spectrum range between two interference modes as previously expressed in equation (3.18). Two distinct length of the sensing SMF are used to construct the MSM structure; 4 cm and 2.5 cm respectively. The transmission spectrum of these MSM structures at ambient temperature are shown in Figure 3.21. It can be seen clearly that the interference spectrum of the 4 cm SMF has more multiple peaks and dips as compared

to the spectrum of 2.5 cm SMF. With the sufficient length of the sensing SMF, the interference of the core mode and cladding modes can strongly modulate the interference pattern of the MSM structure. However, the interference pattern of the 2.5 cm SMF is having distinct values of peaks and dips, which make the MSM with 2.5 cm SMF a compact feature of a sensor.

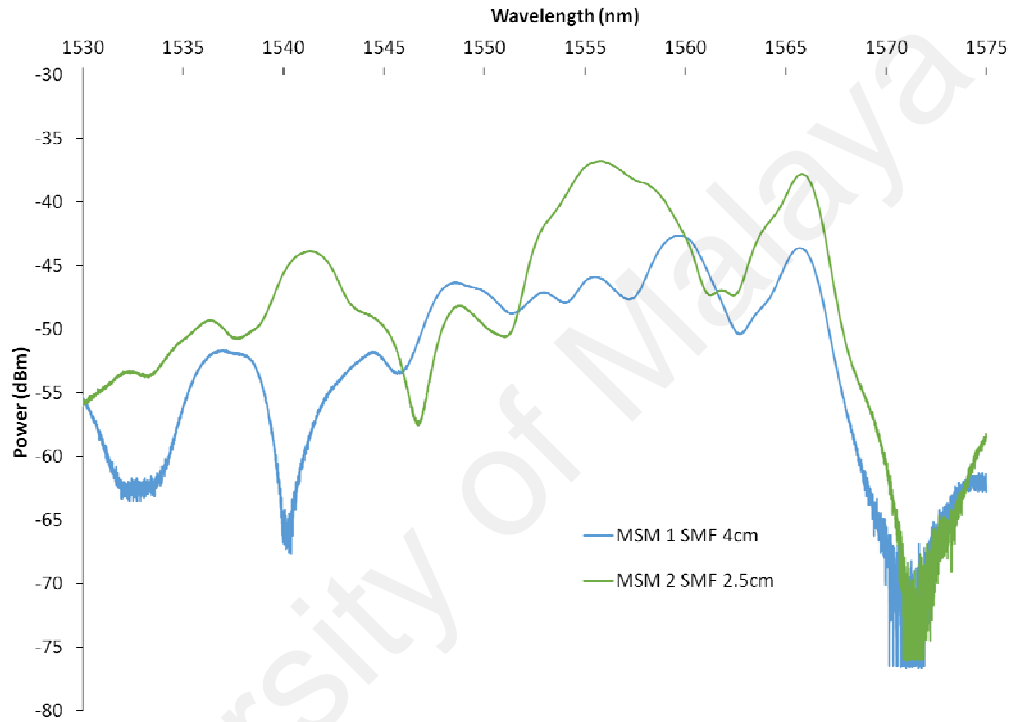


Figure 3.21: Spectral response of MSM uncoated SMF length of 4.0 cm and 2.5 cm

3.2.3 Characterization of MSM sensor probe

The temperature response of MSM structure was also experimentally demonstrated. Similar experimental setup in Figure 3.9(a) was used to investigate the temperature response of the structure. The MSM structure was secured on the heater mat and the pigtail was connected to ASE C-band source. The spectrum of transmission was obtained from the optical spectrum analyzer. The MSM structure temperature variations were recorded using thermocouple type K.

The observation of the interference dip was made around wavelength of 1550 nm for temperature analysis of the structure. As shown in Figure 3.22, when the temperature increases, the power spectrum shifts towards smaller wavelengths. The results obtained indicate the achievement of stable temperature at a sensitivity of 9.7 pm/ ° C within 25-38 ° C temperature range. However, the temperature sensitivity of the MSM fiber structure is 0.1896 nm/ ° C when the temperature rises above 38 ° C. When there is a temperature perturbation on the SMF segment, the phase in between the core and cladding modes changed and thus, the spectrum shifted too. It can therefore be inferred that the MSM structure provides greater sensitivity in temperature measurement than the SMS structure because there are significant differences in the effective refractive index of the structure's cladding and core modes (Silva et al., 2012).

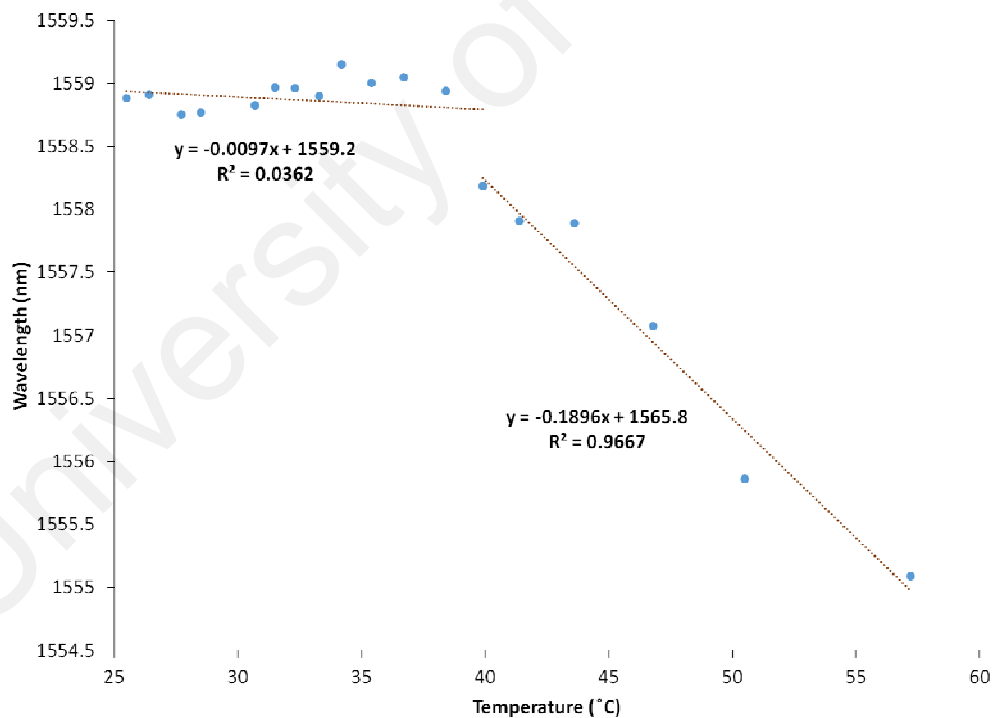


Figure 3.22: Peak wavelength of the spectral response of MSM as a function of temperature

3.3 Summary

The fabrication of the SMS structure is far simpler than the fabrication of the MSM structure. MSM structure is more challenging to construct as it is built by cascaded splicing to replicate two SMS systems. In addition, the MSM structure is more sensitive to temperature changes than the SMS structure. Based on the results obtained in the load analysis, the bending of the packaged SMS structure has an enormous impact on the structure's transmission spectral response. It is observed that the FBG sensor is insensitive to the load supplied to it.

University of Malaya

CHAPTER 4: WATER WAVE GAUGE BASED ON SINGLEMODE- MULTIMODE-SINGLEMODE FIBER STRUCTURE

4.1 Introduction

Waves are primary consideration in the design of coastal structures as waves lead longshore sediment transport and create currents. Waves generally produced by wind moving across the ocean surface. The fluctuation on the water surface leads the water to rise above the equilibrium level while the gravity force forces the water to reach below its equilibrium level. These forces lead in wave propagation in oscillations where energy is transferred in a circular orbital motion. Due to the complexity of the coastal system, physical modeling is usually preferred for solving coastal engineering problems. This method facilitates better prediction in controlled environments.

Physical modeling is a miniature system conducted in laboratory settings that offers advantages over both field studies and numerical modeling approach as observed by Hughes (Hughes, 1993). It includes equations that are used to govern the process without the need to simplify numerical models. Furthermore, small-size data are sufficient to be used in physical models compared to field studies. The researcher controls the conditions being studied and may reproduce a variety of conditions, even those that may be important although they rarely occur in the field. Finally, researchers are able to observe the system as the experiment develops in the physical model, which gives them a better understanding of behavior and processes.

Physical modeling, however, has the notable drawback that its scale is smaller compared to the field study. For example, the effects of the wave's viscous forces cannot be performed in the laboratory flume. In addition, the laboratory environment also causes effects, and it is unlikely that the exact conditions in nature can be replicated

in the laboratory. An example is the use of unidirectional waves instead of multidirectional waves occurring in nature.

A laboratory flume with a wave maker is often used to make physical water wave models that include hydrodynamic forces, motion analysis, and wave patterns (Sorensen, 1997; Goseberg et al., 2013). The flume typically has a long and narrow enclosure with a wavemaker at one end. The wavemaker is essential for the reproduction of natural wave conditions in the laboratory flume. In early research, a simple mechanical wave paddle was used in the laboratory to generate waves that moved sinusoidally at a certain amplitude and period.

Subsequently, the generation of laboratory waves evolved from a simple paddle mechanism to the use of complex theories of wave generation to predict waves generated from various paddle motions. Most flumes are still using flap or piston wave makers. At relatively low water depth, piston wave makers are commonly used. The orbital particle motion is compressed into an elliptical shape when the water is shallow in relation to the wavelength, thus creating noticeable horizontal movement on the flume floor. Many previous studies used piston wave generation (Malek-Mohammadi, 2010; N.-J. Wu, Tsay, & Chen, 2014). Flap wave generators (Elangovan., 2008) are used to generate water waves in modeling the sea structure in deep water. Waves are produced by decay of the orbital particle motion at depth and the lack of motion at the bottom. (Hughes, 1993).

Waves generated in the laboratory flume are usually detected by means of a resistance wave gauge consisting of an electrical circuit with a pair of wires partially submerged in the water (Hughes, 1993). The resistance of the submerged wire will vary according to the different water levels. Despite the good linear response of the resistance wave gauge, it has to be frequently calibrated. The calibration process is

usually time consuming as it is necessary to ensure minimum fluctuation of the water level, which can affect the gauge calibration quality. Furthermore, each resistance wave gauge requires an electronic circuit to compensate the connecting cable's parasitic impedance to obtain linear output response. This packaged SMS structure was proposed as a water gauge showing similar good linear response. The SMS sensor is beneficial as it can resolve the disadvantages of standard wave gauges with added attributes of its simple design, ease of fabrication and resistant to interference from electromagnetic fields.

As stated previously in Chapter 2, the SMS fiber design has achieved notoriety among researchers for application in a displacement detector (A. Mehta, 2003), refractive index sensor (P. Wang et al., 2011), structural health monitoring (Masnan et al., 2016), and load sensor (Rionda Kuntaraco, 2014) due to its multimodal interference property. The sensor is packed with CR-39 plastic polymer sheets so that it can detect water wave based on a linear, uniform fiber bending mechanism that will alter the trend of light interference and output energy. To the best of my knowledge, this study is the first attempt to use the SMS interferometer to detect water waves.

4.2 Water Gauge Experimental setup

The SMS sensor is constructed using a 9.6 cm-long multimode fiber (MMF) with a step index profile and a core size of 105 microns. As the SMS structure will be packaged using CR-39 plastic polymer plates and is hung 1 cm above the static water level of the water flume, the sufficient length of the MMF will provide the sensor the flexibility and strength to gauge water wave. When water wave hits the packaged SMS, it will experience bending due to the movement of the water wave in the flume. The MMF length used is sufficient to provide effective bending that causes the effective refractive index in the MMF section to change. A portion of light will escape from the

core of the fiber to the cladding layer and causes energy radiation in the structure. The amount of change is proportional to the amount of bending that occurs in the SMS. The smaller the MMF bending radius, the greater the power change. When no wave force is applied to the packaged SMS, the device returns to its original state because the CR-39 plates exhibit elasticity as previously described in Chapter 3.

The SMS is sandwiched between two CR-39 plastic polymer plates that are 0.05 cm thick, 4 cm wide, and 17.4 cm long. The CR-39 plastic polymer is used as the packaging material for the SMS sensor because it is rather thin, highly flexible and elastic. The characteristic of the packaged SMS structure is further explained in previous chapter. Waterproof epoxy is used to attach the plates to the SMS fiber.

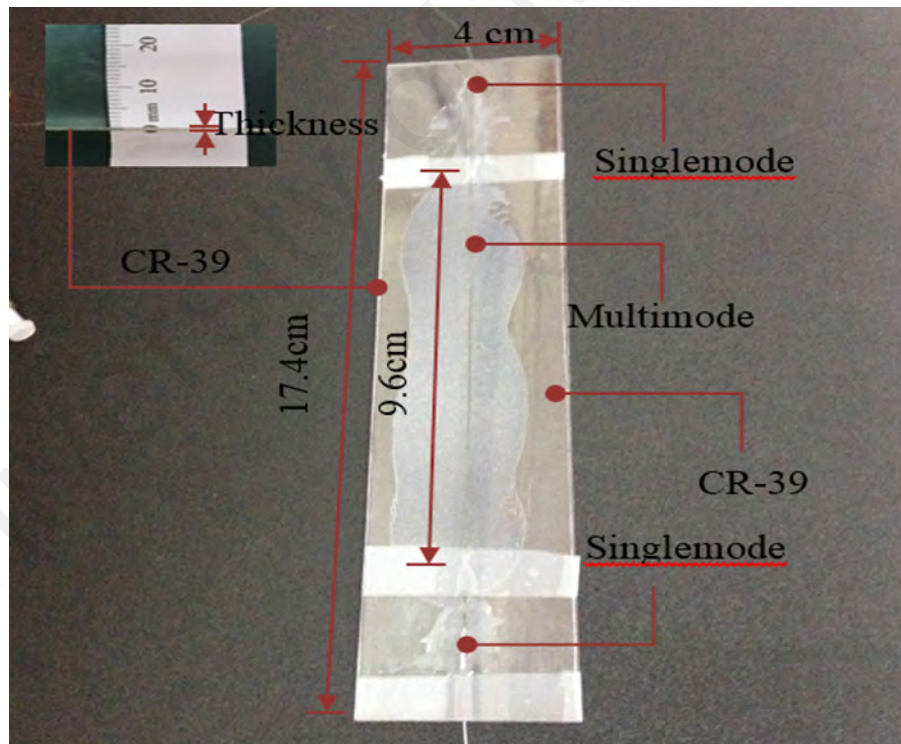


Figure 4.1: SMS is sandwiched between CR-39 polymer plates

Figure 4.2 shows the SMS wave gauge experimental setup using the C4MKII-5.0M Multi-Purpose Teaching Flume and the C4-67 wave generator mounted on top of the flow channel inlet tank. The flume consists of metal frames and clear acrylic sides in the working section, so the flow is visible. The working section of the flume is 76 mm wide, 250 mm deep, and 5 m long. The C4-67 wave generator is used to generate water waves at various speeds. It consists of a vertical paddle that is moved backward and forward to produce water waves in the flow channel. The drive arrangement consists of a combined motor and gearbox with an eccentric crank wheel at different radii to change the stroke of the paddle.

The speed of the drive motor can be adjusted via the hydraulic motor control to change the frequency of waves via the speed controller. A wave absorber is placed at the opposite end of the flow channel to reduce the reflections of the wave by absorbing its energy. The flume is filled with clear water at a depth of 11.4 cm. The packaged SMS is hung 1 cm above the static water level and securely held between two metal clamps that are attached on top of the flume at a horizontal distance of 1.6 m from the back of the flume, as shown in Figure 4.2.

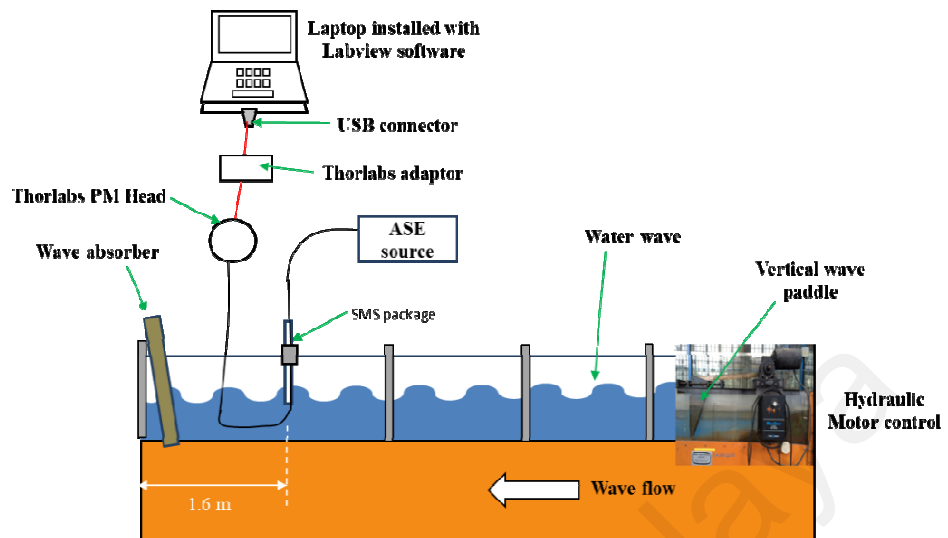


Figure 4.2: SMS wave gauge experimental setup and photo image of the wave maker flume (C4MKII-5.0M Multi-Purpose Teaching Flume mounted with C4-67 wave generator)

An amplified spontaneous emission source based on erbium-doped fiber gain medium is used to provide a broadband light source at C-band. A Thorlabs power meter (PM100USB) is used to measure the average power of the output transmitted by the SMS package. The power meter is connected to a laptop computer via power meter adapter and a USB connection. The PM100USB is remotely operated using utility software with setting of the operating wavelength at 1550nm. The power data are measured over a time series at a sampling rate of 8.2 Hz and logged in the laptop

computer. The power time series are measured at different motor speeds of 80%, 85%, 90%, 95%, and 100% for durations of 60 seconds at each speed.

When the water wave hits the packaged SMS, the structure experiences external force that impact to bending with certain curvature radius. As the wave celerity changes with the variation of motor speed, the SMS structure bends in an almost regular periodic manner with curvature radius changes. The amount of change is proportional to the amount of bending that occurs in the SMS structure. The smaller the MMF bending radius, the greater the power will change. Since the wave celerity is dynamic parameter, the spectrum analysis technique is not suitable to be applied to the SMS structure. A fixed wavelength is chosen in order to observe the interference change of the SMS structure. When no wave force is applied to the packaged SMS, the device returns to its original state because the Cr-39 plates are highly elastic as previously described.

4.3 Results and discussion

The mechanism of sea waves is complex because of their varying amplitudes, intervals, and distances from one to another. Hence, surface water sea waves are usually studied using the small amplitude wave theory based on Airy's model to simplify their complexity to two-dimensional behavior. According to the theory, the wave celerity or speed of the wave is the distance travelled by a crest per unit of time. Figure 4.3 shows water wave pattern and parameters in a cross-sectional view where L , H , and d represent water wave length, wave height and static water depth respectively. The wave height is the vertical distance in between the crest and trough on the water wave. Meanwhile, the water wave length is the horizontal distance between successive crests or troughs. Based on Airy's model, the wave celerity of the intermediate water depth can be calculated using equation (4.1). However, the formula is only valid to the wave conditions in which the wave height is small compared to the length and depth of the wave.

$$C = \sqrt{\frac{gL}{2\pi} \tanh\left(2\pi \frac{d}{L}\right)} \quad \text{for } H < L \text{ and } H < d \quad (4.1)$$

where g is gravitational acceleration (m/s^2).

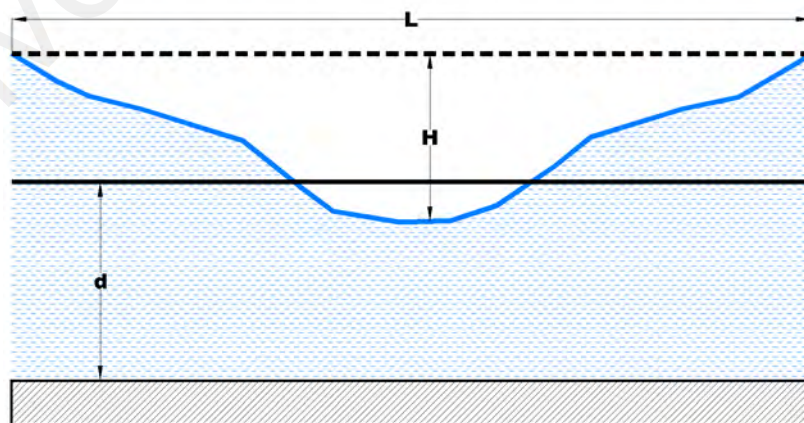


Figure 4.3: Water wave parameters

In the experiment, the water wave was generated with different motor speeds. At each motor speed, the corresponding wavelength was observed on the transparent water flume and measured using a measuring tape. The wave exhibited an almost perfect regular wave pattern and had a relative depth of $0.18 < d/L < 0.25$. Therefore, this wave was classified as transitional wave or intermediate depth wave because $0.05 < d/L < 0.5$ (Méhauté, 1976). The maximum wave height of 7.5 cm was obtained through out the experiment. Figure 4.4 shows the wave celerities and wave lengths at different motor speeds. The wave celerity values were calculated using equation (4.1) at corresponding wave lengths. It is inferred that the wave celerity increased linearly as the motor speed was increased to a slope of 0.007 (m/s)/%. In contrast, the wave length was reduced in a linear manner to a slope of 0.0087 m/%.

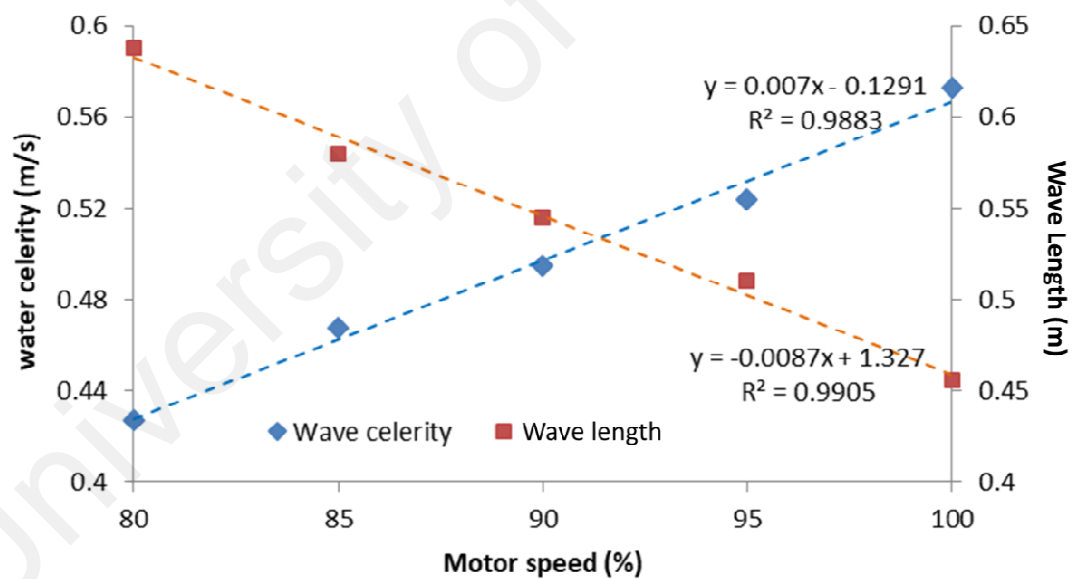
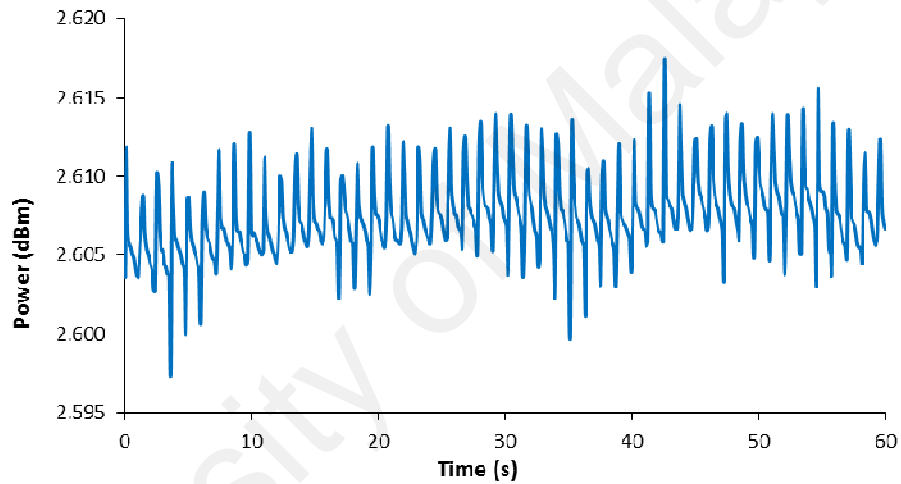
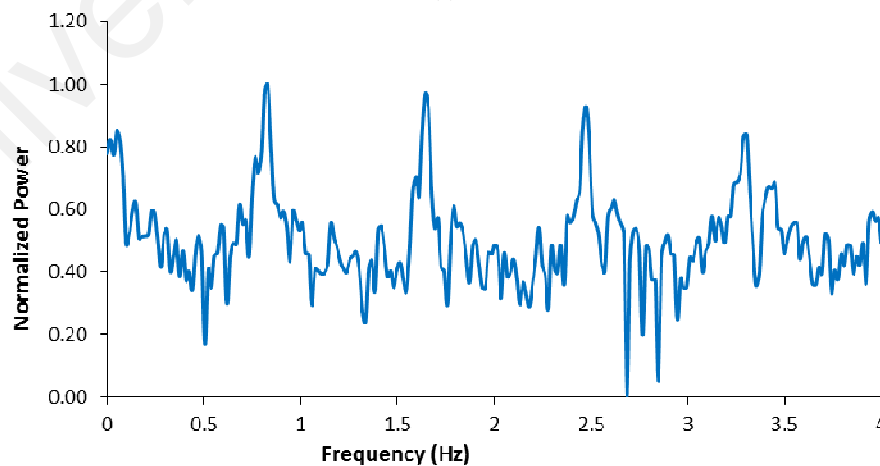


Figure 4.4: Wave celerity and wave length at different motor speeds

The averages of the power time series measurements from the output transmission of the SMS at the wave celerities of 0.43m/s, 0.47m/s, 0.49m/s, 0.52m/s, and 0.57m/s are illustrated in Figure 4.5 a) to Figure 4.9 a) respectively. Based on the observation on these figures, the power waveform fluctuated in a pulse form. The water wave is moving in orbital velocity. As the wave hits on the SMS structure, it bends in an almost regular periodic manner. The amount of bending of the structure will leads to the changes in curvature radius of the structure, and will caused the transmission power of the SMS structure to change.

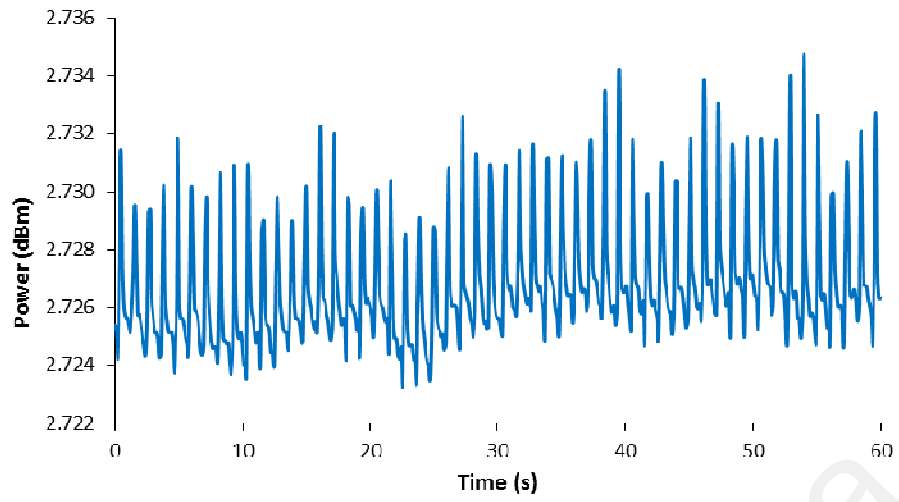


(a)

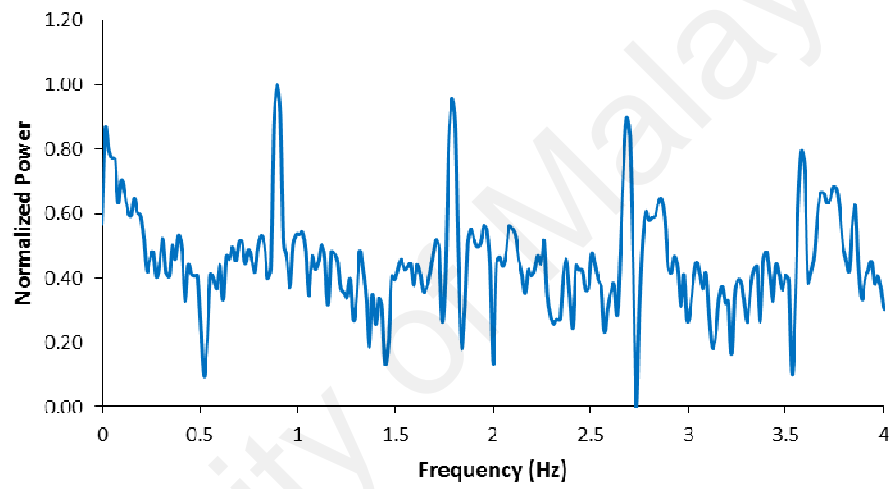


(b)

Figure 4.5: (a) Average output power time series and (b) its corresponding frequency spectrum at wave celerity of 0.43 m/s

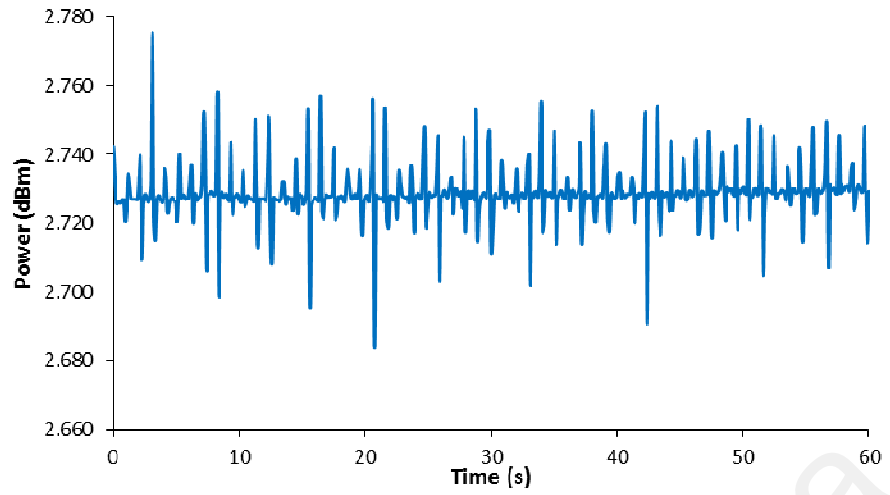


(a)

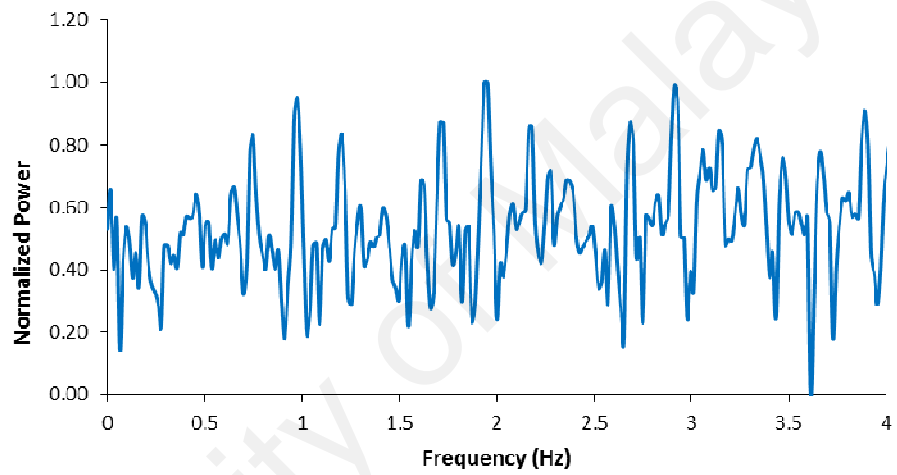


(b)

Figure 4.6: (a) Average output power time series and (b) its corresponding frequency spectrum at wave celerity of 0.47 m/s



(a)



(b)

Figure 4.7: (a) Average output power time series and (b) its corresponding frequency spectrum at wave celerity of 0.49 m/s

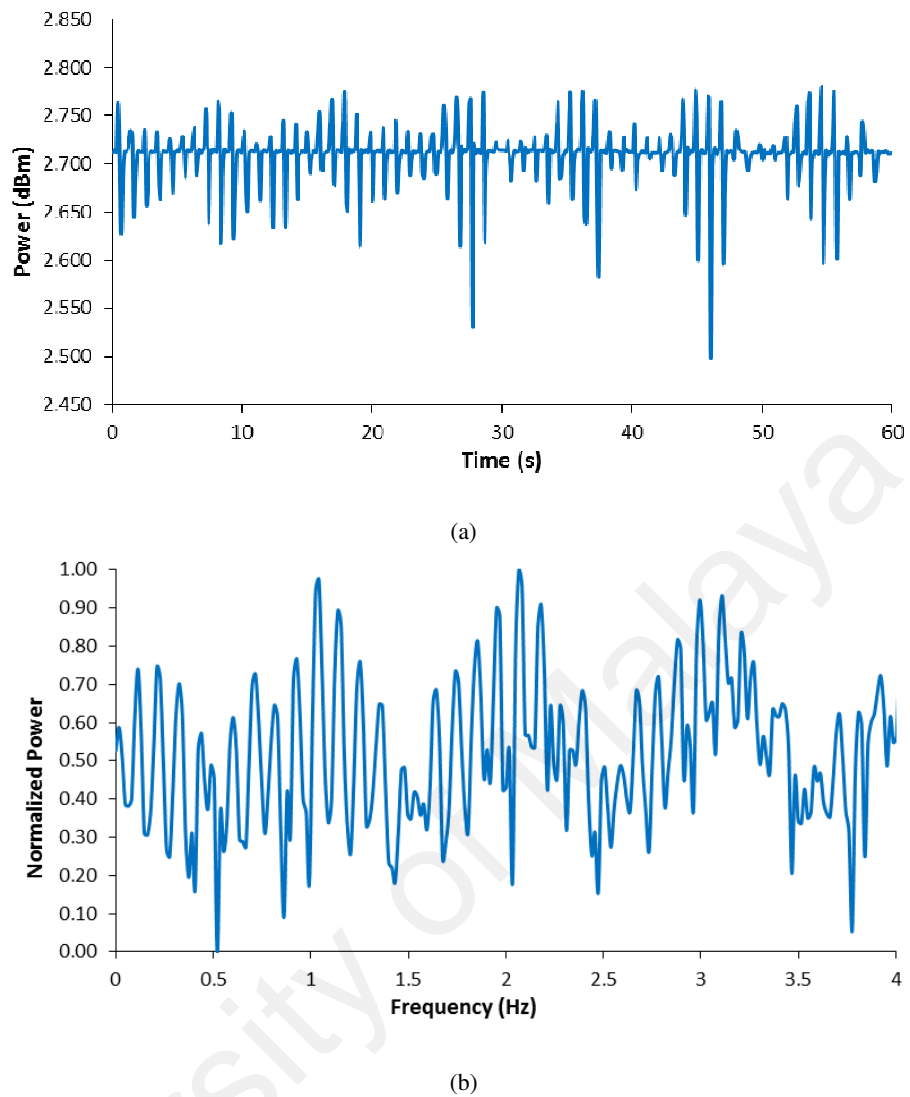
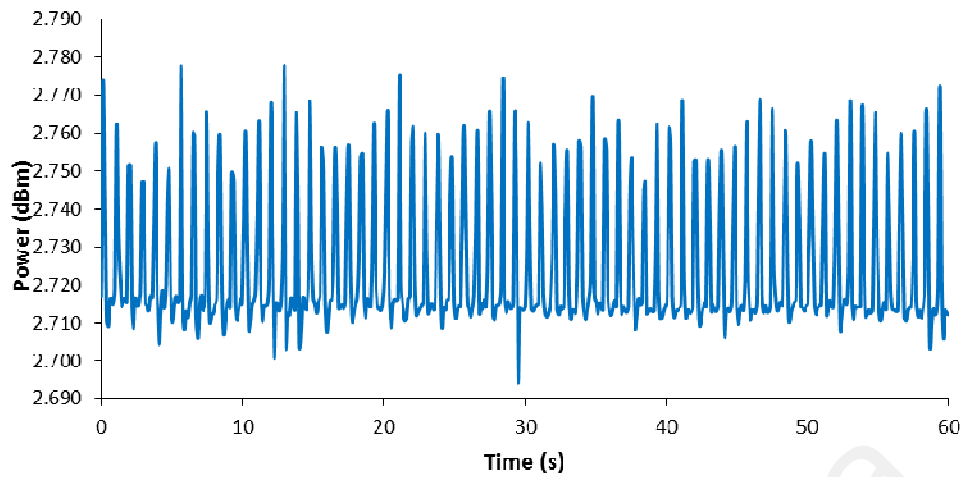
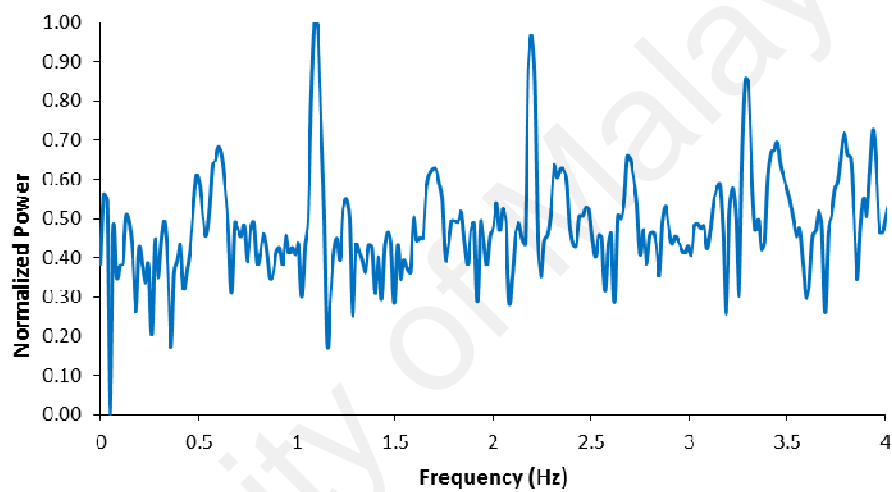


Figure 4.8: (a) Average output power time series and (b) its corresponding frequency spectrum at wave celerity of 0.52 m/s

The highest noise level was observed at wave celerities of 0.49 m/s and 0.52 m/s. At these wave celerities, the spectrum pattern was observed carefully in order to distinguish the dominant harmonics. In this research, the dominant harmonics were defined as the set of harmonics that has the highest peak power.



(a)



(b)

Figure 4.9: (a) Average output power time series and (b) its corresponding frequency spectrum at wave celerity of 0.57 m/s

Because the time series power pattern made it difficult to analyze the data, the Fast Fourier Transform (FFT) technique in the Labview software was used to convert the data into the frequency domain with sampling rate of 100 Hz and number of samples taken is 100. Figure 4.5 b) to Figure 4.9 b) show the normalized power spectra in the frequency domain corresponding to the time series measurements. The DC component of the time domain data is removed by deducting mean value from the signal. The figures show that the entire frequency spectrum exhibited dominant peak harmonics up to the third harmonic at different wave celerities. In addition, the presence of lesser

power harmonics and other low signal noises due to lesser regular wave pattern was produced by the wave paddle and the small wave reflection.

Peak fundamental harmonic frequencies of 0.83 Hz, 0.90 Hz, 0.960 Hz, 1.04 Hz, and 1.10 Hz were observed in the frequency spectrum analysis at wave celerities of 0.43m/s, 0.47m/s, 0.49m/s, 0.52m/s, and 0.57m/s, respectively. The pulse peak frequency shown in Figure 4.10 decreased linearly as the wavelength was increased at a sensitivity of 1.5613 Hz/ m.

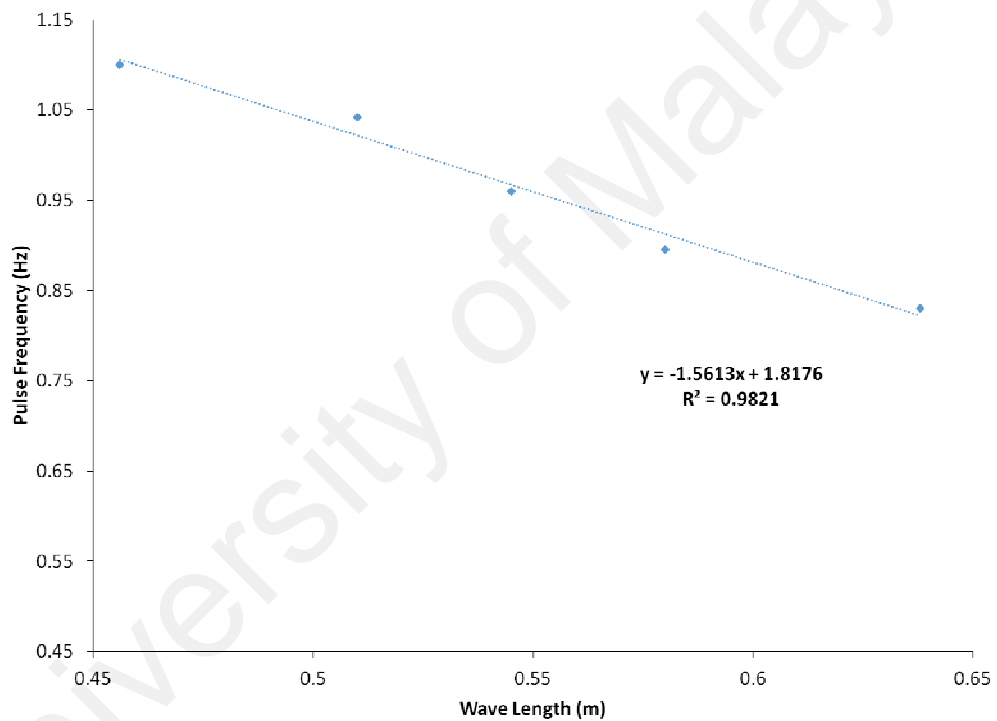


Figure 4.10: Average output power pulse frequency at different wavelength

Since the wave celerity values were calculated using equation (4.1) at corresponding wavelengths, the pulse frequency shown in Figure 4.11 exhibits a linear increasing pattern in respect to the increased wave celerity with a sensitivity of 2.0304 Hz/ (m/s). Based on these results, it can be concluded that the SMS sensor was capable to gauge wave characteristics accurately, and the noise signal could distinguished and isolated according to the weakness and strength of its power level.

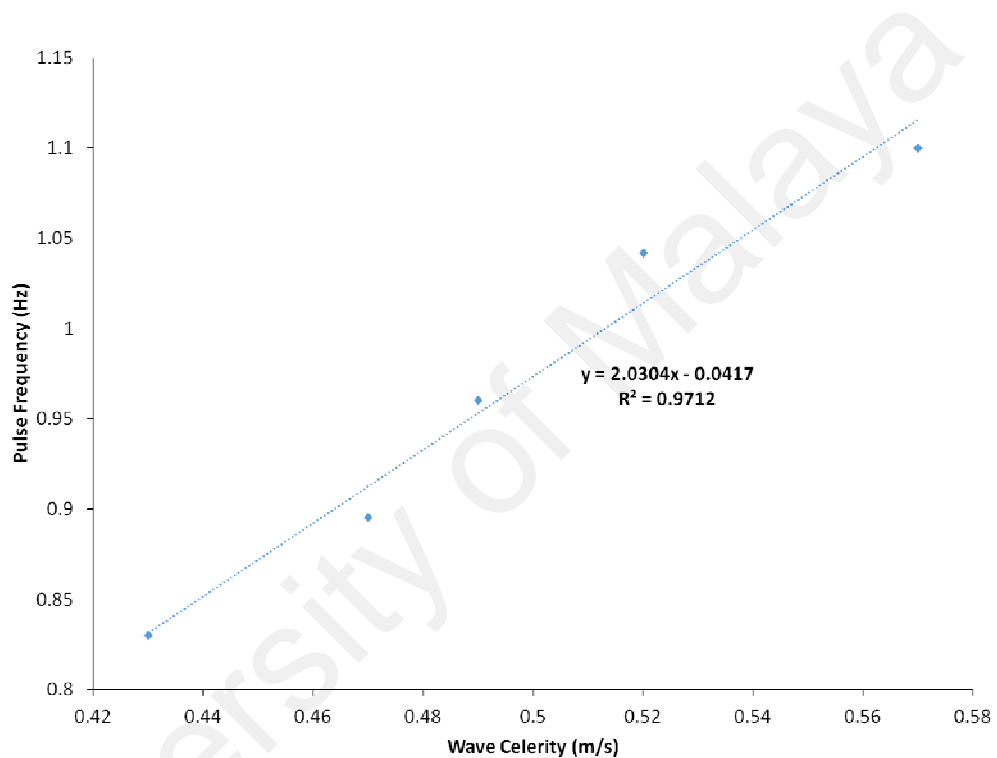


Figure 4.11: Average output power pulse frequency at different wave celerity

4.4 Summary

In conclusion, a packaged SMS fiber structure was experimentally investigated in a water flume to gauge water waves. The results indicated that the packaged SMS structure was capable of serving as a wave gauge at relatively high sensitivity. The SMS sensor responded to increases in the fundamental harmonic frequency of 2.0304 Hz at a wave celerity of every 1m/s wave under intermediate depth wave conditions. In addition, the sensor was capable of providing a sensitivity of 1.5613 Hz/ m in sensing wavelengths.

University of Malaya

CHAPTER 5: SINGLEMODE-MULTIMODE-SINGLEMODE FIBER STRUCTURE AS COMPRESSIVE STRAIN SENSOR ON A REINFORCED CONCRETE BEAM

5.1 Introduction

The term “structural health monitoring” (SHM) relates to the method used to evaluate the failure mechanism in many infrastructural structures, aviation, etc (Sohn et al., 2004). Following disaster occurrences such as landslides and earthquakes, SHM is used to monitor real-time circumstances and to generate accurate data on the structural integrity of structures. The sensor is the most important element in SHM because it detects local damage and failure risks, such as crack spots, bonding in the structure, and deformations in the civil system.

Most SHM systems use strain detectors of electrical resistance, strain gauges of vibration wire and piezoelectric accelerometers as detection device. Although these sensors have been used in civil structures for many years, alternative methods are required due to their inability to withstand electromagnetic wave interference (EMI), water shortage, and corrosion. In the past, fiber optic sensors (FOS) were well performed in monitoring risk in buildings owing to their capability to solve flaws in traditional detectors (H.-N. Li, Li, & Song, 2004). FOS has several favorable features, such as its relatively small size, immune to electromagnetic interference, low cost, and its competitiveness with other methods.

Multimode interference in a SMS fiber structure has been investigated recently. It has been demonstrated effectively as a sensor of temperature, load sensor, displacement sensor, bandpass filter and refractometer (A. Mehta, 2003; Antonio-Lopez, Castillo-

Guzman, May-Arrijoja, Selvas-Aguilar, & LiKamWa, 2010; Mohammed, Smith, & Gu, 2006; Silva et al., 2012; Tripathi et al., 2009; Qian Wang & Farrell, 2006).

A standard SMS structure comprises a MMF segment (MMF) fusion-spliced between two SMFs, Where a broadband light source is fed into SMS, multimodal excitation, multimode interference and light recouplement from MMF to SMF produce a modulated transmission spectrum. The pattern of multimode interference can be altered when a strain is introduced to the MMF (Tripathi et al., 2009; Qian Wang et al., 2008). A study of the SMS fiber structure to measure the compressive strain on a reinforced concrete beam was presented in this chapter. Although past studies used SMS on simple civil structure such as steel bar (Masnan et al., 2016) and cantilever beam (Yong Zhao et al., 2014), this is the first attempt to explore SMS fiber structure on a reinforced concrete beam.

A reinforced concrete beam that met the requirements of Euro code (EC2) was designed and constructed in this study. Figure 5.1 illustrates the beam's cross-sectional and side perspectives; all sizes are in millimeters (mm). As shown in the figure, the panel is 3120 mm long, 250 mm high and 150 mm broad. The concrete beam is reinforced by using shear connections to perform diagonal shear forces. Twenty-one R6 steel stirrups are arranged at 150 mm intervals. Additionally, the beam is reinforced by longitudinal steel bars: two H10 steel bars are located at the top of the cross section and three H10 steel bars are located at the bottom of the cross section.

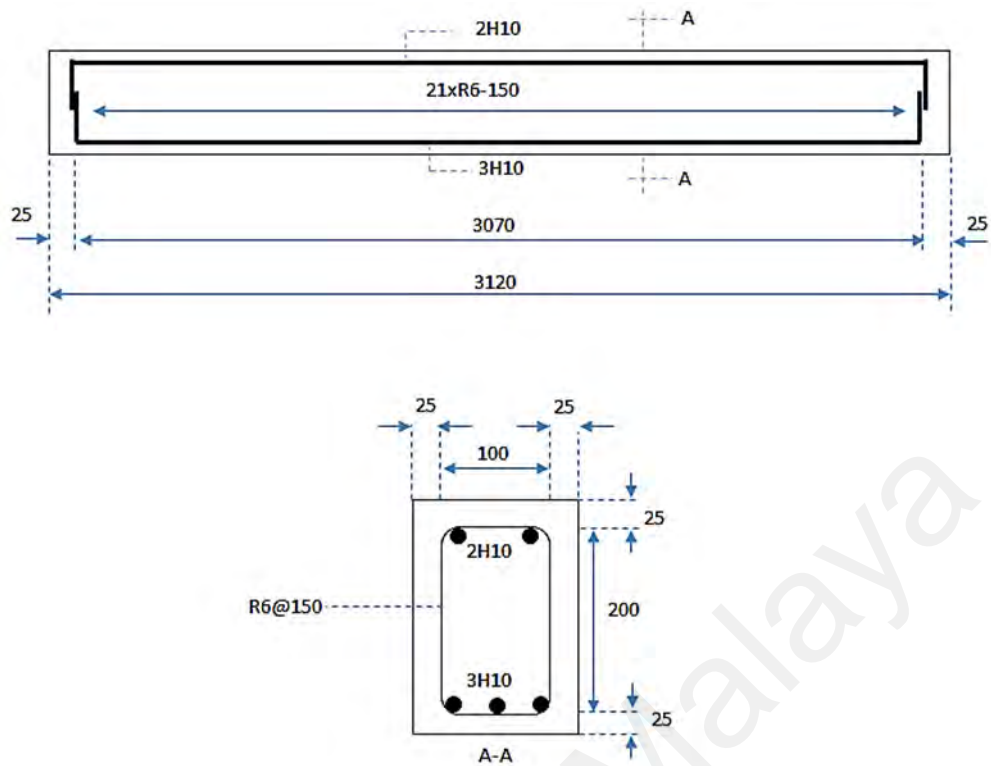


Figure 5.1: Reinforced concrete beam design

The concrete beam has been constructed by blending granite, sand, water and cement as shown in Table 5.1. Portland cement which is widely accessible in Malaysia was blended by adding water to a concrete mixer. The cement-to-sand ratio was 0.458 and the water-to-cement ratio (W / C) was 0.575.

Table 5.1: Concrete mixture preparation per meter cube

Materials	Volume (kg/m^3)
Cement	435
Sand	949
Granite	716
Water	250

The slump test was performed on the concrete blend in which 80 mm slump was achieved. The fresh concrete was then poured into a steel mold; a steel cage was mounted appropriately inside the mold. The concrete was compacted using a vibrator. After the casting, the concrete beam was complete, after which it was demolded after a week. Concrete strength was obtained by casting 12 cube samples of 100x100x100 mm per unit. Three samples of 200 mm cylinders in height and 100 in diameter were cast for use in the splitting test, which was performed on the same day the beam test was performed. The concrete beam and samples were cured by water for 28 days. The average compressive concrete strength in the cubes was 37.67 MPa, and the cylinder samples had an average tensile strength of 3.03 MPa.

5.2 Compressive Strain Experimental Setup

Figure 5.2 illustrates the experimental arrangement used to measure the compressive strain on the fabricated reinforced concrete beam. An Instron universal testing machine with a static load capability of 2000 kN was used to apply a compressive load at the middle of the beam as shown in Figure 5.3. The load was distributed by two point loads at the top and the mid-span of the reinforced concrete beam. The distance between the two point loads was 1 m. The reinforced concrete panel was supported on the hinged end and roller end over a clear span of 2.82 m.

The overhang was 0.15 m at each end as shown in Figure 5.2. The mid-span surface of the beam was fitted with an electrical resistance strain gauge with a cyanoacrylate glue. Thermoplastic adhesive was then used to cover the top of the gauge. The ER strain gauge was attached to data logger in order to read and record the strain values.

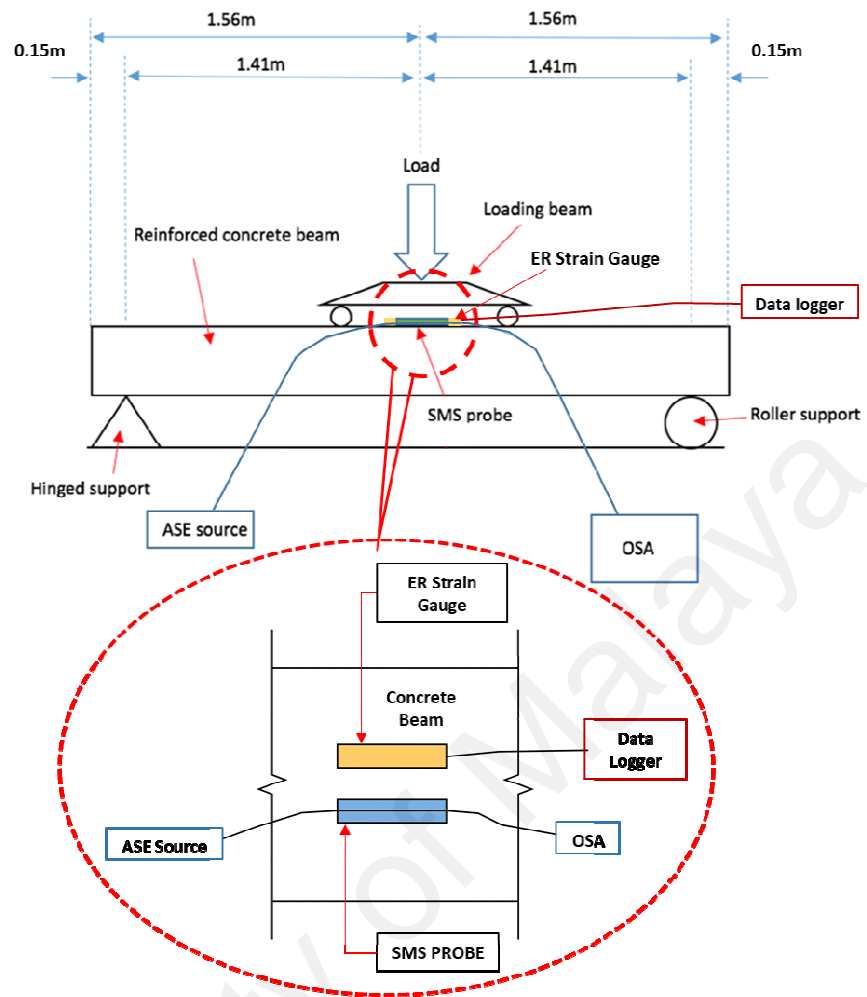


Figure 5.2: Experimental setup in measuring compressive strain using ER strain gauge and SMS sensor

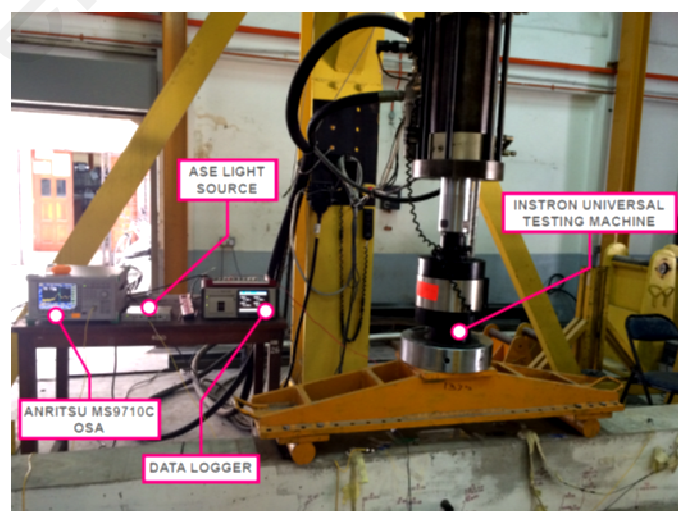


Figure 5.3: Photo image of the test-site in the Civil Engineering Laboratory, University of Malaya, Malaysia

The SMS fiber was used to verify the optical fiber sensor performance by measuring different strains on the reinforced concrete beam. The SMS fiber structure, as elaborated in Chapter 3 was formed by fusion splicing a MMF with both terminals of the SMF. The MMF used has step index profile with a core /cladding diameter of 105/125 microns. Epoxy adhesive was used to attach the SMS in a straight manner at the mid-span position on the top surface of the reinforced concrete beam and in parallel with the ER sensor. An ASE light source at the C-band wavelength was used as a light source, and an OSA, Aritsu MS9710C was used to capture spectral changes at the output of the sensor.

In order to apply and increase the amount of strain to the beam, the main applied load was increased from 0 kN and then gradually increased at the rate of 1.0 kN/min up to 31 kN. The amount of load applied ensured that the elasticity of the beam was maintained. The ER strain gauge and the SMS sensor measurements were simultaneously recorded for comparison when different loads were applied.

5.3 Results and Discussion

The bandpass transmission spectrum of the SMS at 0 kN loading is shown in Figure 5.4. It was captured at an OSA resolution of 0.1 nm and a span of 20 nm. A peak power was observed at wavelength of 1533 nm with regulated ambient temperature in the laboratory. MMF with length of 6.8 cm was used to form the SMS structure. The MMF length used is sufficient to experience micro bending effect that caused by the applied load on the SMS structure. The bending loss occurs due to the changes of the effective refractive index contrast between the core and cladding modes in the MMF segment. The intensity of the transmission power will change accordingly to the corresponding propagating coefficients and the excitation of the eigenmodes along the MMF.

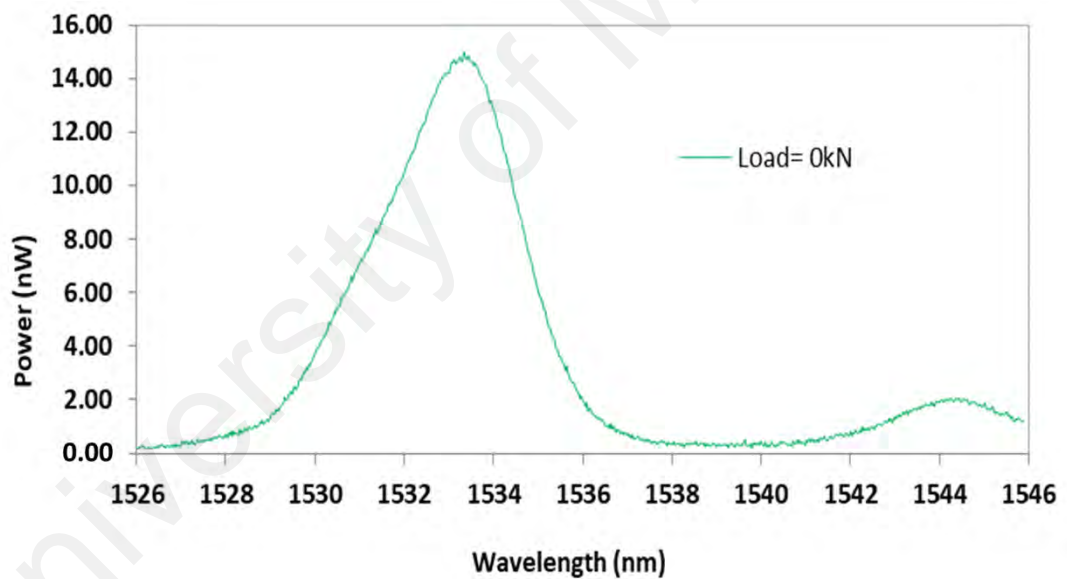


Figure 5.4: SMS bandpass transmission spectrum on a reinforced concrete beam at 0 kN loading condition

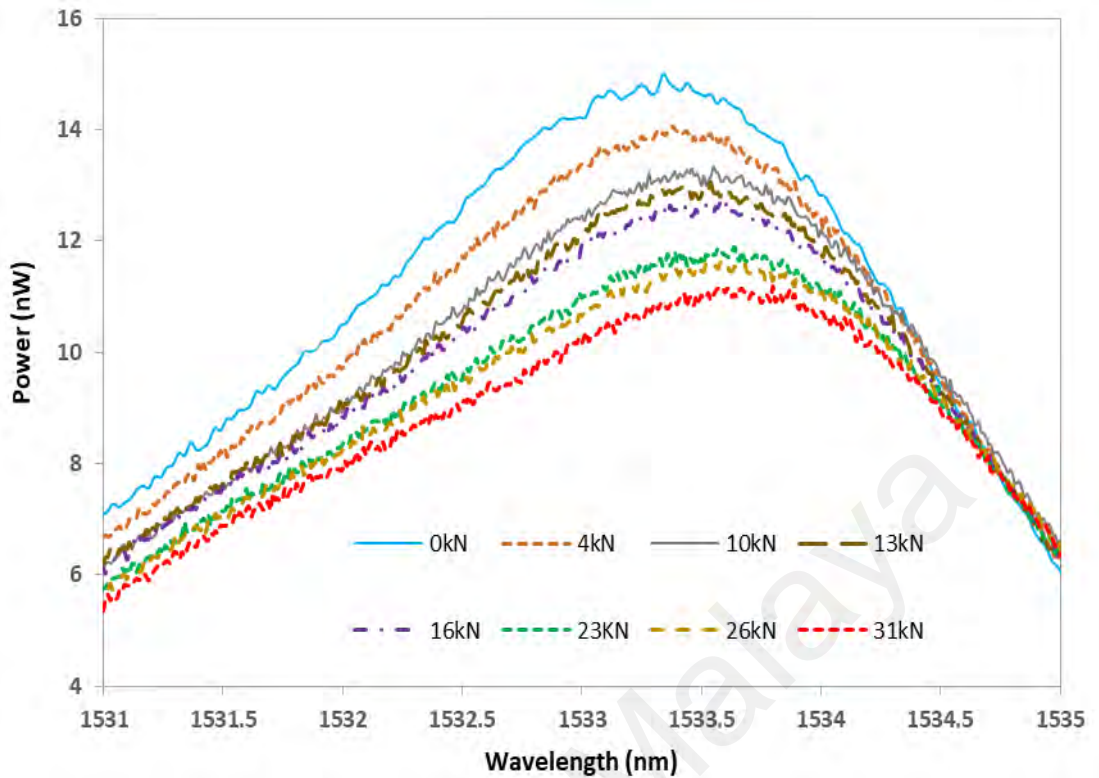


Figure 5.5: Peak bandpass spectra at different compressive loads

The measured spectral response of the SMS fiber structure, which was measured at the same OSA settings for various compressive loads, is shown in Figure 5.5. The observation of the spectral response was made with having the load gradually increasing at the increment rate of 1.0 kN/min up. The maximum applied load is 31 kN. The graph in Figure 5.5 shows that the peak wavelength of the output spectrum for each load has slightly shifted as the load was increased. The power of the spectra for various load is also decreasing as the load was increased.

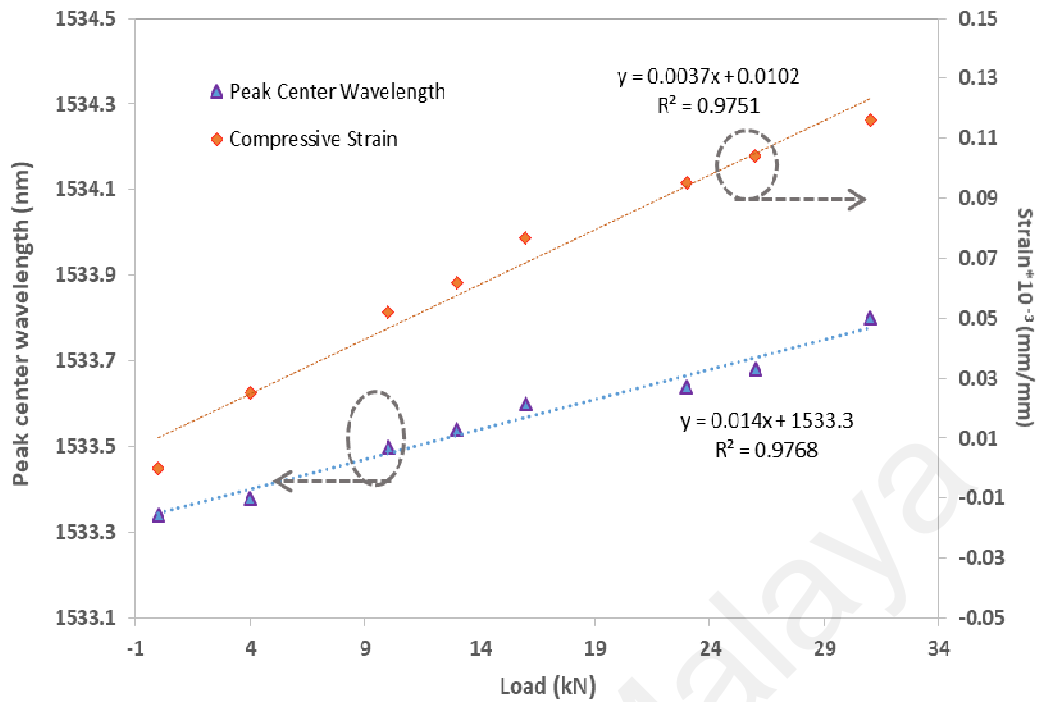


Figure 5.6: Compressive strain and spectral peak center wavelength at different compressive loads

Figure 5.6 shows the compressive strain using ER strain gauge and spectral peak wavelength of the SMS structure at different compressive loads. The compressive strain measured by the strain gauge was processed by a data logger. The maximum strain of 0.116 mm / mm was applied to the beam with an input compressive load up to 31 kN. It is observed that the SMS sensor acquired the sensitivity of 0.014 nm/kN with a linearity of 0.97676, meanwhile the ER strain gauge acquired a sensitivity of 0.0037 (mm/mm)/kN with a linearity of 0.97511. The peak of the bandpass transmission spectrum changed to a longer wavelength as the load increased. Theoretically, when light reaches at the SMF-MMF intersection of the SMS structure, higher order eigenmodes are excited and formed a regular modal interference along the MMF with varying phase velocity. The output power of the SMS structure is depending on the relative phase difference between cladding and core modes along the MMF segment.

When load is applied on the SMS structure, the structure experiences changes in fiber dimensions and photoelastic effects, which leads to the changes of the relative phase difference between the modes. Therefore, transmission spectra of the SMS structure experiences wavelength shift due to the changes.

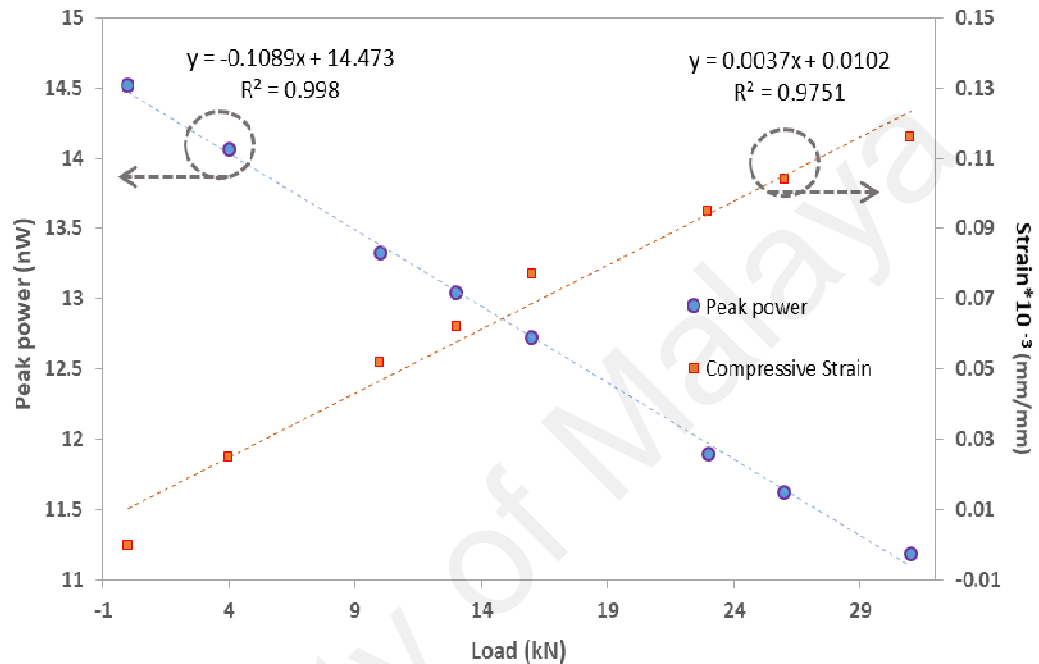


Figure 5.7: Compressive strain and spectral peak power at different compressive loads

Another notable observation was made in Figure 5.7, which illustrates the relationship between peak power and compressive strain measured by the ER strain gauge at various loads. Moreover, as the load increased, the recorded peak power was observed to decline at a slope of -0.1089 nW / kN and a linearity of 0.99795. When the load was applied to the sensor structure, the MMF fiber experienced small bending effect. The micro bending causes the redistribution of the mode field to move from fiber core towards the cladding layer, which leads to the guided modes couple to radiation modes. The bending loss is depending on the core radius, radius of curvature and

relative effective refractive index between cladding and core modes (Fang, Z. et al.; 2012). Therefore, the bending effect on the SMS structure causes to light intensity to decrease.

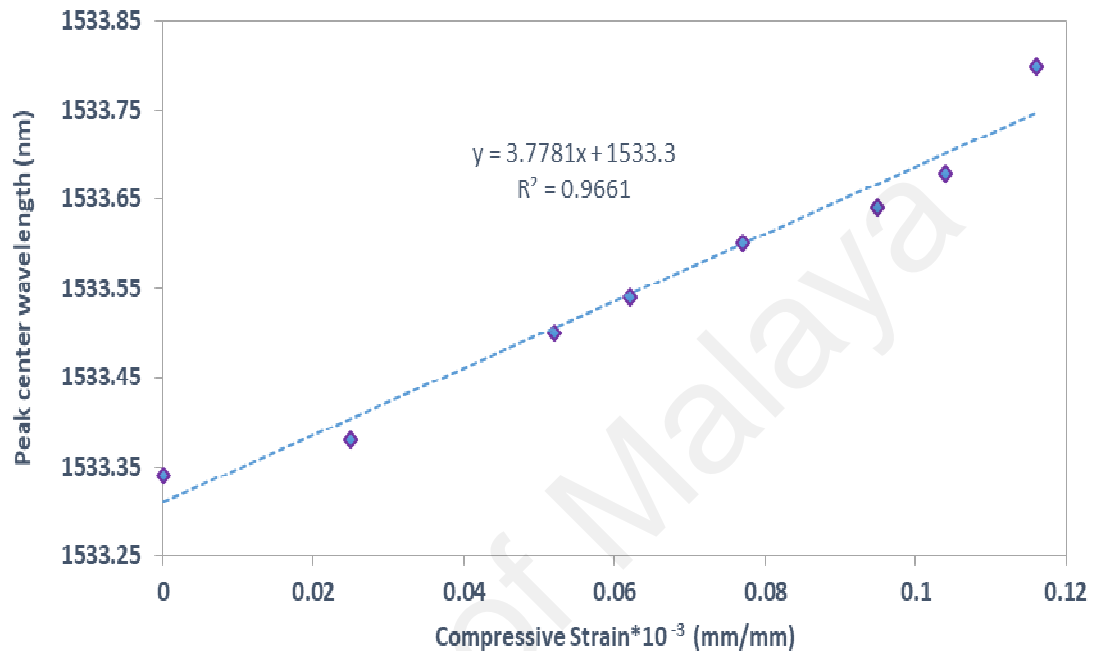


Figure 5.8: Relation between the spectral peak center wavelength and the compressive strain

Figure 5.8 illustrates the relation between the spectral peak center wavelength and the compressive strain. It was noted that the curve was increased linearly with increments of compressive strain at a slope of 3.7781 nm/(mm / mm) and a linearity of 0.96606. Compared to the previous work by S. Sun (2017), the authors developed twisted MMF in SMS structure as strain sensor. Although the strain sensitivity measurement was achieved at 42.5 pm/ $\mu\epsilon$, the fabrication process which required heating and rotating fiber to form twisted structure is complicated. In addition, the work was tested on the displacement platforms in the laboratory setup instead on testing on the civil structure. In contrast, the proposed SMS structure in this work has been teste

on the reinforced concrete beam and capable to achieve fairly high sensitivity on strain measurement. Therefore, the proposed SMS structure can be competitive candidate for the use in strain measurement applications.

5.4 Summary

This experimental work demonstrated that a simple SMS fiber structure was capable of measuring the strain in a reinforced concrete beam, which is a heavy and rigid civil structure. This work also demonstrated the method used to fabricate a reinforced concrete beam that complied with the Euro code (EC2) standard. The findings showed that the SMS fiber sensor offered a sensitivity of 3.7781 nm/ (mm / mm) and a linearity of 0.96606 in compressive strain readings up to a maximum of 0.116 mm / mm.

CHAPTER 6: INVESTIGATION ON MULTIMODE UNCOATED SINGLE-MODE MULTIMODE FIBER STRUCTURE FOR VIBRATION DETECTION

6.1 Introduction

Deterioration of civil infrastructure such as composite structure, platforms, bridges, buildings and railways is subject to long-term continuous usage, excessive loading and adverse environmental conditions. It is essential to monitor the structural system's health and performance continuously to prevent massive damage and losses. Vibration-based damage detection methods such as changes in natural frequency, modal stiffness, frequency response function and its curvature are commonly implemented to structural health monitoring of civil infrastructure. SHM with integration of fiber optic sensing system which includes fiber laser, optoelectronics, microelectronics etc. has become the trend nowadays. As mentioned earlier, optical fiber sensors have many benefits such as light weight, portable and immune to electromagnetic interferences

The FBG sensors have developed leading and mature technology in fiber optic sensor systems. FBG sensors exhibit their potential for vibration, strain and temperature measurement, as they offer high resolution and range, compact size, multiplex capability and resistant to hostile environments. There are numerous methods for fiber optic vibration detection that have been widely explored. Tsuda (2010) used the FBG sensor to demonstrate an extremely sensitive vibration detection scheme. The FBG detector functions as a loop cavity mirror to detect vibration up ultrasound frequency with the presence of strain or temperature on the sensor.

In 2015, an embedded Mach Zehnder interferometer and FBG sensor was developed to detect vibrations of high frequency voltage for non-destructive testing. The proposed sensor, consisting of a 60 mm SMF with a 12 mm spliced in between two 3 mm FBG, is also capable of simultaneously sensing localized temperature and strain (Q. Wu et al., 2015). Z. Zhang and Liu (2017) developed FBG vibration sensor to monitor the degree and orientation of the critical parts, which is capable to measure the vibration frequency up to 100Hz. However, a complicated interrogator is needed to execute a FBG detection scheme. Demodulation method is needed to obtain FBG's reflected signals (Majumder et al., 2008).

Another optical fiber sensor relying on multimode interference in SMS has been explored and used in many detection systems. The fiber structure not only offers comparable features as FBG, but also makes it easier to construct and requires a simpler measurement scheme. A normal SMS structure is unable to have high sensitivity to detect vibration. Thus, the cladding of the MMF of the SMS structure is chemical etched using chemical compounds (Qiang Wu et al., 2011). The fabrication is much more complicated as it involves chemical etching which requires cautious and precise handling. Another work proposed an optical fiber vibration sensing based on the single mode- coreless- single mode structure. The designed scheme exhibits high sensitivity and rapid response in detecting vibration frequency in real time monitoring. The experimental results demonstrated that the system can detect a frequency range from 100 Hz to 29 kHz with the no core fiber employed as multimode waveguide (Ran et al., 2015).

The MSM scheme is used as a vibration sensor in this work to measure vibration frequency. As mentioned previously in Chapter 3, the design of MSM is distinguished from the structure of SMS. The modal interferences that occur between SMF core mode and cladding mode in MSM configuration.

6.2 Fabrication of sensor probe

As described on the making of the MSM sensor device in Chapter 3, the structure is constructed by fusion splicing a section of uncoated SMF between two brief segments of MMFs. This configuration offers the interference interacting in the SMF between the core and cladding modes and meanwhile the MMFs act as mode couplers. The MSM structure used for vibration measurement must only operate at controlled ambient temperature. Based on the MSM structure's prior temperature assessment, it is susceptible to temperature fluctuations owing to the large distinction in effective index between the structure's cladding and core mode.

The materials used in this work are SMF-28 (8.2/125 μm core / cladding diameter) and Thorlabs MMF FG105LCA (pure silica core with fluorine-doped silica, 105/125 μm core / cladding diameter). The length of the uncoated SMF is 2.5 cm and both MMFs are cleaved to have a coherent length of 5.0 cm as shown in Figure 6.1.

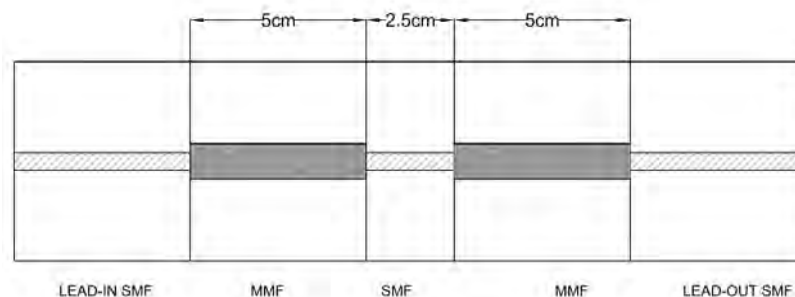


Figure 6.1: Schematic diagram of MSM structure

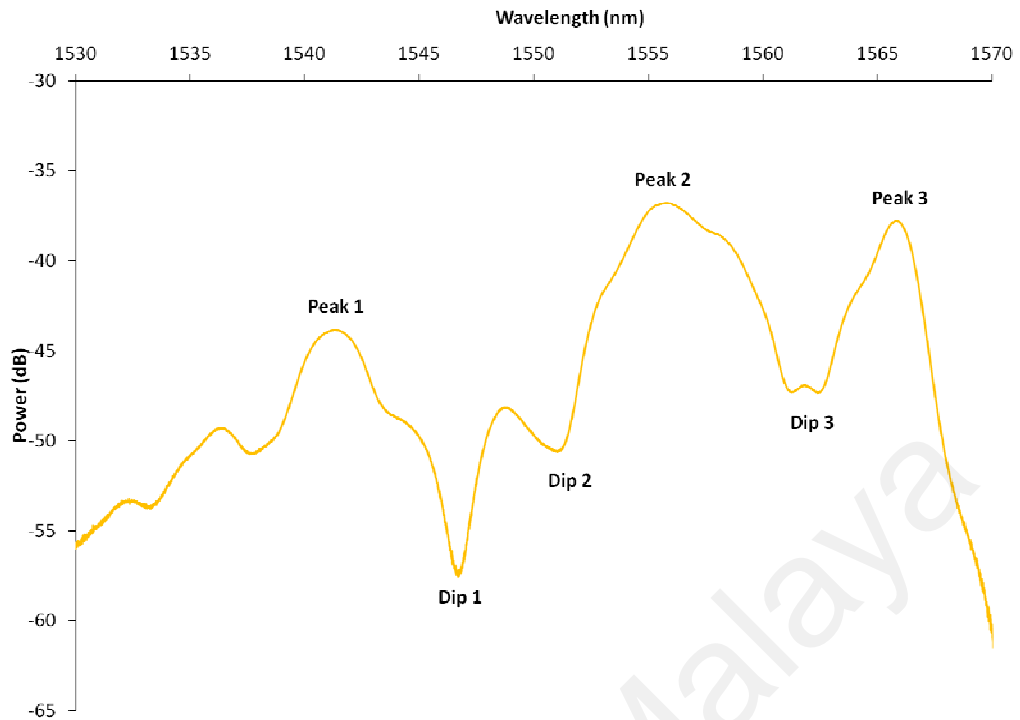


Figure 6.2: Transmission spectrum of the MSM structure

As seen in Figure 6.2, inhomogeneous interference trend exhibits in transmission spectra owing to cladding mode excitation of the SMF. The light source is supplied to the MMF1 of the MSM structure from a lead-in SMF. Due to the large core diameter misalignment, a portion of the power will be coupled to the SMF cladding modes at the lead-in SMF-MMF1 junction. When the light enters the SMF-MMF2 junction, partly the SMF's cladding modes and core mode are coupled to the MMF2. The MMF length may influence the transmission spectrum interference pattern. It is suggested to keep the MMF section as short as possible in order to avoid large guided modes phase differences.

6.3 Experimental setup for vibration test

Figure 6.3 shows the experimental set-up for vibration testing. Light at 1550 nm from the C-band light source was used for input SMF for the MSM sensor probe, and the output SMF was attached to the DET01CFC/M Thorlabs photodiode detector. The photodiode detector transformed the optical signal from the lead-out SMF to electrical signal and the signal was obtained using a digital oscilloscope. The MSM sensor was fitted to a speaker diaphragm and the signal generator provided the vibration source, producing sinewave shapes over frequencies up to 6 kHz. As the speaker is connected to signal generator, the diaphragm that attached to the electromagnetic coil is vibrating and producing audio frequency.

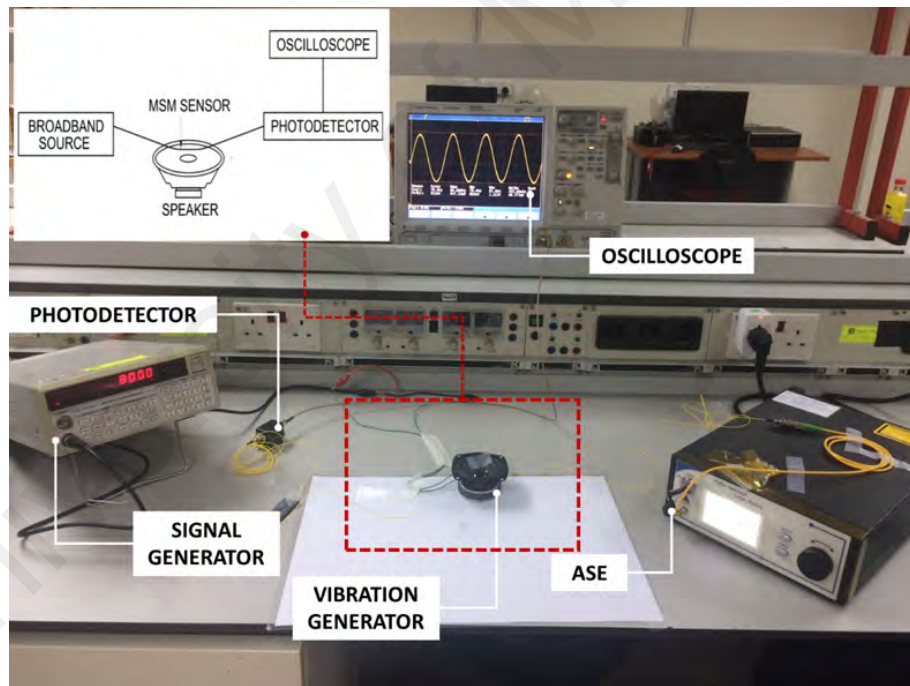


Figure 6.3: Experimental setup in detecting vibration using MSM sensor

6.4 Results and discussion

When the vibration sensing test takes place, the signal supplied by the signal generator causes the speaker to vibrate. The vibration source also affects the MSM sensor probe, which modulates the output light intensity. The waveform from various frequency settings was observed from the digital oscilloscope. The output was acquired from the photodiode detector as the transmission spectrum consists multiple peaks and dips. It is difficult to observe the changes of the spectral changes. Figure 6.4 shows the photo image of the waveform of 3.99 kHz displayed on the digital oscilloscope when the speaker is supplied with 4.0 kHz sinusoidal waveform from the signal generator.

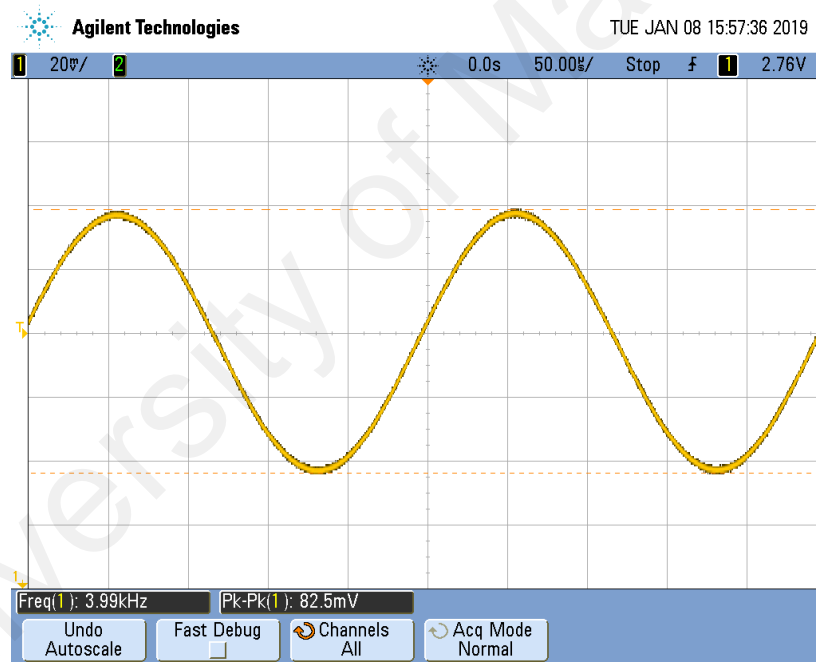
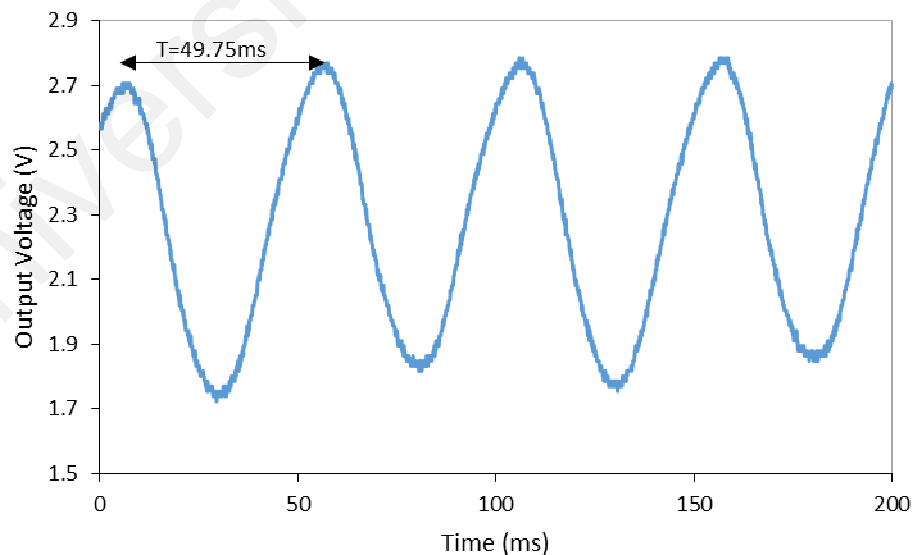
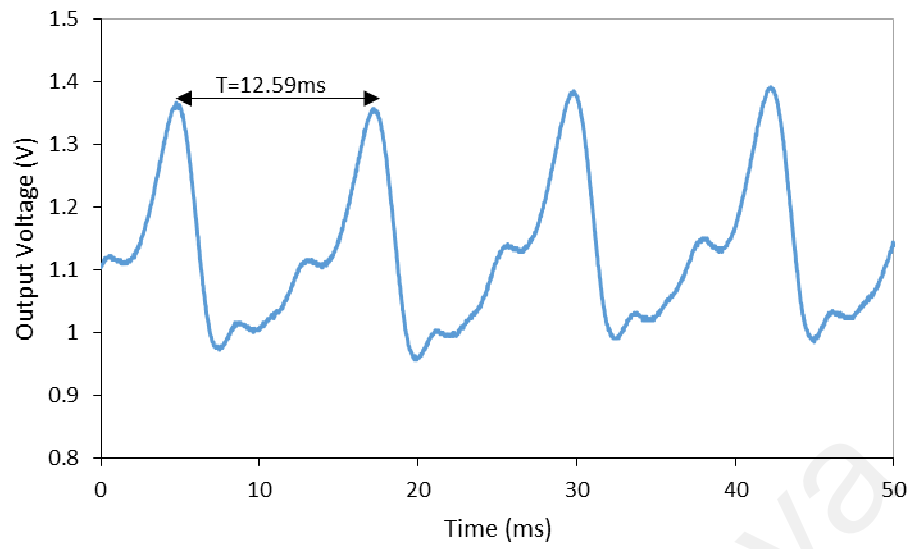


Figure 6.4: Photo image of the waveform of 4.0 kHz using digital oscilloscope

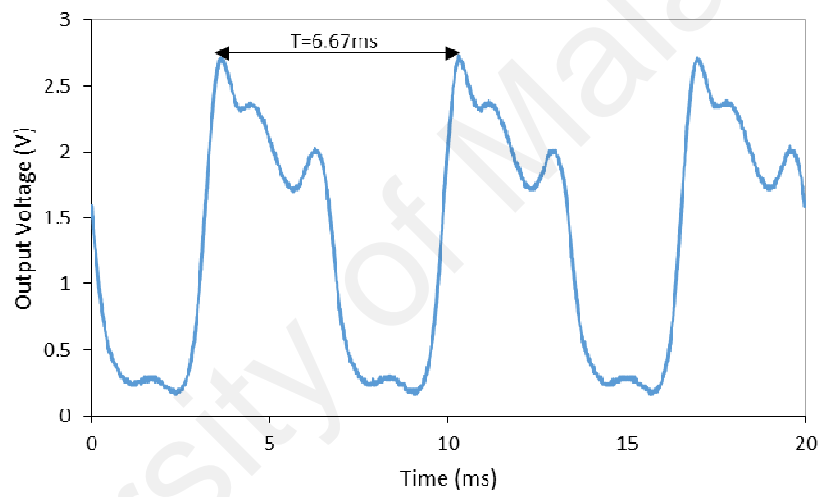
Various vibration frequency will produce distinct change in output light intensity of the MSM sensor probe. Under the constant vibration intensity, the waveforms of 20 Hz–6 kHz are detected. All detected waveforms from various frequency settings were recorded in Figure 6.5. When the sensing SMF vibrates, photoelastic effect occurs and leads changes to the effective refractive index difference between the modes. Therefore, the light intensity changes correspondingly to the change of the external perturbation. The transmission power of the MSM structure is the resultants of the interference of the cladding and core modes of the sensing SMF. When the MSM structure experiences vibration, the periodical intensity at the interference wavelength will experiences changes. Based on the observation of the graphs obtained, waveforms of 80 Hz, 150 Hz and 300 Hz seemed distorted. These waveforms are distorted as the PD detector converts the optical signal to certain electrical signal which is responded to the light intensity at the output of the structure. However, the detected waveforms are in consistent periodical manner which is able to detect the corresponding frequency.



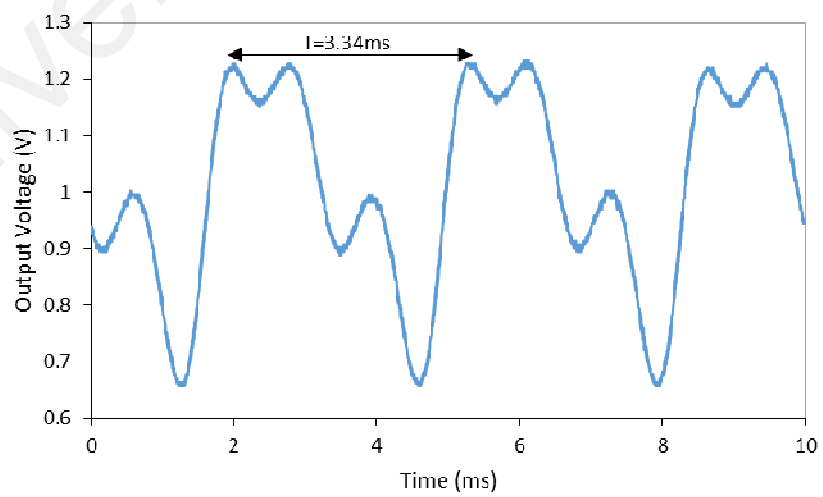
a) 20 Hz



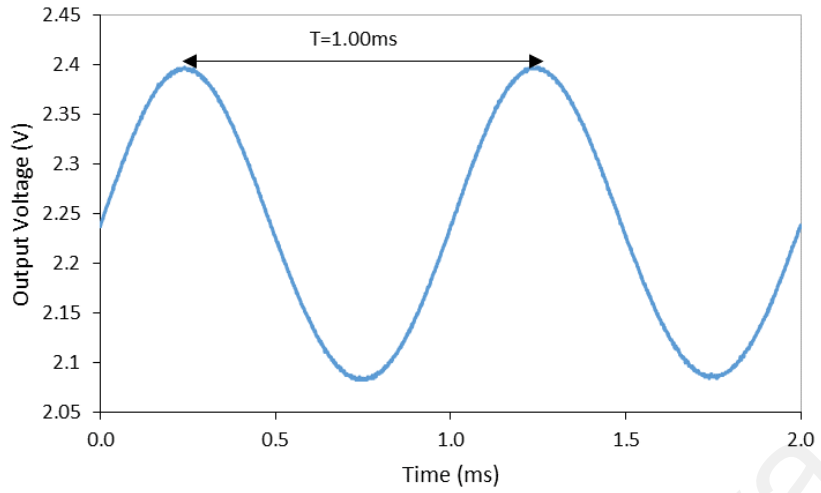
b) 80 Hz



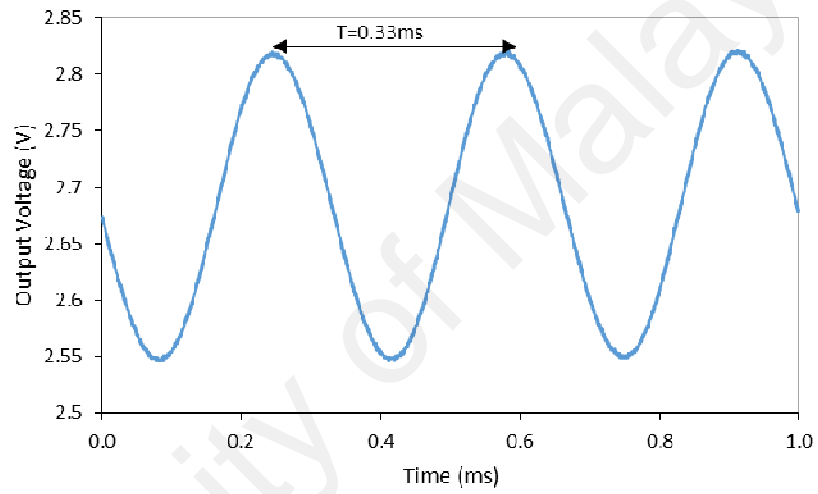
c) 150 Hz



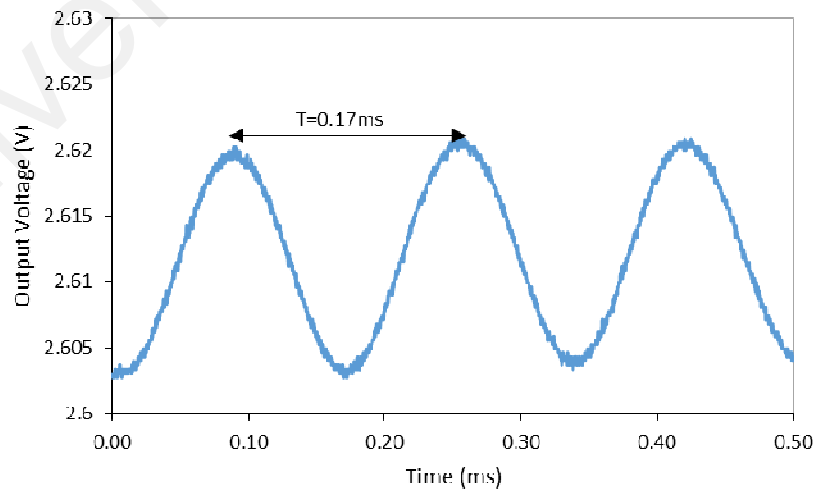
d) 300 Hz



e) 1 kHz



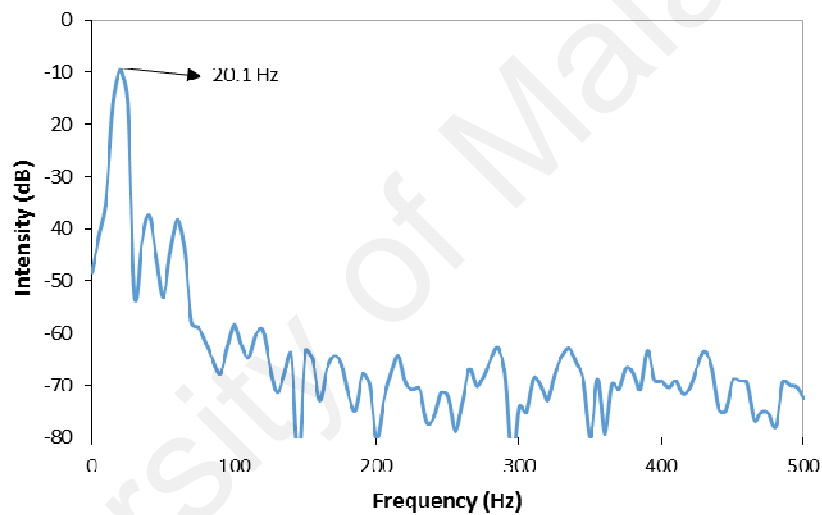
f) 3kHz



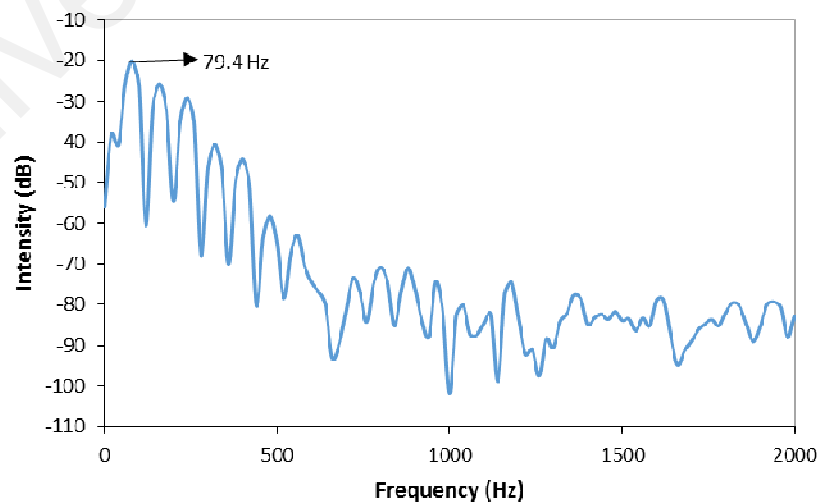
g) 6kHz

Figure 6.5: Waveform Detection at different frequency: a) 20 Hz, b) 80 Hz, c) 150 Hz, d) 300 Hz, e) 1kHz, f) 3 kHz, g) 6kHz

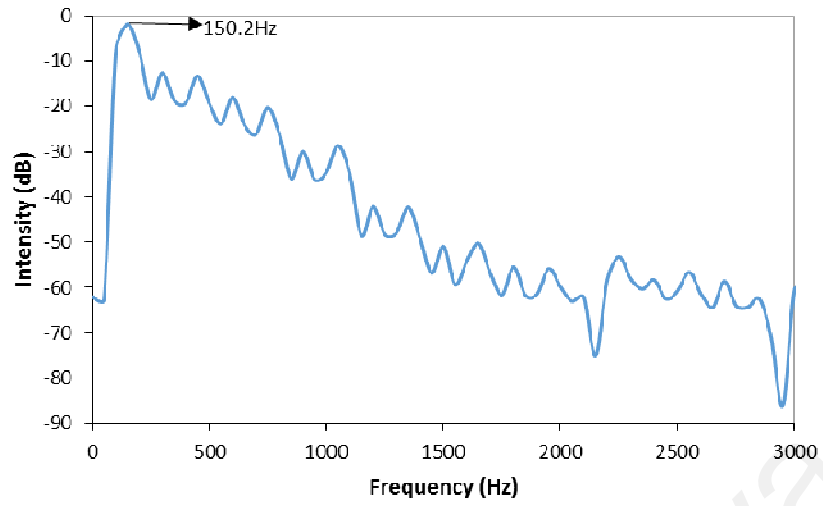
Fast Fourier Transform (FFT) is performed to time domain measurements to acquire the vibration frequency. The DC component of the time domain data is removed by deducting mean value from the signal. Figure 6-6 displays 150 Hz, 300 Hz, 1 kHz, 3 kHz and 6 kHz frequency response curves under the same vibration intensity. The detected frequency is the fundamental frequency at the peak power intensity of the frequency spectrum. It is inferred that the fundamental frequency detected by the MSM detector is well-matched with the supplied frequency. The MSM detector probe can certainly measure the vibration frequency in the frequency range from 20 Hz to 6 kHz.



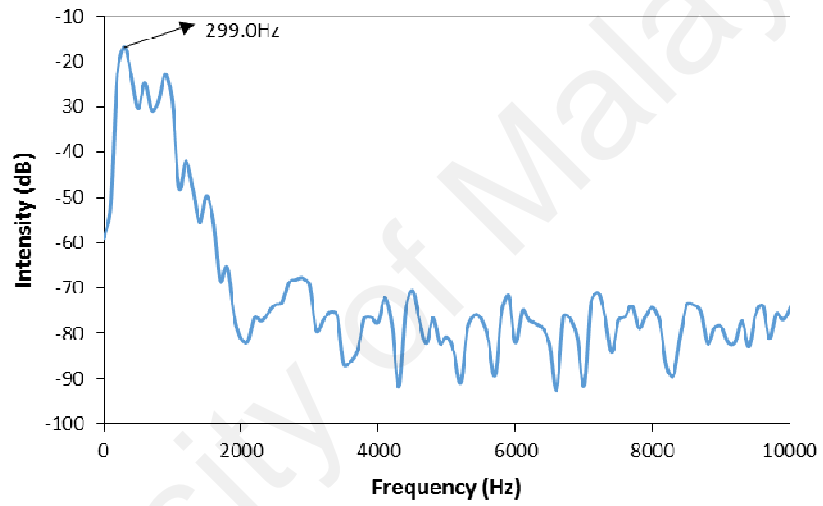
a) 20 Hz



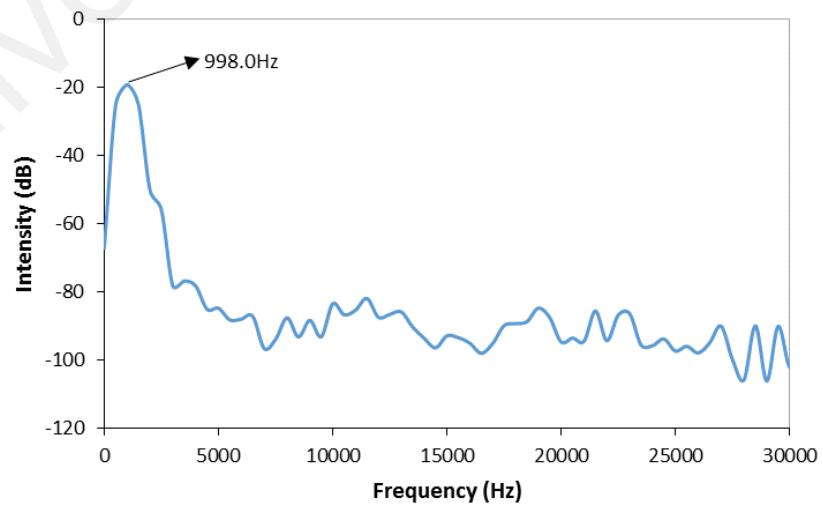
b) 80 Hz



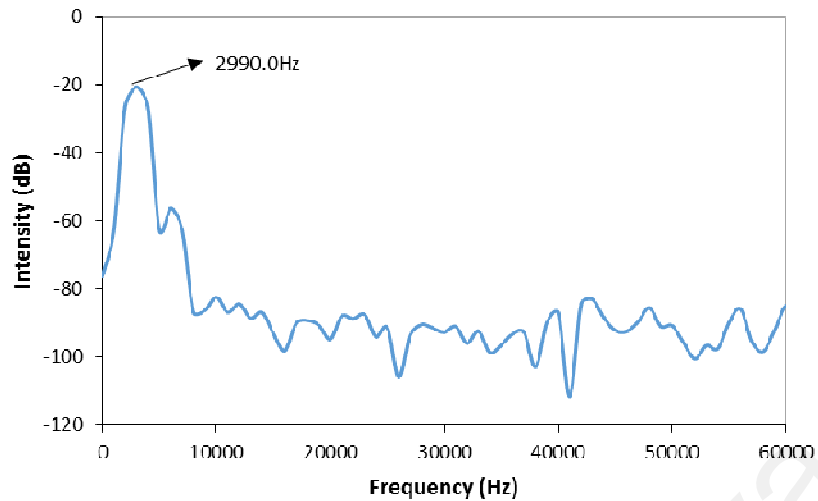
c) 150 Hz



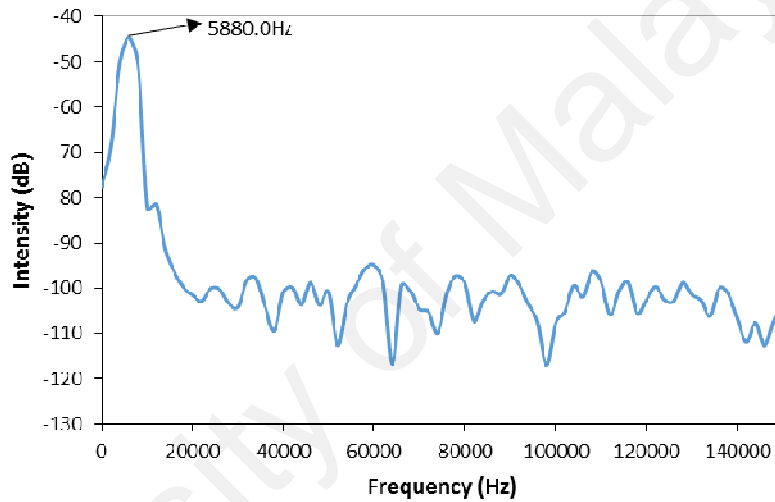
d) 300 Hz



e) 1 kHz



f) 3kHz



g) 6kHz

Figure 6.6: Frequency Response : a) 20 Hz, b) 80 Hz, c)150 Hz, d) 300 Hz, e) 1kHz, f) 3 kHz, g) 6kHz

Although the frequency spectrum contains higher order harmonics, the power intensity of these harmonics are in small amplitude and not causing excessive distortion to the detected frequency. Thus, the low levels of these harmonics are insignificant and do not affect the sensing capability of the MSM structure. It can be inferred that the MSM structure is capable of detecting wide range vibration frequency, ranging from 20 Hz up to 6 kHz. Table 6.1 tabulates the relative error of frequency measurement. The measurement of frequency is highly accurate with relative errors not more than 2 %. As

compared to the SMS structure that proposed by Yong Zhao et al. (2014), the structure was only able to detect up to 100 Hz with maximum relative error of 3.33 %. On the other hand, the recent work by R. Gao et al. (2018) revealed the development of a tapered SMS structure to detect low frequency. Although the structure is able to achieve measurement sensitivity more than 40 times than the normal SMS structure, the tapered SMS structure is limited to detect frequency up to 300 Hz. Due to its limitation in measurement and also complicated fabrication process, the MSM structure is favorable as vibration frequency detector.

Table 6.1: Relative error of frequency measurement

Actual frequency (Hz)	Detected frequency (Hz)	Relative error (%)
20	20.1	0.50
80	79.1	1.13
150	150.2	0.13
300	299.0	0.33
1000	998.0	0.20
3000	2990.0	0.33
6000	5880.0	2.00

6.5 Summary

In summary, a frequency vibration sensor based on MSM configuration was proposed and experimentally proven. It was demonstrated that the sensing element, a sandwiched uncoated SMF with two MMF when adhered to the speaker by the epoxy adhesive, could sensitively detect the vibration signal. Experimental findings indicate that the frequency measured by MSM sensor can be well- matched to the frequency employed. The vibration frequency's maximum relative error is 2.00 %. The MSM sensor has a low temperature sensitivity of only 0.7 pm/ ° C within 25-38 ° C temperature range. Temperature disruption can therefore be ignored in the case of low temperature changes.

University of Malaysia

CHAPTER 7: CONCLUSION & RECOMMENDATIONS

7.1 Conclusion

The thesis presents an extensive work on the development of a fiber optic sensor for SHM based on multimode interference (MMI). These works include the fabrication, characterization and experimentation of the sensor probe on the civil infrastructure. Two distinct fiber sensor probes based on multimode interference (MMI), namely SMS and MSM fiber structures, were proposed and demonstrated for strain and vibration measurements. Both sensors can detect any variations in parameters as the structure's performance depends on the mode interference principle in the optical fiber. This research has successfully explored multimode interference (MMI) in the guided mode propagation of SMS and MSM fiber. This type of optical fiber sensors have gained tremendous interests in recent years particularly for SHM applications. They offer many advantages in term of fabrication cost, immunity to electromagnetic interference and compactness.

The optical sensors have been extensively developed to measure numerous physical and chemical parameters. They can also be used to substitute the conventional electrical strain gauge in SHM. Both SMS and MSM sensors were used in this thesis to measure strain based on modal interference impact within the proposed structures. The SMS structure was fabricated by fusion splicing both ends of MMF with SMF. The creation of the MSM structure is more complicated, since two SMS structures have been replicated. In addition, the structure of the MSM is more susceptible to temperature changes than the structure of the SMS. The unique packaging and installation method was effectively developed in this work by manipulating the bending impact. Based on the outcomes acquired in the load analysis, it is revealed that the special packaged SMS

structure has improved the structure's transmission spectral response. It generates multimode interference owing to the reflection at the splicing point between the SMF and MMF, which creates a regular modal interference along the MMF with varying phase velocity.

Coastal infrastructure development is generally complicated as it includes many design variables such as wave climate, temperature, precipitation, wind, etc. The safety of these buildings constructed along coastlines are priority, physical modeling is generally chosen to solve coastal engineering issues. This technique promotes better prediction in regulated settings. A laboratory flume with a wave maker is often used to make physical water wave models that include hydrodynamic forces, motion analysis, and wave patterns. In this work, a packaged SMS structure was used as a water level gauge. The SMS sensor is favorable as it is able to overcome the disadvantages of conventional wave gauges with added values of its simple structure, ease of fabrication and immune to electromagnetic field interference.

Straight SMS structure offers very restricted measurement as the fiber structure has the elevated risk of breakage when the greater strain or vibration amplitude is applied to it. In this thesis, a special packaged bent SMS was proved to provide wider strain measurement and elevated resolution with temperature compensation. For a curved MMF, the refractive index is asymmetrical along the fiber axis. It was found that the packaged SMS has gained temperature stability up to $0.0904 \text{ nm/}^\circ \text{C}$. It is also demonstrated that all SMS structures are capable of strain assessment for normal ambient environments as the performance of SMS will not be influenced by a small temperature disturbance.

The packaged SMS structure is elastic for small strains and returns to the original position after being bent. However, it is prevented to apply a higher quantity of strain greater than 451.106mN on the SMS as this quantity of strain poses greater than the elastic limit of the packaged SMS and then causes permanent deformation and fracture. This experimental research was confirmed with a comparable packaged FBG structure. The load on the FBG structure increased incrementally to 480.526mN. However, for various loads applied, there is no wavelength shift. The curved FBG structure is not susceptible to transverse strain / load detection.

The temperature response of the MSM structure was also experimentally proved in this research. The temperature sensitivity of the MSM fiber structure within the temperature range above 38 ° C is found to be 0.1896 nm/ ° C. It can be inferred that the MSM structure works better for temperature monitoring relative to the SMS structure owing to the large efficient refractive index distinction of the thermal coefficient of the core and cladding mode. Since numerous vibration-based identification methods have been introduced to civil infrastructure for structural health monitoring, the MSM sensor probe was developed in this work to assess the vibration frequency of mechanical vibration. The experimental result proved that the MSM structure is capable in detecting a wide range of vibration frequency, ranging from 20 Hz up to 6 kHz. The measurement of frequency was highly accurate with relative errors of less than 2%.

7.2 Future Works

The proposed structure-based SMS and MSM sensors for civil structural monitoring applications were successfully evaluated in this thesis. These proposed sensors can measure strain and vibration at specified local point in a structure. The sensing principle is based on detecting the optical phase change induced in the propagating light along the optical fiber. Constructive interference occurs in the sensing structure when two interfering waves are in phase, which resulting in maximum amplitude. Meanwhile, destructive interference occurs when two interfering waves are out of phase and obtains minimum amplitude.

These MMI sensors are basically a point sensor with have limitation to assess the performance of the large scale civil structure. Therefore, the future work shall focusses on developing these sensors for distributed sensing. Distributed sensing scheme will be most suited for large civil structural monitoring as it can provide fully distribution sensing information along the optical fiber, therefore external perturbation signal from any location can be detected. The distributed sensing scheme requires comprehensive investigations on the determination of exact fault location on a large scale with measurement of relative optical phases shift.

This work can also be extended to investigate the different shapes and waist diameters of the fiber in order to enhance the sensitivity of the sensor probes. The sensor structure may be tapered on the diameter waist of the sensing element or reshaping into elliptical structure to suit the strain and vibration measurement in real application. However, this work requires the establishment of high-durable structure in order to perform in harsh environment and meanwhile, produce effective composite interference within the sensing element.

Another recommendation for future work is to enhance the packaging of the optical sensor probe. The work involved should be investigating on different packaging materials subjected to various conditions such as operating temperature, humidity and usage in the hazardous environment. In order to provide effective mechanical contact between the fiber and the civil structure host, the packaging scheme for optical sensor probes is very crucial. The sensor probe will only provide accurate sensing for the measurands of interest. Different packaging materials also offer different protection schemes in the targeted sensing region. Future study shall look into the potential packaging schemes for various host materials as delicate attention and various measures need to be taken during the installation of the optical sensor probe.

REFERENCES

- Andrade, C., & Alonso, C. (2001). On-site measurements of corrosion rate of reinforcements. *Construction and Building Materials*, *15*(2), 141-145.
- Antonio-Lopez, J. E., Castillo-Guzman, A., May-Arrijoja, D. A., Selvas-Aguilar, R., & LiKamWa, P. (2010). Tunable multimode-interference bandpass fiber filter. *Optics Letters*, *35*(3), 324-326.
- Antunes, R. A., Cortez, N. E., Giancesini, B. M., & Vieira Filho, J. (2019). Modeling, Simulation, Experimentation, and Compensation of Temperature Effect in Impedance-Based SHM Systems Applied to Steel Pipes. *Sensors (Basel)*, *19*(12), 2802.
- Baharin, N. F., Azmi, A. I., Abdullah, A. S., & Mohd Noor, M. Y. (2018). Refractive index sensor based on lateral-offset of coreless silica interferometer. *Optics & Laser Technology*, *99*, 396-401.
- Bai, Z., Zhang, W., Gao, S., Zhang, H., Wang, L., & Liu, F. (2015). Bend-insensitive long period fiber grating-based high temperature sensor. *Optical Fiber Technology*, *21*, 110-114.
- Becker, T., Ziemann, O., Engelbrecht, R., & Schmauss, B. (2018). Optical Strain Measurement with Step-Index Polymer Optical Fiber Based on the Phase Measurement of an Intensity-Modulated Signal. *Sensors (Basel, Switzerland)*, *18*(7), 2319.
- Bezombes, F. A., Lalor, M. J., & Burton, D. R. (2007). Contact microphone using optical fibre Bragg grating technology. *Journal of Physics: Conference Series*, *76*, 012017.
- Bhardwaj, V., & Singh, V. K. (2017). Study of liquid sealed no-core fiber interferometer for sensing applications. *Sensors and Actuators A: Physical*, *254*, 95-100.
- Bhatia, V., & Vengsarkar, A. M. (1996). Optical fiber long-period grating sensors. *Optics Letters*, *21*(9), 692-694.
- Bremer, K., Wollweber, M., Weigand, F., Rahlves, M., Kuhne, M., Helbig, R., & Roth, B. (2016). Fibre Optic Sensors for the Structural Health Monitoring of Building Structures. *Procedia Technology*, *26*, 524-529.
- Bryngdahl, O. (1973). Image formation using self-imaging techniques. *Journal of the Optical Society of America*, *63*(4), 416-419.
- Canning, J., & Carter, A.. (1997). Modal interferometer for in situ measurements of induce core index change in optical fibers. *Optics letters*. *22*. 561-3. 10.1364/OL.22.000561.

- Cazzulani, G., Cinquemani, S., Comolli, L., Gardella, A., & Resta, F. (2014). Vibration control of smart structures using an array of Fiber Bragg Grating sensors. *Mechatronics*, 24(4), 345-353.
- Chan, T. H. T., Yu, L., Tam, H. Y., Ni, Y. Q., Liu, S. Y., Chung, W. H., & Cheng, L. K. (2006). Fiber Bragg grating sensors for structural health monitoring of Tsing Ma bridge: Background and experimental observation. *Engineering Structures*, 28(5), 648-659.
- Chen, X., Zhou, K., Zhang, L., & Bennion, I. (2005). Simultaneous measurement of temperature and external refractive index by use of a hybrid grating in D fiber with enhanced sensitivity by HF etching. *Applied Optics*, 44(2), 178-182.
- Chen, Y., Han, Q., Liu, T., Lan, X., & Xiao, H. (2013). Optical fiber magnetic field sensor based on single-mode-multimode-single-mode structure and magnetic fluid. *Optics Letters*, 38(20), 3999-4001.
- Chen, Y., Han, Q., Liu, T., & Lü, X. (2015). Self-temperature-compensative refractometer based on singlemode-multimode-singlemode fiber structure. *Sensors and Actuators B: Chemical*, 212, 107-111.
- Chtcherbakov, A. A., & Swart, P. L. (2004). Chirped fiber-optic Bragg grating interrogator in a multiplexed Bragg grating sensor configuration. *Journal of Lightwave Technology*, 22(6), 1543-1547.
- Elangovan., A. L. M. (2008). CFD Simulation and Validation of Flap Type Wave Maker. *Journal of World Academy of Science, Engineering and Technology*, 46.
- Fang, X., Xuan, Y., & Li, Q. (2013). Theoretical investigation of the extinction coefficient of magnetic fluid. *Journal of Nanoparticle Research*, 15(5), 1652.
- Frank, M. H., Jason, K. R., & Peter, D. F. (1998). A strain-isolated fibre Bragg grating sensor for temperature compensation of fibre Bragg grating strain sensors. *Measurement Science and Technology*, 9(8), 1163.
- Gao, P., Chen, X., & Feng, W. (2012). Simultaneous measurement of external refractive index and temperature based on long-period-grating-inscribed Sagnac interferometer and fiber Bragg grating. *Review of Scientific Instruments*, 83(10), 105001.
- Gao, R., Wang, H., Zhu, D., Fan, G., Yan, H., Wang, P., . . . Chen, Y. (2018). Acoustic frequency vibration sensor based on tapered SMS fiber structure. *Sensors and Actuators A: Physical*, 271, 243-250.
- Gong, Y., Zhao, T., Rao, Y., & Wu, Y. (2011). All-Fiber Curvature Sensor Based on Multimode Interference. *IEEE Photonics Technology Letters*, 23(11), 679-681.
- Gong, Z., Chen, K., Yang, Y., Zhou, X., Peng, W., & Yu, Q. (2017). High-sensitivity fiber-optic acoustic sensor for photoacoustic spectroscopy based traces gas detection. *Sensors and Actuators B: Chemical*, 247, 290-295.
- Goseberg, N., Wurpts, A., & Schlurmann, T. (2013). Laboratory-scale generation of tsunami and long waves. *Coastal Engineering*, 79, 57-74.

- Hatta, A. M., Semenova, Y., Wu, Q., & Farrell, G. (2010). Strain sensor based on a pair of single-mode-multimode-single-mode fiber structures in a ratiometric power measurement scheme. *Applied Optics*, 49(3), 536-541.
- Hill, K. O., Bilodeau, F., Malo, B., Kitagawa, T., Thériault, S., Johnson, D. C., . . . Takiguchi, K. (1994). Chirped in-fiber Bragg gratings for compensation of optical-fiber dispersion. *Optics Letters*, 19(17), 1314-1316.
- Huang, J., Lan, X., Wang, H., Yuan, L., Wei, T., Gao, Z., & Xiao, H. (2012). Polymer optical fiber for large strain measurement based on multimode interference. *Optics Letters*, 37(20), 4308-4310.
- Huang, Y., Wang, T., Deng, C., Zhang, X., Pang, F., Bai, X., . . . Chen, Z. (2017). A Highly Sensitive Intensity-Modulated Optical Fiber Magnetic Field Sensor Based on the Magnetic Fluid and Multimode Interference. *Journal of Sensors*, 2017, 9573061.
- Hughes, S. A. (1993). Laboratory Wave Generation *Physical Models and Laboratory Techniques in Coastal Engineering*, 7, 333-457.
- Kashyap, R. (2010). Chapter 7 - Chirped Fiber Bragg Gratings. In R. Kashyap (Ed.), *Fiber Bragg Gratings (Second Edition)* (pp. 301-345). Boston: Academic Press.
- Kersey, A. D., Davis, M. A., Patrick, H. J., LeBlanc, M., Koo, K. P., Askins, C. G., . . . Friebele, E. J. (1997). Fiber grating sensors. *Journal of Lightwave Technology*, 15(8), 1442-1463.
- Kumar, A., Goel, N. K., & Varshney, R. K. (2001). Studies on a few-mode fiber-optic strain sensor based on LP/sub 01/-LP/sub 02/ mode interference. *Journal of Lightwave Technology*, 19(3), 358-362.
- Kumar, A., Varshney, R. K., Antony C, S., & Sharma, P. (2003). Transmission characteristics of SMS fiber optic sensor structures. *Optics Communications*, 219(1), 215-219.
- Li, E. (2007). Temperature compensation of multimode-interference-based fiber devices. *Optics Letters*, 32(14), 2064-2066.
- Li, H.N., Li, D.S., & Song, G.B. (2004). Recent applications of fiber optic sensors to health monitoring in civil engineering. *Engineering Structures*, 26(11), 1647-1657.
- Li, L., Xia, L., Xie, Z., Hao, L., Shuai, B., & Liu, D. (2012). In-line fiber Mach-Zehnder interferometer for simultaneous measurement of refractive index and temperature based on thinned fiber. *Sensors and Actuators A: Physical*, 180, 19-24.
- Li, Y., Liu, Z., & Jian, S. (2014). Multimode interference refractive index sensor based on coreless fiber. *Photonic Sensors*, 4(1), 21-27.
- Lin, W., Miao, Y., Zhang, H., Liu, B., Liu, Y., & Song, B. (2013). Fiber-optic in-line magnetic field sensor based on the magnetic fluid and multimode interference effects. *Applied Physics Letters*. 103, 151101.

- Lin, Y. B., Pan, C. L., Kuo, Y. H., Chang, K. C., & Chern, J. C. (2005). Online monitoring of highway bridge construction using fiber Bragg grating sensors. *Smart Materials and Structures*, 14(5), 1075-1082.
- Liu, L., Lu, P., Wang, S., Fu, X., Sun, Y., Liu, D., . . . Yao, Q. (2016). UV Adhesive Diaphragm-Based FPI Sensor for Very-Low-Frequency Acoustic Sensing. *IEEE Photonics Journal*, 8(1), 1-9.
- Liu, Y., & Wei, L. (2007). Low-cost high-sensitivity strain and temperature sensing using graded-index multimode fibers. *Applied Optics*, 46(13), 2516-2519.
- Luo, L., Pu, S., Dong, S., & Tang, J. (2015). Fiber-optic magnetic field sensor using magnetic fluid as the cladding. *Sensors and Actuators A: Physical*, 236, 67-72.
- Ma, L., Kang, Z., Qi, Y., & Jian, S. (2015). Fiber-optic temperature sensor based on a thinner no-core fiber. *Optik*, 126(9), 1044-1046.
- Ma, Y., Qiao, X., Guo, T., Wang, R., Zhang, J., Weng, Y., . . . Feng, Z. (2012). Mach-Zehnder Interferometer Based on a Sandwich Fiber Structure for Refractive Index Measurement. *IEEE Sensors Journal*, 12(6), 2081-2085.
- Majumder, M., Gangopadhyay, T. K., Chakraborty, A. K., Dasgupta, K., & Bhattacharya, D. K. (2008). Fibre Bragg gratings in structural health monitoring—Present status and applications. *Sensors and Actuators A: Physical*, 147(1), 150-164.
- Malek-Mohammadi, S., & Testik, F. Y. (2010). New methodology for laboratory generation of solitary waves. *Journal of Waterway, Port, Coastal and Ocean Engineering*, 136(5), 286-294.
- Masnan, S. E. F., Zulkifli, A. Z., Azmi, N. M., Akib, S. M., Razak, H. A., Arof, H., & Harun, S. W. (2016). Steel Beam Compressive Strain Sensor Using Single-Mode-Multimode-Single-Mode Fiber Structure. *IEEE Photonics Journal*, 8(1), 1-6.
- May-Arrijoja, D. A., Ruiz-Perez, V. I., Bustos-Terrones, Y., & Basurto-Pensado, M. A. (2016). Fiber Optic Pressure Sensor Using a Conformal Polymer on Multimode Interference Device. *IEEE Sensors Journal*, 16(7), 1956-1961.
- Méhauté, B. L. (1976). *An Introduction to Hydrodynamics and Water Waves*: Springer Berlin Heidelberg.
- Mehta, A., Mohammed, W., & Johnson, E. G. (2003). Multimode interference-based fiber optic displacement sensor. *IEEE Photonics Technology Letters*, 15(8), 1129-1131.
- Meltz, G., Morey, W. W., & Glenn, W. H. (1989). Formation of Bragg gratings in optical fibers by a transverse holographic method. *Optics Letters*, 14(15), 823-825.
- Mishra, V., Lohar, M., & Amphawan, A. (2016). Improvement in temperature sensitivity of FBG by coating of different materials. *Optik - International Journal for Light and Electron Optics*, 127(2), 825-828.

- Mohammed, W. S., Smith, P. W. E., & Gu, X. (2006). All-fiber multimode interference bandpass filter. *Optics Letters*, 31(17), 2547-2549.
- Nguyen, L., Hwang, D., Moon, S., Moon, D. S., & Chung, Y. (2008). High temperature fiber sensor based on core diameter mismatch. *Optics express*. 16. 11369-75. 10.1364/OE.16.011369.
- Park, C.-S., Joo, K.-I., Kang, S.-W., & Kim, H.-R. (2011). A PDMS-Coated Optical Fiber Bragg Grating Sensor for Enhancing Temperature Sensitivity. *Journal of the Optical Society of Korea*, 15(4), 329-334.
- Pengfei, W., Gilberto, B., Yuliya, S., Qiang, W., & Gerald, F. (2011). A simple ultrasensitive displacement sensor based on a high bend loss single-mode fibre and a ratiometric measurement system. *Journal of Optics*, 13(7), 075402.
- Ran, Y., Xia, L., Han, Y., Li, W., Rohollahnejad, J., Wen, Y., & Liu, D. (2015). Vibration Fiber Sensors Based on SM-NC-SM Fiber Structure. *IEEE Photonics Journal*, 7(2), 1-7.
- Rao, J., Pu, S., Yao, T., & Su, D. (2017). Ultrasensitive Magnetic Field Sensing Based on Refractive-Index-Matched Coupling. *Sensors*, 17(7).
- Rionda Kuntaraco, A. M. H., Sekartedjo, Catur A. Prastyanto, Indrasurya B. Mochtar. (2014). Experimental Characterization of A Load Sensor Based on Singlemode – Multimode – Singlemode (SMS) Fiber Structure with A Variation of The Number of Bends. *IPTEK, Journal of Proceeding Series*, 1, 561-564.
- Rong, Q., Qiao, X., Wang, R., Sun, H., Hu, M., & Feng, Z. (2012). High-Sensitive Fiber-Optic Refractometer Based on a Core-Diameter-Mismatch Mach–Zehnder Interferometer. *IEEE Sensors Journal*, 12(7), 2501-2505.
- Rongxiang, Z., Tiegen, L., Qun, H., Yaofei, C., & Lin, L. (2014). U-bent single-mode–multimode–single-mode fiber optic magnetic field sensor based on magnetic fluid. *Applied Physics Express*, 7(7), 072501.
- Silva, S., Pachon, E. G. P., Franco, M. A. R., Hayashi, J. G., Malcata, F. X., Frazão, O., . . . Cordeiro, C. M. B. (2012). Ultrahigh-sensitivity temperature fiber sensor based on multimode interference. *Applied Optics*, 51(16), 3236-3242.
- Socorro, A. B., Del Villar, I., Corres, J. M., Arregui, F. J., & Matias, I. R. (2013). Mode transition in complex refractive index coated single-mode–multimode–single-mode structure. *Optics Express*, 21(10), 12668-12682.
- Sohn, H., Farrar, C. R., Hemez, F. M., Shunk, D. D., Stinemat, D. W., Nadler, B. R., & Czarnecki, J. J. (2004). A Review of Structural Health Monitoring Literature: 1996–2001; Los Alamos National Laboratory: Los Alamos, NM, USA, 2003
- Soldano, L. B., & Pennings, E. C. M. (1995). Optical multi-mode interference devices based on self-imaging: principles and applications. *Journal of Lightwave Technology*, 13(4), 615-627.

- Sorensen, R.M. (1997) Two-Dimensional Wave Equations and Wave Characteristics. In: Basic Coastal Engineering. Boston, MA: Springer US.
- Stephen, W. J., & Ralph, P. T. (2003). Optical fibre long-period grating sensors: characteristics and application. *Measurement Science and Technology*, 14(5), 49.
- Sun, A., Wu, Z., Wan, C., & Yang, C. (2012). All-fiber optic acoustic sensor based on multimode-single mode-multimode structure. *Optik*, 123(13), 1138-1139.
- Sun, R., Jin, D., Tan, F., Wei, S., Hong, C., Xu, J., . . . Wang, P. (2016). High-power all-fiber femtosecond chirped pulse amplification based on dispersive wave and chirped-volume Bragg grating. *Optics Express*, 24(20), 22806-22812.
- Sun, S., Lin, Z., Li, W., Zhu, N., & Li, M. (2018). Time-stretch probing of ultra-fast soliton dynamics related to Q-switched instabilities in mode-locked fiber laser. *Optics Express*, 26(16), 20888-20901.
- Sun, Y., Liu, D., Lu, P., Sun, Q., Yang, W., Wang, S., . . . Ni, W. (2017). High sensitivity optical fiber strain sensor using twisted multimode fiber based on SMS structure. *Optics Communications*, 405, 416-420.
- Suo, R., Chen, X., Zhou, K., Zhang, L., & Bennion, I. (2008). 800 nm WDM Interrogation System for Strain, Temperature, and Refractive Index Sensing Based on Tilted Fiber Bragg Grating. *IEEE Sensors Journal*, 8(7), 1273-1279.
- Tang, J., Pu, S., Dong, S., & Luo, L. (2014). Magnetic Field Sensing Based on Magnetic-Fluid-Clad Multimode-Singlemode-Multimode Fiber Structures. *Sensors (Basel, Switzerland)*, 14(10), 19086-19094.
- Tang, J., Zhou, J., Guan, J., Long, S., Yu, J., Guan, H., . . . Chen, Z. H. (2017). Fabrication of Side-Polished Single Mode-Multimode-Single Mode Fiber and Its Characteristics of Refractive Index Sensing. *IEEE Journal of Selected Topics in Quantum Electronics*, 23, 1-8.
- Tennyson, R. C., Mufti, A. A., Rizkalla, S., Tadros, G., & Benmokrane, B. (2001). Structural health monitoring of innovative bridges in Canada with fiber optic sensors. *Smart Materials and Structures*, 10(3), 560-573.
- Tian, K., Farrell, G., Wang, X., Lewis, E., & Wang, P. (2018). Highly sensitive displacement sensor based on composite interference established within a balloon-shaped bent multimode fiber structure. *Applied Optics*, 57(32), 9662-9668.
- Tian, K., Farrell, G., Wang, X., Yang, W., Xin, Y., Liang, H., . . . Wang, P. (2017). Strain sensor based on gourd-shaped single-mode-multimode-single-mode hybrid optical fibre structure. *Optics Express*, 25(16), 18885-18896.
- Tian, K., Zhang, M., Farrell, G., Wang, R., Lewis, E., & Wang, P. (2018). Highly sensitive strain sensor based on composite interference established within S-tapered multimode fiber structure. *Optics Express*, 26, 33982-33992

- Tjin, S. C., Wang, Y., Sun, X., Moyo, P., & Brownjohn, J. M. W. (2002). Application of quasi-distributed fibre Bragg grating sensors in reinforced concrete structures. *Measurement Science and Technology*, 13(4), 583-589.
- Tripathi, S. M., Kumar, A., Varshney, R. K., Kumar, Y. B. P., Marin, E., & Meunier, J.-P. (2009). Strain and Temperature Sensing Characteristics of Single-Mode–Multimode–Single-Mode Structures. *Journal of Lightwave Technology*, 27(13), 2348-2356.
- Tsuda, H. (2010). Fiber Bragg grating vibration-sensing system, insensitive to Bragg wavelength and employing fiber ring laser. *Optics Letters*, 35(14), 2349-2351.
- Villatoro, J., & Monzon-Hernandez, D. (2006). Low-cost optical fiber refractive-index sensor based on core diameter mismatch. *Journal of Lightwave Technology*, 24(3), 1409-1413.
- Wang, H., Pu, S., Wang, N., Dong, S., & Huang, J. (2013). Magnetic field sensing based on singlemode-multimode-singlemode fiber structures using magnetic fluids as cladding. *Optics letters*. 38. 3765-3768.
- Wang, L., Yang, L., Zhang, C., Miao, C., Zhao, J., & Xu, W. (2019). High sensitivity and low loss open-cavity Mach-Zehnder interferometer based on multimode interference coupling for refractive index measurement. *Optics & Laser Technology*, 109, 193-198.
- Wang, P., Brambilla, G., Ding, M., Semenova, Y., Wu, Q., & Farrell, G. (2011). Investigation of singlemode-multimode-singlemode and singlemode-tapered multimode-singlemode fibre structures and their application for refractive index sensing. *Journal of the Optical Society of America B*, 28(5), 1180-1186.
- Wang, Q., Du, C., Zhang, J., Lv, R., & Zhao, Y. (2016). Sensitivity-enhanced temperature sensor based on PDMS-coated long period fiber grating. *Optics Communications*, 377, 89-93.
- Wang, Q., & Farrell, G. (2006). All-fiber multimode-interference-based refractometer sensor: proposal and design. *Optics Letters*, 31(3), 317-319.
- Wang, Q., Farrell, G., & Yan, W. (2008). Investigation on Single-Mode–Multimode–Single-Mode Fiber Structure. *Journal of Lightwave Technology*, 26(5), 512-519.
- Wu, N.-J., Tsay, T.-K., & Chen, Y.-Y. (2014). Generation of stable solitary waves by a piston-type wave maker. *Wave Motion*, 51(2), 240-255.
- Wu, Q., Farrell, G., & Semenova, Y. (2010). Simple design technique for a triangular FBG filter based on a linearly chirped grating. *Optics Communications*. 2010, 283(6), 985–992.
- Wu, Q., Muhammad Hatta, A., Semenova, Y., & Farrell, G. (2009). Use of a single-multiple-single-mode fiber filter for interrogating fiber Bragg grating strain sensors with dynamic temperature compensation. *Applied Optics*, 48(29), 5451-5458.

- Wu, Q., Okabe, Y., & Wo, J. (2015). Fiber Sensor Based on Interferometer and Bragg Grating for Multiparameter Detection. *IEEE Photonics Technology Letters*, 27(12), 1345-1348.
- Wu, Q., Semenova, Y., Wang, P., & Farrell, G. (2011). High sensitivity SMS fiber structure based refractometer – analysis and experiment. *Optics Express*, 19(9), 7937-7944.
- Wu, Q., Semenova, Y., Wang, P., Hatta, A. M., & Farrell, G. (2011). Experimental demonstration of a simple displacement sensor based on a bent single-mode-multimode-single-mode fiber structure. *Measurement Science and Technology*, 22(2), 025203.
- Wu, Q., Yang, M., Yuan, J., Chan, H. P., Ma, Y., Semenova, Y., . . . Farrell, G. (2014). The use of a bend singlemode-multimode-singlemode (SMS) fibre structure for vibration sensing. *Optics & Laser Technology*, 63, 29-33.
- Xu, B., Li, Y., Sun, M., Zhang, Z.-W., Dong, X.-Y., Zhang, Z.-X., & Jin, S.-Z. (2012). Acoustic vibration sensor based on nonadiabatic tapered fibers. *Optics Letters*, 37(22), 4768-4770.
- Xu, Y., Lu, P., Qin, Z., Harris, J., Baset, F., Lu, P., . . . Bao, X. (2013). Vibration sensing using a tapered bend-insensitive fiber based Mach-Zehnder interferometer. *Optics Express*, 21(3), 3031-3042.
- Xu, Z., Sun, Q., Wo, J., Dai, Y., Li, X., & Liu, D. (2013). Volume Strain Sensor Based on Spectra Analysis of In-Fiber Modal Interferometer. *Sensors Journal, IEEE*, 13, 2139-2145.
- Yang, J., Guan, C., Tian, P., Chu, R., Ye, P., Wang, K., . . . Yuan, L. (2020). High sensitivity temperature sensor based on liquid filled hole-assisted dual-core fiber. *Sensors and Actuators A: Physical*, 303, 111696.
- Yang, W., Zhang, S., Geng, T., Li, L., Li, G., Gong, Y., . . . Yuan, L. (2019). High Sensitivity Refractometer Based on a Tapered-Single Mode-No Core-Single Mode Fiber Structure. *Sensors (Basel, Switzerland)*, 19(7), 1722.
- Yin, B., Li, Y., Liu, Z.-b., Feng, S., Bai, Y., Xu, Y., & Jian, S. (2016). Investigation on a compact in-line multimode-single-mode-multimode fiber structure. *Optics & Laser Technology*, 80, 16-21.
- Z., F., K., C., R., Q., & H., C. (2012). *Fundamentals of Optical Fiber Sensors*. Canada: John Wiley & Sons.
- Zhang, Y., Xue, L., Wang, T., Yang, L., Zhu, B., & Zhang, Q. (2014). High Performance Temperature Sensing of Single Mode-Multimode-Single Mode Fiber With Thermo-Optic Polymer as Cladding of Multimode Fiber Segment. *IEEE Sensors Journal*, 14(4), 1143-1147.
- Zhang, Y., Zhou, A., Qin, B., Deng, H., Liu, Z., Yang, J., & Yuan, L. (2014). Refractive Index Sensing Characteristics of Single-Mode Fiber-Based Modal Interferometers. *Journal of Lightwave Technology*, 32(9), 1734-1740.

- Zhang, Z., & Liu, C. (2017). Design of vibration sensor based on fiber Bragg grating. *Photonic Sensors*, 7(4), 345-349.
- Zhao, Y., Cai, L., & Hu, H. (2015). Fiber-Optic Refractive Index Sensor Based on Multi-Tapered SMS Fiber Structure. *IEEE Sensors Journal*, 15(11), 6348-6353.
- Zhao, Y., Li, X.-g., Meng, F.-c., & Zhao, Z. (2014). A vibration-sensing system based on SMS fiber structure. *Sensors and Actuators A: Physical*, 214, 163-167.
- Zhao, Y., & Liao, Y. (2004). Discrimination methods and demodulation techniques for fiber Bragg grating sensors. *Optics and Lasers in Engineering*, 41(1), 1-18.
- Zhao, Y., Xia, F., Chen, M., & Lv, R. (2018). Optical fiber low-frequency vibration sensor based on Butterfly-Shape Mach-Zehnder Interferometer. *Sensors and Actuators A: Physical*, 273, 107-112.

University of Malaysia